Design of Mixing Pulses for NMR Spectroscopy by Repeated Rotating Frames

Thesis advisor: Gerhard Wagner Paul William Coote

Design of mixing pulses for NMR spectroscopy by repeated rotating frames

Abstract

In protein NMR spectroscopy, homonuclear mixing pulses are used to reveal correlations amongst chemically bonded nuclear spins. These pulses must have low RF power levels and short durations to avoid probe damage and sample heating. However, standard mixing pulses require high RF power to cover the large bandwidths of chemical shift frequencies encountered in practice. This motivates the design of new mixing pulses which have high bandwidth-to-power ratios. Such pulses are especially useful for experiments at high Zeeman field, on the carbon channel, and/or with long mixing duration.

This thesis presents a new way to design homonuclear mixing pulses that are broadband, narrowband, or multi-band, to suit various existing and new experiments in protein NMR spectroscopy. These pulses are designed analytically, rather than by numerical optimization, by iterative construction of a series of nutating frames of reference. Pulse parameters are chosen frame-by-frame to effectively compress the chemical shift bandwidth arbitrarily many times, while largely maintaining couplings between spins. This means that the effective Hamiltonian is dominated by spin-spin couplings, rather than mismatched chemical shift frequencies, and therefore magnetization will move throughout the network of interacting nuclei.

This design methodology is explored analytically, via simulation, and in experiments. Pulses are created which have higher bandwidth than currently available broadband mixing pulses. Robustness to inhomogeneity in the pulse amplitude, which is important for the pulses to perform reliably in practice, is demonstrated. The loss of signal due to relaxation effects under the new pulses is no worse than under widely-used existing pulses. Novel multi-band pulses, which save power by neglecting unpopulated spectral regions, were created and

successfully implemented. Finally, a selection of *temporally orchestrated* mixing experiments, in which pulses with different mixing properties are applied in sequence to generate novel correlation patterns, are demonstrated. These patterns are potentially highly informative for protein spectroscopy, and cannot be observed using standard mixing pulses.

To my parents, Bill and Dorothy Coote

Acknowledgments

I am grateful to my research advisors, Professor Navin Khaneja and Professor Gerhard Wagner, for their wonderful support and mentorship. Professor Roger Brockett and Professor Yue Lu have been generous with their time, for which I am thankful.

Dr Haribabu Arthanari has devoted considerable time and effort to helping me develop my research, and I appreciate all his help and advice.

I also gratefully acknowledge the support and collaboration of my colleagues Dr Van Korolev, Dr Phil Owrutsky, Dr Jamin Sheriff, Dr Tsyr-Yan Yu, Kendra Leigh, Dr Scott Robson, and Dr Andras Boeszoermenyi.

Finally, I want to thank my family: Mum, Dad, Cathy, Michael, and Julia, and my sweetheart Rita, for heartfelt encouragement and support.

Contents

List of figures

List of tables

1

Introduction and background

This thesis is about the design of nuclear magnetic resonance (NMR) pulses for the transfer of magnetization amongst networks of coupled nuclear spins, suitable for protein spectroscopy. In particular, an analytical pulse design methodology is proposed which depends on familiar Hamiltonian transformations, such as rotating frame constructions, and on pulses comprising multiple sinusoidal modulations. With the aid of the Hamiltonian transformations, the effective (or average) Hamiltonian that describes the net effect of such a pulse can be calculated. The set of frequencies and amplitudes that parameterize the pulse can then be chosen to produce a desired effective Hamiltonian—specifically, one that transfers

magnetization between coupled spins that have a broad range of resonance frequencies. This methodology is of both theoretical and practical interest: The multi-frame approach stands in contrast to other NMR pulse design methods, which mostly rely on numerical searches or gradient descents. And in practice, the new pulses compare favorably with available alternatives for homonuclear mixing.

1.1 Overview

Broadband homonuclear mixing pulses are required for protein spectroscopy; however, they must be used at sufficiently low power and for sufficiently short times to avoid probe damage and sample heating (Hartmann and Hahn 1962; Müller and Ernst 1979; Braunschweiler and Ernst 1983; Ernst et al. 1987; Cavanagh et al. 2007; Hiller et al. 2009). However, standard homonuclear mixing pulses require high radiofrequency (RF) power to cover large bandwidths of chemical shift frequencies (Glaser and Quant 1996). This motivates the design of shaped mixing pulses which have high bandwidth-to-power ratios (Rucker and Shaka 1989; Kadkhodaie et al. 1991; Glaser and Quant 1996; Carlomagno et al. 1996; Zuiderweg et al. 1996; Bennett et al. 2003). Such pulses are especially useful for experiments at high Zeeman field, on the carbon channel, and/or with long mixing times.

The multi-rotating frame method developed in this thesis produces TOCSY (total correlation spectroscopy) mixing pulses which can cover a large bandwidth of resonance frequencies at low RF amplitude. These pulses are created analytically, i.e. without numerical searches or optimizations. Instead, pulse parameters are chosen systematically while the Hamiltonian is expressed in a series of different frames of reference. The effective (or *apparent*) chemical shift bandwidth changes in each new frame. In fact, the effective bandwidth can be driven to near zero by choice of pulse parameters. At the same time, the coupling tensor is largely maintained. That is, the pulse is used to construct an effective Hamiltonian which is dom-

inated by couplings, rather than mismatched chemical shift frequencies. This Hamiltonian satisfies the Hartmann-Hahn mixing condition (Hartmann and Hahn 1962), so that homonuclear cross-polarization takes place. At the end of the mixing pulse all spins are in phase, although they pass out of phase temporarily during the pulse.

The design method yields mixing pulses with larger bandwidth-to-RF amplitude ratios than FLOPSY (Kadkhodaie et al. 1991) and other widely-used sequences. Moreover, most common mixing sequences were designed using numerical optimizations (Glaser and Quant 1996). However, for this purely analytical method the computational load is negligible and new pulses tailored to a particular experimental application can be designed very quickly. Moreover, under the new method it is easy to exploit the bandstructure and coupling topology of the spin system to resolve particular patterns of correlation—a versatility that is proving to be useful in practice.

In this introductory chapter, NMR mixing pulses are motivated by a review their role in protein NMR spectroscopy. In particular, the process of protein resonance assignment, and how this depends crucially on the availability of homonuclear mixing pulses, is described. The physical origins of the relevant parts of the Hamiltonian are reviewed, and the Hartmann-Hahn mixing condition is explained. A survey of the available TOCSY pulses and pulse-design methods is presented. Special attention is paid to *nutating frame* spectroscopy, of which the multi-frame method can be considered a generalization.

1.2 Mixing pulses and NMR spectroscopy of proteins

1.2.1 Protein structure determination

Liquid-state NMR offers a powerful approach for finding the structure of proteins. Nuclear polarization tends to move amongst nearby spins as it relaxes to equilibrium, for example under the Nuclear Overhauser Effect (Anderson and Freeman 1962). Moreover, the rates

at which these cross relaxations occur in a sample are functions of internuclear distances (Cavanagh et al. 2007). At the same time, each spin-1/2 nucleus has, in general, a distinct, measurable, resonance frequency. This is determined broadly by its chemical species, and in detail by its local electrical environment. The spectroscopic method for protein structure determination divides into two parts: Firstly, the investigator must determine which resonances arise from which nuclei. This is called protein *assignment*. Secondly, the rates of cross relaxation between as many of these peaks as possible must be measured. This yields constraints on the spatial layout of the protein, which are hopefully sufficient to solve for a unique three-dimensional structure, or at least a best-fit structure. The protein samples used in NMR are typically enriched with spin-1/2 isotopes (notably carbon-13 and nitrogen-15) to increase the number of nuclei contributing to the measured signal (Cavanagh et al. 2007).

The assignment process uses knowledge of the historical distribution of resonance frequencies associated with spins in different amino acids, as well as measured interactions between bonded nuclei. These interactions can be used to transmit polarization throughout a network of spins during an NMR experiment, so that the collected measurement data will indicate which resonances arise from nuclei that are directly bonded, or separated by a few sequential bonds. The sharing of magnetization across couplings can be orchestrated in considerable detail, using various modes of selectivity. For example, the INEPT (insensitive nuclei enhanced by polarization transfer) sequence (Morris and Freeman 1979) transfers magnetization from hydrogen to either bonded carbons or nitrogens, and the timing of various delays in the sequence is selective for coupling topology; the transfer is tailored to CH_1, CH_2 and/or CH_3 depending on the choice of delay times (Levitt 2008).

The second major kind of selectivity of transfer is based on resonance frequency. Briefly, any applied mixing pulse will have one or more active bandwidths of resonance frequencies (Glaser and Quant 1996). Only spins within the working bandwidth(s) participate in the sharing of polarization. Often, it is desirable to make the bandwidth as broad as possible, so

that many chemical bonds can be observed. However, some patterns of correlation can only be observed by *restricting* the bandwidth, or deploying pulses that are selective for multiple frequency bands. This topic is explored in detail in subsequent chapters.

1.2.2 Chemical shift, J-coupling, and radiofrequency Hamiltonians

The Hamiltonian that describes the evolution of nuclear spin during an NMR experiment divides into three parts, called the chemical shift, J-coupling, and radiofrequency (RF) Hamiltonians. The Hamiltonian determines the dynamics of the nuclear spins, as described in Appendix A.

Chemical shift: The interaction between the atomic nuclei and the external field from the NMR spectrometer is weakened by local shielding of the nucleus by the surrounding bonding electrons. This means that two spins of the same nuclear species, in different locations in the same sample, will be subject to slightly different magnetic fields and therefore resonate at a distinct rates. The resonance frequency of each spin is a signature of its local environment, and the spectra of most relevant samples show multiple peaks.

Briefly, the physical mechanism of the chemical shift is that the external field generates a current in an electron cloud, which in turn induces a small local magnetic field with magnitude proportional to the applied field. This extra field superimposes upon the main field, and the local nuclear precession rate is determined by both components. In protein samples, the differences in the additional field (for different nuclei) are on the order of 10^{-6} of the magnitude of the external magnetic field—a small, but measurable, deviation in the frequency of the free induction decay signal (Hoch and Stern 1996). The shift in resonance frequency should be measured in dimensionless units (typically parts-per-million) because they are intrinsic properties of samples, whereas the resultant frequency in Hertz depends on the instrument.

The additional field is not, in general, parallel to the main field. However, the non-aligned components are generally ignored in liquid-state NMR by appeal to the following approximation: when expressed in rotating about the z-axis at the Larmor frequency of the nuclear species, the non-aligned additional magnetic fields will rapidly average out, while the component in the z-direction will remain. Therefore, to a good approximation, the precession of the spin is given by the Hamiltonian

$$H_{\mathrm{CS}} = -\gamma B_0(1+\delta)I_{\mathrm{z}}$$

where δ is the relative strength of the z-component of the additional, electron-induced field[1], and $-\gamma B_0$ is the Larmor frequency of the chemical species—gyromagnetic ratio multiplied by field strength (Griffiths 2005). In the frame that rotates about the z-axis at the Larmor frequency only the offset is important, so the chemical shift Hamiltonian is given by

$$H_{\mathrm{CS}} = \omega I_{\mathrm{z}}$$
$$\text{where} \quad \omega = -\gamma B_0 \delta$$

For the carbons in a protein in a 500 MHz NMR spectrometer, the range of chemical shift offsets can be up to about 25 kHz. Typically the precession of the rotating frame is not exactly at the Larmor frequency of the chemical species, but at the carrier frequency of the applied RF pulse (see below). If this differs from the Larmor frequency by δ_{RF}, then the precession of the spin in the rotating frame is at the rate $\omega = -\gamma B_0(\delta - \delta_{\mathrm{RF}})$. In other

[1]Note that there exist various conflicting conventions for the *sign* of δ, and more generally the sense of rotations in NMR across analyses, simulations, and in different spectrometers (Levitt 1997; Levitt and Johannessen 2000; Roehrl et al. 2005). In this thesis, the prescription of Levitt (1997) is followed closely: δ is positive, so that it is a really a *de*shielding constant, referenced against a *highly* shielded standard sample, tetramethylsilane (TMS). Then for nuclei with positive gyromagnetic ratio the precession in the rotating frame is clockwise (i.e. from the x to y to $-x$ to $-y$ axes) for δ higher than the carrier frequency, and anti-clockwise for δ lower than the carrier frequency. This means that on a spectrum displayed in the usual way, frequency is increasing from left to right, although the values of δ are decreasing.

words, if the rotating frame is precessing faster, then the spins' precession rates appear correspondingly slower, and visa versa.

J-COUPLING: In isotropic liquids, the J-coupling is the primary interaction between neighboring nuclear spins, allowing for magnetization to move from one nucleus to another. It arises indirectly, via the bonding electrons and their interaction with the field between the two nuclei. Observable J-couplings can occur in practice over multiple bonds, for example two hydrogens that are bonded to the same carbon (but not directly to each other) may still show a J-coupling interaction, even when the carbon channel is decoupled. The coupling depends on spatial orientation, although the anisotropic part is suppressed under the rapid molecular tumbling of the sample. The isotropic coupling Hamiltonian between two spins I and S takes the form

$$\begin{aligned} H_{\mathrm{J}} &= 2\pi J \mathbf{I}.\mathbf{S} \\ &= 2\pi J (I_{\mathrm{x}} S_{\mathrm{x}} + I_{\mathrm{y}} S_{\mathrm{y}} + I_{\mathrm{z}} S_{\mathrm{z}}) \end{aligned}$$

where the factor of 2π is included so that the magnitude of the interaction $|J|$ can be quoted in Hertz. Crucially, and unlike chemical shifts, the strength of the J-interaction is *independent* of the strength of the applied field. The implication is that as field strengths increase, the relative magnitude of the coupling as compared to the chemical shift *decreases*. Relatively large chemical shift differences prevent efficient transfer of magnetization across J-couplings (Hartmann and Hahn 1962; Glaser and Quant 1996). Therefore, observing J-couplings—and therefore chemical bonds in the sample—becomes more difficult at higher magnetic fields.

When the J-coupling is *heteronuclear*—between spins of different nuclear species—the

Hamiltonian takes a simpler longitudinal form:

$$H_{\mathrm{J}} = 2\pi J I_{\mathrm{z}} S_{\mathrm{z}}$$

This is because the transverse components rapidly average to zero in the doubly rotating frame corresponding to the two species' Larmor frequencies. This is essentially the same reasoning that was used to neglect the parts of the chemical shift field that were not aligned with the z-axis[2].

The applied RF Hamiltonian: The third relevant part of the Hamiltonian is the only part which can be freely chosen by the spectroscopist (subject to power allowances). One or more electromagnetic coils, aligned orthogonally to the main field, provide for the application of relatively small transverse fields with controllable amplitude and orientation. These fields are always chosen to oscillate at or near the Larmor frequency of a nuclear species of interest. Then, by the phenomenon of resonance, the small transverse fields do not average out in the rotating frame. These fields can be used to steer the nuclear magnetizations along desired trajectories.

The two components of the applied Hamilton are typically expressed in polar co-ordinates $(A(t),\ \phi(t))$ relative to a carrier frequency ω_{RF}. However, it is usually more convenient to express the RF Hamiltonian in a frame rotating at the carrier frequency about the z-axis.

$$\begin{aligned} H_{\mathrm{RF}} &= A(t)(\cos(\omega_{\mathrm{RF}} t + \phi(t))I_{\mathrm{x}} + \sin(\omega_{\mathrm{RF}} t + \phi(t))I_{\mathrm{y}}) \\ &\xrightarrow{rot.} A(t)(\cos(\phi(t))I_{\mathrm{x}} + \sin(\phi(t))I_{\mathrm{y}}) \end{aligned}$$

In this thesis, it will usually be preferable to use Cartesian co-ordinates $(u(t),\ v(t))$ to express

[2]These kinds of approximations are called *secular* approximations. For a thorough derivation, see the book by Levitt (2008).

the RF Hamiltonian in the rotating frame,

$$H_{\mathrm{RF}} = u(t)I_{\mathrm{x}} + v(t)I_{\mathrm{y}}$$

For an ensemble of isolated spins, each spin precesses about the instantaneous magnetic field, $\vec{B}(t) = [u(t),\ v(t),\ \omega]$, and can be steered from its equilibrium state aligned with the z-axis to a desired final state.

Throughout this thesis, the term 'power' is used in the signal processing sense, as the mean-square amplitude of a signal. Therefore, for an RF pulse, the power has units of kilohertz-squared. This usage is standard in NMR; however, it is not strictly the same as power in physics, which has energy units.

In practice, the precise application of RF fields is confounded by the presence of *RF inhomogeneity*. The field produced by the RF coils is not perfectly uniform across the sample volume. Therefore, spins in different locations see slightly different control fields. This is typically modeled by an inhomogeneity factor σ_{RF} sampled from a neighborhood of unity. The RF Hamiltonian then takes the form

$$H_{\mathrm{RF}} = \sigma_{\mathrm{RF}}u(t)I_{\mathrm{x}} + \sigma_{\mathrm{RF}}v(t)I_{\mathrm{y}}$$

Sophisticated pulse sequences robustly steer the magnetization to near a desired state irrespective of the value of σ_{RF}, for some reasonable range, for example $\sigma_{\mathrm{RF}} \in [0.9,\ 1.1]$ (Owrutsky and Khaneja 2012; Daems et al. 2013). It is common to numerically simulate pulses for a range of inhomogeneity factors to asses their robustness (Glaser and Quant 1996).

Total Hamiltonian: The full Hamiltonian for a realistic homonuclear sample, expressed in the rotating frame, comprises chemical shift, RF, and coupling terms. The chemical shift

terms produce a drift rotation of each spin about the z-axis, and each spin is steered by the same transverse RF terms. Isotropic couplings describe interactions amongst the nuclei.

$$H(t) = \sum_{\mathrm{k}} (\omega_{\mathrm{k}} I_{\mathrm{kz}} + \sigma_{\mathrm{RF}} u(t) I_{\mathrm{kx}} + \sigma_{\mathrm{RF}} v(t) I_{\mathrm{ky}}) + \sum_{\mathrm{k>j}} 2\pi J_{\mathrm{kj}} \mathbf{I}_{\mathrm{k}} . \mathbf{I}_{\mathrm{j}}$$

In the case of synchronized multi-channel (i.e. heteronuclear) pulses, there are two differences: a separate RF pulse shape may be applied to each nuclear species, and the couplings between spins of different species are longitudinal only. These effects are safely ignored in the presence of a suitable decoupling pulse (Cavanagh et al. 2007).

1.2.3 Hartmann-Hahn mixing condition

In the presence of only an isotropic J-coupling (that is, no chemical shift or RF terms), in-phase magnetization tends to move along bonds. For example, the evolution of two coupled spins under an isotropic coupling Hamiltonian, with initial state $\rho(0) = I_y$, is given by (Cavanagh et al. 2007):

$$\rho(t) = I_{\mathrm{y}} \cos^2(\pi J t) + S_{\mathrm{y}} \sin^2(\pi J t) + 2(I_{\mathrm{z}} S_{\mathrm{x}} - I_{\mathrm{x}} S_{\mathrm{z}}) \cos(\pi J t) \sin(\pi J t) \tag{1.1}$$

Therefore, if the mixing time is chosen as $T = \frac{1}{2J}$ then complete transfer is achieved at the conclusion of the mixing period; $\rho(T) = S_{\mathrm{y}}$. By swapping the I and S operators, the evolution of $\rho(0) = S_{\mathrm{y}}$ is seen to have a similar form. Moreover, the total in-phase magnetization $I_{\mathrm{y}} + S_{\mathrm{y}}$ is preserved at all times, while polarization difference $I_{\mathrm{y}} - S_{\mathrm{y}}$ is inverted after time T. In networks of greater than two spins, the movement of polarization along the bonds can be found by numerical integration of the Hamiltonian[3]. As in the two-spin case,

[3]Analytical expressions for the transfer of magnetization along J-couplings exist for some multi-spin networks, depending on coupling magnitudes and topology. Glaser (1993) catalogs many examples potentially relevant to protein NMR.

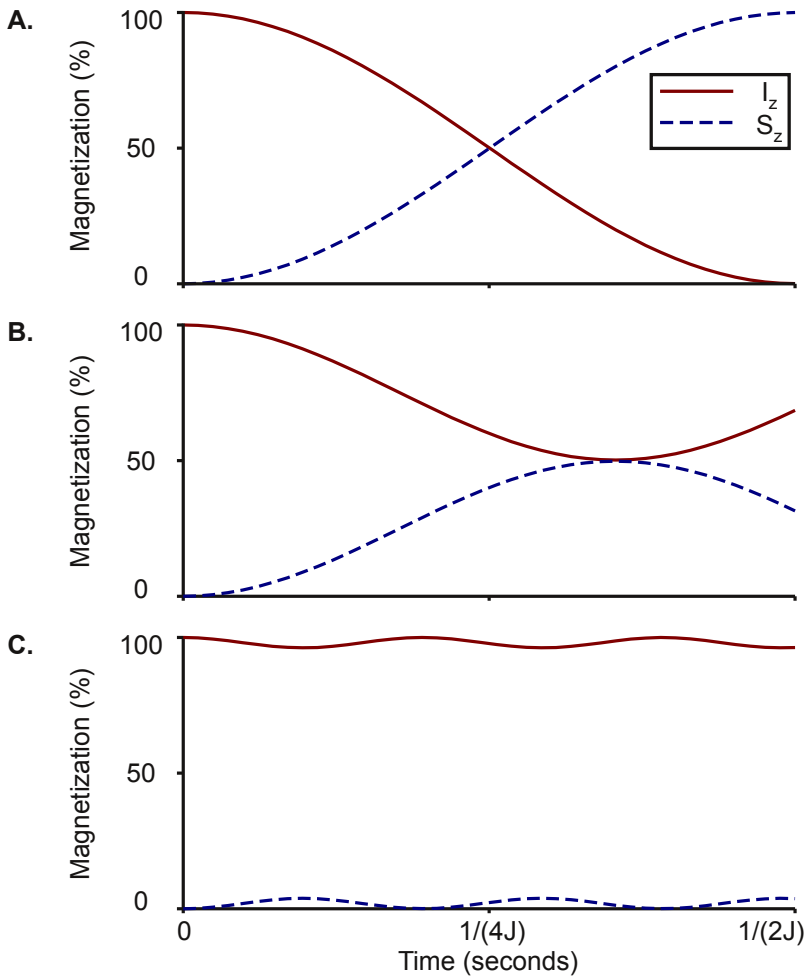

Figure 1.1: Simulated transfer of magnetization between two isotropically coupled spins. **A.** There are zero chemical shift offsets. The initial state is $\rho(0) = I_z$ and we measure $\mathrm{tr}(\rho(t)I_z)$ (solid line) and $\mathrm{tr}(\rho(t)S_z)$ (dashed line). The magnetization migrates between the nuclei in time $T = 1/(2J)$. **B.** The chemical shift difference is $\omega_I - \omega_S = 2\pi J_{IS}$. The transfer is truncated. **C.** The chemical shift difference is $\omega_I - \omega_S = 10\pi J_{IS}$. The transfer is eliminated. Intrinsic chemical shift differences in protein samples are much larger than the homonuclear couplings, so TOCSY pulses that effectively remove chemical shifts are required for resolving homonuclear couplings.

total magnetization is preserved (total magnetization $\sum_k I_{ky}$ commutes with the coupling Hamiltonian, making it a preserved quantity in quantum mechanics (Griffiths 2005)). This means that no signal component is *lost* by a TOCSY mixing period (except for relaxation losses); signal is merely *moved* amongst the spins.

In the presence of non-negligible chemical shift offsets, the transfer is truncated or completely removed. Figure 1.1 shows the trajectory of single-quantum operators I_z and S_z under an isotropic J-coupling, for three cases of chemical shift difference between the nuclei: matched, partially matched, and mismatched. Full transfer of magnetization is observed only in the matched case (equal chemical shifts). The trajectories were found by simulation of the two-coupled-spin Hamiltonian in Matlab (2011). Hartmann and Hahn (1962) derived the result that polarization transfer can only be efficient in networks with matched chemical shift offsets. This is usually stated as

$$|\omega_I - \omega_S| \ll 2\pi J_{IS}$$

Although samples contain *intrinsic* chemical shift differences, an applied RF Hamiltonian can be introduced which combines with the intrinsic Hamiltonian. The net evolution can be described by the *effective* or *average* Hamiltonian. In particular, a functioning TOCSY pulse removes effective chemical shift differences from the sample, while maintaining at least some of the coupling magnitude. Therefore, it makes sense to state the Hartmann-Hahn condition for the effective values in the presence of a particular pulse:

$$|\omega_I^{\text{eff}} - \omega_S^{\text{eff}}| \ll 2\pi J_{IS}^{\text{eff}}$$

The simplest example of a Hartmann-Hahn mixing pulse is a high-powered field aligned with the x-axis. If this pulse is much stronger than all the chemical shift offsets, then it continually and rapidly reverses the sense of the chemical shifts precession, refocusing the dispersion caused by differing chemical shifts. Therefore, the chemical shift terms average out over relevant time-scales. The effective Hartmann-Hahn condition is satisfied, and TOCSY transfer takes place (Levitt 2008). This requires high RF power for experimentally relevant bandwidths of chemical shift offsets, so in practice more sophisticated schemes are used

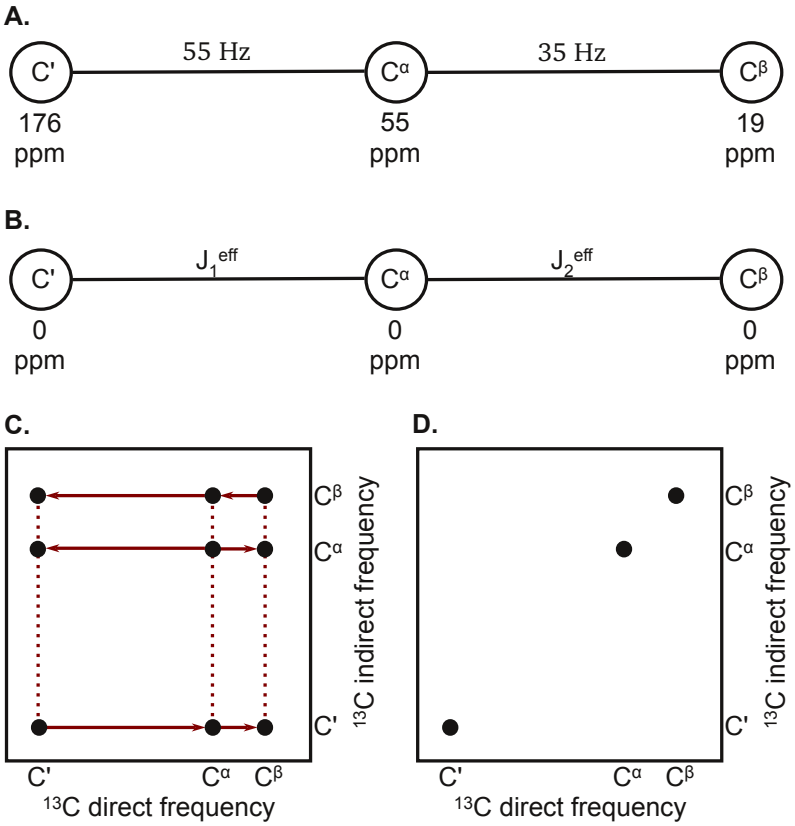

Figure 1.2: Schematic of the TOCSY of alanine. **A.** The intrinsic Hamiltonian of alanine (assuming non-carbon channels are decoupled). The chemical shift differences are on the order of tens of parts per million (i.e. kilohertz) and the couplings on the order of tens of Hertz. **B.** In the presence of a suitable RF pulse, the effective Hamiltonian contains no chemical shift differences, but maintains non-zero effective couplings. Typically these effective couplings are weaker than the intrinsic couplings, due to partial averaging under the RF pulse. This is the Hartman-Hahn matched regime. **C.** The TOCSY spectrum of alanine. Each resonance evolves during the indirect evolution, then the resulting polarization migrates to the coupled carbons during the TOCSY pulse. Finally, their precession is measured during signal acquisition. Off-diagonal peaks in the Fourier transformed data are evidence of chemical bonds, and are used to assign the resonance frequencies to particular nuclei. **D.** In the absence of Hartman-Hahn matching during the TOCSY pulse, transfer does not occur and the cross peaks are not observed, leaving no evidence that the three resonances are chemically bonded.

to produce matched effective chemical shifts. Figure 1.2 is a schematic of the intrinsic Hamiltonian of the coupled carbon-13 spins in alanine, along with the effective Hamiltonian

in the presence of a TOCSY pulse, and the TOCSY spectrum.

1.2.4 Multi-dimension spectroscopy and tocsy

Chemical bonds are observed indirectly using multi-dimensional spectroscopy and J-couplings. Spins are perturbed from equilibrium along the z-axis to the transverse plane, and allowed to precess at their characteristic resonance frequency for some amount of time (t_1), acquiring a time-dependent phase. A mixing pulse transfers the resultant state across any couplings, so that the phase acquired at the *original* resonance frequency is now associated with one or more spins with *different* frequencies. The spins then are allowed to evolve at their resonance frequency for another time period (t_2). Further transfers and delays can be added, so that the signal passes through a desired set of nuclei.

The final measured signal contains a component with acquired phase proportional to

$$\phi = \omega_1 t_1 + \omega_2 t_2 + \cdots + \omega_{\mathrm{n}} t_{\mathrm{n}}$$

where the $\{\omega_{\mathrm{k}}\}$ are the resonance frequencies of spins that participated in the series of J-mediated transfers. This is repeated many times, varying the length of each of the delays. The exception is the very last delay t_{n}, called the direct dimension, which can be observed during its precession. That is, the signal along the t_{n} axis can be recorded in a single NMR scan, while all other dimensions must be sampled at a rate of one point per dimension, per scan[4].

A final n-dimensional data matrix contains oscillations at different frequencies along different time dimensions ($t_1,\ t_2, \ldots,\ t_{\mathrm{n}}$). The spins are always relaxing during the various delays and transfers, so that each sinusoidal component is enveloped by a decaying exponen-

[4]Is is not necessarily required to finely sample all these dimensions. Sophisticated sampling schedules and reconstruction algorithms can greatly improve the amount of relevant information that can be extracted from a sparse sampling of first n-1 dimensions (Hyberts et al. 2012; 2013)

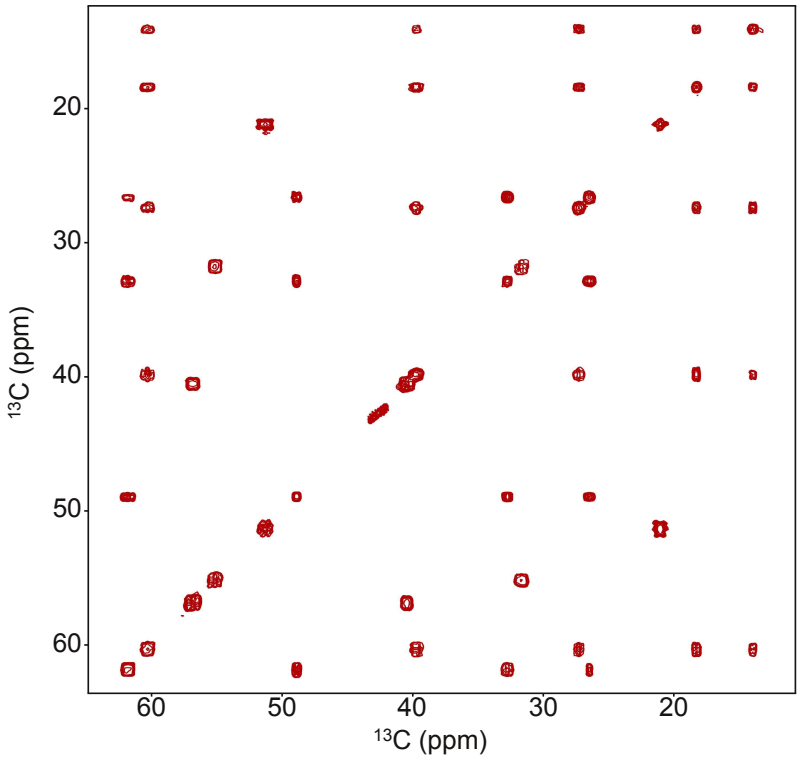

Figure 1.3: Example of a TOCSY spectrum of a pentapeptide sample. The off-diagonal peaks reveal which resonance frequencies belong to the same spin network. There are 15 resonances in total, which come from five separate networks of coupled carbon-13. The co-ordinates of each cross peak reveal that two nuclei are chemically bonded, either directly or via intermediate spins. The bandwidth is about 170 times greater than the couplings, so a mixing pulse was required in order to satisfy the Hartmann-Hahn condition (c.f. Figure 1.1). The sample and TOCSY pulse used are described in detail in Chapter 4.

tial in the time-domain, which corresponds a Lorentzian line shape in the frequency-domain. The data are Fourier transformed, yielding a Lorentzian peak with frequency co-ordinates $(\omega_1,\ \omega_2, \ldots,\ \omega_n)$. This peak is evidence that these resonances arise from spins that are directly chemically bonded, or else separated by a small number of sequential bonds. This information is used to assign each resonance frequency to a particular nucleus in the sample. Figure 1.3 shows the experimental two-dimensional TOCSY spectrum of a simple pentapeptide sample, obtained using a low-powered, multi-frame mixing pulse.

Clearly, the RF pulses that bring about transfer of magnetization are indispensable for

assigning proteins. However, these pulses are subject to constraints on their power and duration that are in tension with their desired properties, such as high bandwidth and strong effective coupling strengths. Therefore, the mixing pulses should be optimized to reduce average RF amplitude while enhancing bandwidth and effective coupling strength. The development of these RF pulses is the central task of this thesis.

1.3 Review of available pulses

Protein NMR experiments are planned, analyzed, and programmed into spectrometers using the assumption that certain idealized pulses are available. An ideal excitation will move magnetization reliably from the z to x axes, irrespective of chemical shift offset. A perfect decoupling pulse will remove all artifacts of heteronuclear couplings. An ideal mixing pulse will allow the J-couplings to evolve as if there were no chemical shift offsets.

However, each of these idealized actions is underwritten by a more detailed pulse design and analysis. For example, a spectroscopist will choose to include decoupling for a certain duration as part of the overall experiment, and this will deploy a complicated shaped pulse which has been designed or optimized elsewhere. This section contains a brief historical review of NMR pulses and the methods used to create them.

1.3.1 Broadband excitation pulses

Broadband excitation pulses are included in this review for two reasons: Firstly, they perform a rotation of all spins about the same axis and therefore eliminate the chemical shift dispersion, as required by the Hartmann-Hahn condition. Many mixing pulses are created using sequences of broadband excitation (90° rotation) or inversion (180° rotation) pulses with varying phases. In particular, WALTZ-type sequences use this approach (Shaka et al. 1983; Bax 1988). Moreover, the phase-alternating *super-cycles* into which nearly all mixing

pulses are embedded rely on each individual instance of the pulse being an approximate spin inversion (Glaser and Quant 1996). The second reason for reviewing excitation pulses is that they have received the most attention from an explicitly control-theoretic perspective (Khaneja 2009; Li and Khaneja 2009).

Simple hard pulses provide excitation of sufficiently large bandwidth for many applications (Cavanagh et al. 2007). The excitation bandwidth is about 2.5 times the applied RF amplitude (Skinner et al. 2003). However, beginning around three decades ago (Freeman et al. 1980), more complicated pulses have been used to reduce off-resonance effects and increase bandwidth for high-field applications.

At first, the approach was to use principles such as symmetry or informed guesswork to find pulses which naturally *refocus* dispersions. For example, Freeman et al. (1980) suggested six sequences each consisting of two or three hard pulses with different flip angles and phases, which were found in simulation to exhibit robustness to various inhomogeneities, in the sense that dispersions of magnetization trajectory during the pulse would tend to refocus by the end of the pulse.

Soon, pulse design was being carried out by numerical searches. The basic procedure was to parameterize a family of pulses using a relatively small number of free variables, which were then varied exhaustively in simulations in order to choose the optimal settings. Specific examples include: sequences of hard pulses with arbitrary durations and alternating phases (Levitt 1986; Shaka and Pines 1987); adiabatic pulses (Silver et al. 1984; Bohlen et al. 1989; Ermakov and Bodenhausen 1993); *sinc*-pulses for selective excitation (Runge et al. 1988); and Gaussian amplitude modulation (Emsley and Bodenhausen 1990).

An early move towards iterative improvement—as opposed to exhaustive searches—was the *polychromatic* pulses proposed by Kupce and Freeman (1994), which attempt to create on-resonance conditions simultaneously across a broad spectral range. The idea is to apply a superposition of several weak rectangular pulses of relatively long duration (about 2 ms),

each with a slightly different carrier frequency. In other words, the pulse has a simple Fourier series representation consisting of a few non-zero terms with similar magnitude and equal phase. The pulse is repeatedly simulated in order to observe its excitation profile. The magnitude and phase of each frequency component is systemically increased or reduced until a reasonably uniform and broad excitation profile is achieved. In experimental tests, the excitation profile was similar to a simple hard pulse (however the time taken to excite the spins was longer).

Recently, pulses have been optimized over a much larger space of free parameters using optimal control theory, specifically gradient descent towards a pulse that meets the necessary conditions for optimality given by the Pontryagin maximum principle (Pontryagin 1959). Such pulses obtain near-perfect performance over a specified bandwidth. This method was first applied to selective inversion and excitation in MRI (Conolly et al. 1986; Mao et al. 1986; Rosenfeld and Zur 1996). Later, a refined version was applied to broadband excitation for protein spectroscopy (Skinner et al. 2003; 2004; 2006). With enough computational time, the dynamical model used in the descent can include a sampling of chemical shift offsets, RF inhomogeneity factors, relaxation terms, couplings, or other experimentally relevant parameters.

Pulse design by Fourier synthesis directly exploits the Lie algebraic nature of spin dynamics (Li and Khaneja 2006; Pryor and Khaneja 2006; Li and Khaneja 2009; Khaneja 2009). For a set of small rotations, each with flip angle α, executed sequentially about the $x,\ y,\ -x$, and $-y$ axes, the net effect is a rotation with flip angle $\sim \alpha^2$ about the z-axis. This is because the overall effect of the four rotations is, for small α, given by $[\alpha I_{\mathrm{x}},\ \alpha I_{\mathrm{y}}] \propto \alpha^2 I_{\mathrm{z}}$. Further propagators can be constructed by further cyclical maneuvers, such as $[\alpha I_{\mathrm{x}},\ \alpha^2 I_{\mathrm{z}}] \propto \alpha^3 I_{\mathrm{y}}$. In this way, effective Hamiltonians comprising a set of polynomials in α can be accessed, and therefore a desired effective Hamiltonian can be approximately synthesized. Applications include ensuring that the pulse is robust to unwanted variations in field-strength, or to

differing chemical shift offsets. The time required to generate higher-order polynomial terms can be unfeasibly long in practice, so pulses designed by this method are mostly of theoretical interest, particularly as elegant proofs of ensemble controllability (Li and Khaneja 2009).

1.3.2 Broadband and multi-band mixing

The first composite pulse to achieve broadband mixing by effectively satisfying the Hartmann-Hahn condition was given by Bax and Davis (1985). The pulse worked by repeated application of the $90_x - 180_y - 90_x$ compensated inversion element, which has a slightly broader inversion profile than a rectangular 180 degree pulse. The inversions were arranged into an MLEV-17 supercycle so that the phase of the inversion element was varied systematically, which tends to average out some of the error around the edges of the bandwidth. The inversions reverse the sense of the precession under the chemical shift Hamiltonian, refocusing the spins and effectively eliminating the chemical shift terms from the effective Hamiltonian. The mixing bandwidth of this approach is about 80% of the RF amplitude (Glaser and Quant 1996).

The most widely used mixing pulses in liquid state NMR are DIPSI (decoupling in the presence of scalar interactions) and FLOPSY (flip-flop spectroscopy) (Glaser and Quant 1996; Cavanagh et al. 2007). The design principle underlying the DIPSI scheme is to apply an arbitrary sequence of hard pulses with arbitrary duration along a single axis, i.e. alternating in the plus or minus x-direction (Shaka et al. 1988; Rucker and Shaka 1989). The effective Hamiltonian from this pulse sequence can be calculated to high accuracy via the first few terms of the Magnus expansion (Magnus 1954), and expressed in terms of the 15 basis elements of the two-spin system. Then conditions on the hard pulses can be derived for unwanted terms (such as chemical shifts) to be minimized, and desired terms (such as the isotropic part of the effective coupling tensor) to be maximized. Consideration of these conditions led to a reduced parameter space, which was explored numerically. The FLOPSY

sequence was derived in a similar way to DIPSI, but the hard-pulses were applied with arbitrary phase (Kadkhodaie et al. 1991). The flip angles and phases were numerically optimized, and marginally better performance than DIPSI was achieved.

The mixing bandwidths of DIPSI and FLOPSY are limited to approximately twice the RF amplitude (Cavanagh et al. 2007; Glaser and Quant 1996). That is, the pulse fails when the chemical shift ω of one or both of the coupled spins is larger than the allowed control amplitude $|A(t)|_{\max}$. However, in protein spectroscopy the range of chemical shifts encountered in practice is large. Therefore, these standard mixing pulses cannot be used in all desired experiments, within the RF power limitations of current hardware (Kovacs and Gossert 2014).

Band-selective heteronuclear and homonuclear mixing pulses were explored in the mid-1990s, notably in two companion papers (Carlomagno et al. 1996; Zuiderweg et al. 1996) (the nutating frame approach, developed around the same time, is discussed separately in the next subsection). The goal was not explicitly to lower input power, but rather to restrict the size of the spin network using the selectivity of the band structure (Carlomagno et al. 1996). The strategy is to repeatedly apply a shaped, low-power inversion pulse along a single axis with an additional modulation. This creates a two-band structure, with the separation controlled by the frequency of the modulation. An effective planar J-coupling with reduced strength is retained in the doubly-rotating frame. Interference between the two bands proved problematic unless the band separation was at least three times the root-mean-square RF amplitude (Zuiderweg et al. 1996). In the case of the carbon spectrum, mixing between two bands of 30 ppm width (to correlate carbon-alpha with carbonyl) was demonstrated in simulation and experiment.

For the heteronuclear mixing problem, where different controls can be applied to each nuclear species, the two bandwidths can be controlled independently. This leads to a variety of questions about transfer efficiency between different spin pairs sampled from the two

bands, which have been explored using computer simulations (Carlomagno et al. 1997).

1.3.3 Nutating frame spectroscopy

Construction of a *nutating* frame, in which the spins precess about a tilted axis defined by their chemical shift offset plus the RF field, allows the effective chemical shifts to be manipulated, for example for slice-selection in NMR imaging (Hoult 1980; Hedges and Hoult 1988) and dual-band TOCSY (Grzesiek and Bax 1995). It is worth reviewing this approach, as the multi-frame method can be considered a generalization of nutating frame spectroscopy.

The idea of nutating frame spectroscopy is to apply a pulse that is constant along one axis and cosine-modulated along the other, so that the Hamiltonian of an isolated spin, expressed in a frame rotating at the carrier frequency of the RF pulse, is

$$H(t) = \omega I_{\mathrm{z}} + u I_{\mathrm{x}} + 2a\cos(ft) I_{\mathrm{y}}$$

The cosine term can be decomposed into two circularly-polarized waves precessing at rates $\pm f$ about an axis orthogonal to the y-axis. Also, the time-invariant terms define a field of magnitude $\sqrt{\omega^2 + u^2}$, also orthogonal to the y-axis. By redefining the x and z axes, the Hamiltonian can be expressed as

$$H'(t) = \sqrt{\omega^2 + u^2} I_{\mathrm{z}'} + \underbrace{a\cos(ft) I_{\mathrm{y}} + a\sin(ft) I_{\mathrm{x}'}}_{\text{counter-rotating wave}} + \underbrace{a\cos(-ft) I_{\mathrm{y}} + a\sin(-ft) I_{\mathrm{x}'}}_{\text{on-resonance wave}}$$

Observe that this can only be achieved if the z' and x' axes are defined *differently* for different ω. In a frame rotating about the z'-axis at rate f, the Hamiltonian can be found using (A.2),

$$H''(t) = (\sqrt{\omega^2 + u^2} - f) I_{\mathrm{z}''} + a I_{\mathrm{y}''}$$

where the counter-rotating wave was ignored in accordance with the rotating wave approximation (Ernst et al. 1987). Crucially, the z-component can be chosen to be zero for two *different* values of ω that are equal in magnitude but have opposite sign. This is achievable even for relatively low RF amplitude, since the reduction in magnitude of the z-component is largely shouldered by the offset $-f$, which arises from the cosine modulation in the pulse. Periodically, the rotating y''-axis aligns with the original y-axis, so careful choice of pulse time can ensure that an initial state $\rho(0) = I_{\mathrm{y}} = I_{\mathrm{y}''}$ evolves trivially under the effective Hamiltonian $H''(t) = aI_{\mathrm{y}''}$ to $\rho(T) = I_{\mathrm{y}''} = I_{\mathrm{y}}$, preserving the phase of spins. In other words, the net effect of the Hamiltonian up to time T is a rotation about the y-axis on the Bloch sphere, and this rotation *fixes* its own axis, preserving the y-component of magnetization.

Grzesiek and Bax (1995) also calculated an expression for the effective J-coupling magnitude when this pulse is applied to a two-spin system, and showed that the Hartmann-Hahn condition could be satisfied for two widely separated chemical shifts, in which case the effective coupling is half as strong as the intrinsic coupling.

This thesis generalizes the nutating frame approach in two ways. Firstly, not only can a nutating frame induce a dual band structure, as in Grzesiek and Bax (1995), but it can also reduce the effective bandwidth over a *single* broad spectral region. Secondly, this scheme can be harnessed *iteratively* via successive rotating frame constructions generated by appropriate sine and cosine modulation of the RF field. The effective bandwidth is modified by each new rotating frame, and can be driven to near zero. Meanwhile, the couplings can be largely maintained. This allows for the of design broadband, narrowband, and multi-band pulses for polarization transfer.

1.4 Outline of this thesis

Chapter 2 addresses the problem of eliminating effective chemical shift terms from the Hamiltonian, so that all spins in the sample stay aligned with (or periodically return to) the same axis. In NMR, this is called broadband *spin-locking*. It is demonstrated that broadband spin-locking can be achieved by the multi-frame pulse design method. Practical issues such as robustness to experimental imperfections are addressed, along with the relative scalings of bandwidth, RF power, and pulse time. Moreover, it is demonstrated that in the multi-frame setting it is straightforward to create pulses that spin-lock over two (or more) distinct spectral regions.

The multi-frame method uses a rotating wave-approximation in each new frame. However, in contrast to its usual application, the approximation is being used to suppress relatively slowly oscillating terms. Therefore, there is a question as to whether the approximation is valid. Nonetheless, we observe high-quality spin-locking in simulation and experiment. Chapter 3 treats this approximation in detail. The fundamental intuition is that rapidly oscillating, off-resonance terms can be traded for small static corrections in the manner of perturbation theory, such as the Bloch Siegert shift (Bloch and Siegert 1940). Serendipitously, the corrections appropriate to the multi-frame method appear largely as *additional* effective chemical shift offsets. The iterative method is designed to *reduce and eliminate* chemical shifts. Therefore, the additional corrections do not threaten the basic architecture of the method.

Chapter 4 considers multi-spin systems containing J-couplings. The coupling tensor is transformed into the multi-rotating frame, so that pulses can be designed to *maintain* the couplings, even as the chemical shifts are eliminated. In this way the Hartman-Hahn condition can be satisfied. The performance of these broadband mixing pulses are compared to existing pulse sequences, and the effects of relaxation are addressed. Next, the multi-frame

method is adapted to respect two widely used performance metrics, with the encouraging result that multi-frame pulses outperform their peers according to both metrics.

In practice, *broadband* is not the only regime of interest. Chapter 5 treats the design of pulses that are dual-band, multi-band, or narrowband, to suit various experimental situations. These kinds of pulses serve two purposes: to save power by targeting only the relevant parts of the spectrum, and to generate a favorable spin-network topology by selectively excluding certain spins. The utility of *temporally orchestrated* mixing—where different couplings are resolved sequentially—is explored. This is used to address three current topics in protein NMR: assignment of aromatic nuclei, polarization transfer across weak couplings between neighboring carbon alphas, and assignment of methyls in large proteins.

Chapter 6 summarizes the results and remaining issues, and suggests future directions.

2

Broadband spin-locking by repeated rotating frames

The Hartmann-Hahn mixing condition states that a necessary condition for mixing is a small effective chemical shift difference (Hartmann and Hahn 1962). In a sample with many spins, such as a protein, this means that the effective chemical shift bandwidth must be small relative to the magnitude of couplings (Glaser and Quant 1996). Here, the term *effective* refers to the overall result of the pulse: some chemical shift dispersion *during* the pulse is acceptable, provided that the trajectories for different chemical shifts periodically

return exactly to their starting points. This is called effective *spin-locking*—the spins are behaving on average as though they have zero chemical shift bandwidth.

In this chapter, an ensemble of isolated spin-1/2 nuclei with a large chemical shift bandwidth is considered, and a parametric form is suggested for the RF pulse. Pulse parameters are chosen recursively to ensure that there exists a multi-tilted, multi-rotating frame of reference in which the effective bandwidth is arbitrarily small. Furthermore, this highly contrived frame aligns with the original frame at stroboscopic times, so that spin-locking generated in the multi-rotating frame is also valid in the original frame at these times.

Robustness to RF inhomogeneity is demonstrated, and scaling of power, bandwidth, and duration with the number of frames is explored. Extensions to dual-band and multi-band pulses are also described.

2.1 Iterated rotating frames

This section begins with a description of the overall architecture of the multi-frame method, and then addresses details such as precisely how to generate the frequencies and amplitudes that parameterize the RF pulse.

2.1.1 Overview of the method

For an isolated spin-1/2, the chemical shift and RF Hamiltonians are

$$H_{\mathrm{CS}} + H_{\mathrm{RF}} = \omega I_{\mathrm{z}} + u(t) I_{\mathrm{x}} + v(t) I_{\mathrm{y}}$$

The chemical shift ω is sampled from a large bandwidth or multi-band structure. For an iterated bandwidth-reduction method, the idea is to choose RF terms $u(t)$ and $v(t)$ and then express the Hamiltonian in a new frame of reference. Considered in the new frame

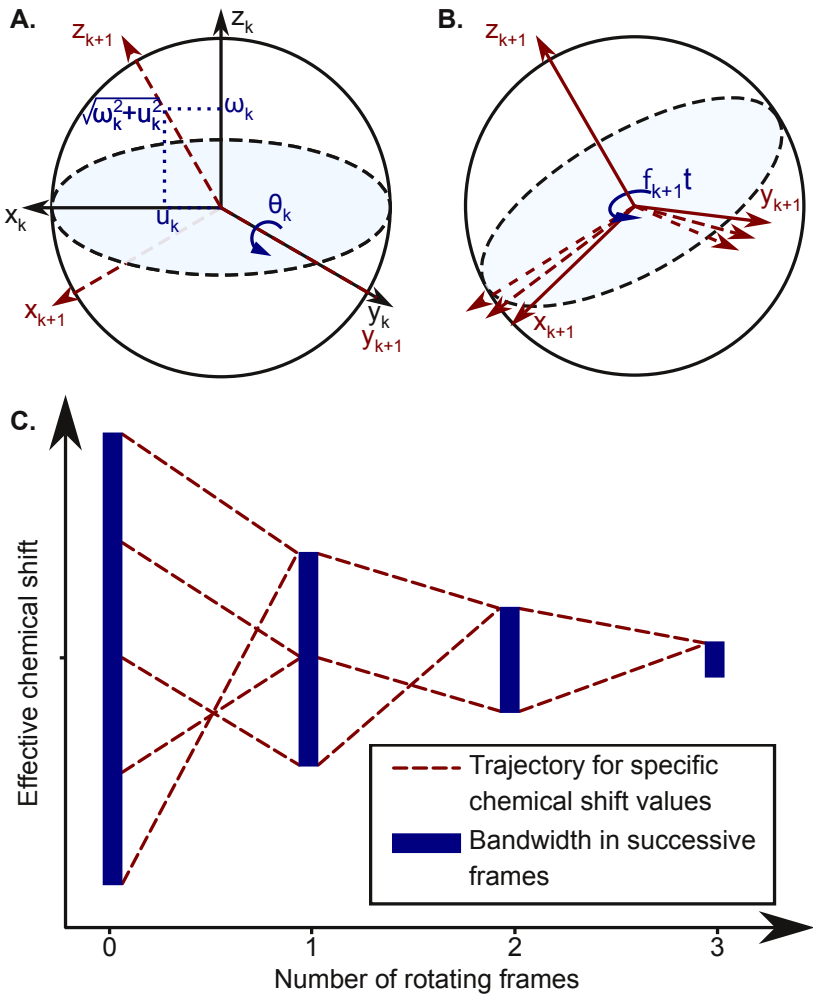

Figure 2.1: Overview of the multi-frame method. **A.** In each tilted, rotating frame the I_z and I_x components of the Hamiltonian are time-invariant. The Bloch sphere axes are tilted about the y-axis such that the new z-axis is aligned with the static part of the field, i.e. the vector sum of $\omega_k\hat{z}$ and $u_k\hat{x}$. **B.** A frame that rotates about the new z-axis displaces the effective chemical shift by $-f_{k+1}$ and demodulates the y-component of the pulse. **C.** The effective chemical shift in the new frame is given by (2.2). This equation can be applied iteratively to effectively compress a large bandwidth. In this schematic, chemical shift values are updated using (2.2) three times. Although (2.2) applies to individual effective chemical shifts (dashed lines), pulse parameters can be chosen so that the set of effective chemical shifts present in the sample becomes smaller with each new frame.

the Hamiltonian's form is unchanged; however, the effective chemical shift bandwidth is reduced. This process can be repeated arbitrarily many times to drive the effective chemical

shift bandwidth to near zero. After the k^{th} change of frames, the Hamiltonian is

$$H^{(\mathrm{k})} = \omega_{\mathrm{k}} I_{\mathrm{z}} + u_{\mathrm{k}}(t) I_{\mathrm{x}} + v_{\mathrm{k}}(t) I_{\mathrm{y}} \tag{2.1}$$

where the superscript (k) indicates the frame in which the Hamiltonian is expressed. Unspecified functions $u_{\mathrm{k}}(t)$ and $v_{\mathrm{k}}(t)$ are retained. These serve as the effective RF pulse applied in the k^{th} frame. The effective chemical shifts in successive frames ω_{k} obey the recursion (derived below)

$$\omega_{\mathrm{k}} = \sqrt{\omega_{\mathrm{k-1}}^2 + u_{\mathrm{k-1}}^2} - f_{\mathrm{k}} \tag{2.2}$$

so that the bandwidth of ω_{n} for $n > 0$ can be engineered from the original bandwidth of ω by choice of free parameters $\{f_1,\ f_2, \ldots,\ f_{\mathrm{n}}\}$ and $\{u_0, u_1, \ldots, u_{\mathrm{n-1}}\}$. These free parameters are frequencies and amplitudes of simultaneously-applied oscillating RF fields, detailed below. The chemical shift $\omega_{\mathrm{k-1}}$ takes on a range of values for different spins in the sample, and (2.2) encodes the range of values for ω_{k} (the effective chemical shift in a new frame of reference). Observe that values of $\omega_{\mathrm{k-1}}$ with equal magnitude but opposite sign will produce identical ω_{k}. This means that the original bandwidth can in a sense be *folded up* and made small.

Recursions are given below that fix the pulse parameters frame-by-frame so that $|\omega_{\mathrm{n}}| \ll |v_{\mathrm{n}}|$ regardless of the original chemical shift. Therefore, in frame n (i.e. the final constructed frame), the Hamiltonian is

$$H^{(\mathrm{n})} \approx v_{\mathrm{n}} I_{\mathrm{y}}$$

Applying the von Neumann dynamics (A.1) to an initial state $\rho^{(\mathrm{n})}(0) = I_{\mathrm{z}}$ (the superscript

indicates that that the density matrix is expressed in frame n),

$$\begin{aligned}\rho^{(\mathrm{n})}(T) &= \exp(-iv_{\mathrm{n}}I_{\mathrm{y}}T)I_{\mathrm{z}}\exp(iv_{\mathrm{n}}I_{\mathrm{y}}T)\\ &= \cos(v_{\mathrm{n}}T)I_{\mathrm{z}} - \sin(v_{\mathrm{n}}T)I_{\mathrm{x}}\end{aligned}$$

Clearly, in this frame it is straightforward to execute a uniform pulse with flip angle $\alpha = v_{\mathrm{n}}T$ about the y-axis. For example, choosing $v_{\mathrm{n}}T = \pi/2$ excites spins from their equilibrium state I_{z} to the state $-I_{\mathrm{x}}$.

Finally, all the frames that have been constructed must have aligned y-axes at the final time T. This ensures that whatever rotation about the y-axis has been achieved in the final frame (k=n) is also valid in the original frame (k=0), and also in all the intermediate frames (k = 1, 2, . . . , n–1).

2.1.2 Functional form of the RF pulse

To generate (2.1) and (2.2), RF fields are chosen to be constant along the x-axis $u_{\mathrm{k}}(t) = u_{\mathrm{k}}(0)$ and sinusoidally modulated along the y-axis $v_{\mathrm{k}}(t) = 2v_{\mathrm{k+1}}(t)\cos(f_{\mathrm{k+1}}t) + 2u_{\mathrm{k+1}}(t)\sin(f_{\mathrm{k+1}}t)$. The idea is to resolve this modulation in a rotating frame such that $(u_{\mathrm{k+1}}(t), v_{\mathrm{k+1}}(t))$ is an arbitrary effective RF pulse applied in the subsequent frame. Since the Hamiltonian is time-invariant in the x-z plane, the reference frame is tilted such that the static part of the field is aligned with the new z-axis (as in Figure 2.1A). The required tilt angle is $\theta_{\mathrm{k}} = \mathrm{atan2}(u_{\mathrm{k}}, \omega_{\mathrm{k}})$ about the y-axis, where atan2 is the two-argument arctangent function. The tilt is captured by the rotation operator $\exp(i\theta_{\mathrm{k}}I_{\mathrm{y}})$ applied to the system (i.e. applied to the density matrix and the Hamiltonian as explained in Appendix A.4). Since θ_{k} depends on ω_{k}, for each chemical shift value the frame is tilted differently; each spin now has its own

set of co-ordinate axes. The Hamiltonian must be adjusted by applying (A.2):

$$e^{i\theta_{\mathrm{k}} I_{\mathrm{y}}} H^{(\mathrm{k})} e^{-i\theta_{\mathrm{k}} I_{\mathrm{y}}} = \sqrt{\omega_{\mathrm{k}}^2 + u_{\mathrm{k}}^2} I_{\mathrm{z}} + (2v_{\mathrm{k+1}}(t)\cos(f_{\mathrm{k+1}}t) + 2u_{\mathrm{k+1}}(t)\sin(f_{\mathrm{k+1}}t))I_{\mathrm{y}}$$

The time-invariant part of the field is now along the z-axis, and the time-varying part of the field is along the y-axis. The next step is to construct a rotating frame about the new z-axis (as in Figure 2.1B), where the rotation rate is $f_{\mathrm{k+1}}$. That is, the rotating frame precession rate is the same as the modulation frequency of $v_{\mathrm{k}}(t)$. This is captured by the time-dependent rotation $\exp(-if_{\mathrm{k+1}}tI_{\mathrm{z}})$ applied to the system. under (A.2) the Hamiltonian becomes

$$\begin{aligned} H^{(\mathrm{k+1})} =& (\sqrt{\omega_{\mathrm{k}}^2 + u_{\mathrm{k}}^2} - f_{\mathrm{k+1}})I_{\mathrm{z}} + \\ & (2v_{\mathrm{k+1}}(t)\cos(f_{\mathrm{k+1}}t) + 2u_{\mathrm{k+1}}(t)\sin(f_{\mathrm{k+1}}t))(\cos(f_{\mathrm{k+1}}t)I_{\mathrm{y}} + \sin(f_{\mathrm{k+1}}t)I_{\mathrm{x}}) \end{aligned}$$

Finally, the terms in the x-y plane are decomposed into slowly and rapidly oscillating parts. Specifically, terms modulated by a sinusoid with frequency $2f_{\mathrm{k+1}}$ are considered *fast*, and the other terms are considered *slow*. This assumes that the frequencies f_{k} are strictly decreasing with frame number.

The rapidly oscillating terms average to zero over relatively short timescales, so their net effect is small compared to the slower terms. For the purpose of developing a design algorithm, these fast terms are neglected. This is the rotating wave approximation (Ernst et al. 1987). However, the approximation is being made for terms that are kHz from resonance, whereas it is most usually evoked for terms that MHz off resonance. Therefore its validity for this pulse design method is addressed in detail in Chapter 3. For now, the rotating wave approximation is applied uncritically so that the current line of thinking can be pursued.

Under this approximation,

$$H^{(\mathrm{k}+1)} = (\sqrt{\omega_{\mathrm{k}}^2 + u_{\mathrm{k}}^2} - f_{\mathrm{k}+1})I_{\mathrm{z}} + u_{\mathrm{k}+1}(t)I_{\mathrm{x}} + v_{\mathrm{k}+1}(t)I_{\mathrm{y}} \tag{2.3}$$

The I_{z} component is the effective chemical shift in frame k+1, so the original chemical shift bandwidth/band-structure is mapped to a new *effective* bandwidth/band-structure. (2.3) is equivalent to (2.1) and (2.2).

The recursion $v_{\mathrm{k}}(t) = 2v_{\mathrm{k}+1}(t)\cos(f_{\mathrm{k}+1}t) + 2u_{\mathrm{k}+1}(t)\sin(f_{\mathrm{k}+1}t)$ is repeated arbitrarily many times in order to repeatedly apply (2.2) and reduce the effective bandwidth. This is terminated by a final-frame spin-locking (constant) pulse of strength v_{n} about the final-frame y-axis. This means that the pulse is of the form

$$\begin{aligned} u_0(t) &= u_0 \\ v_0(t) &= \overbrace{2u_1\sin(f_1t) + 4u_2\cos(f_1t)\sin(f_2t) + 8u_3\cos(f_1t)\cos(f_2t)\sin(f_3t) + \ldots}^{\text{bandwidth reduction}} \\ &\quad + \underbrace{2^{\mathrm{n}}v_{\mathrm{n}}\cos(f_1t)\cos(f_2t)\ldots\cos(f_nt)}_{\text{final-frame spin-locking}} \end{aligned} \tag{2.4}$$

The RF amplitude $A(t)$ and phase $\phi(t)$ are then

$$\begin{aligned} A(t) &= \sqrt{u_0^2 + v_0^2(t)} \\ \phi(t) &= \mathrm{atan2}(v_0(t),\ u_0) \end{aligned}$$

where atan2 is the two-argument arctangent function. The amplitude and phase profiles can be finely discretized and straightforwardly programmed into a spectrometer.

The design task is to choose the pulse amplitudes $\{u_{\mathrm{k}}\}$ and modulation frequencies $\{f_{\mathrm{k}}\}$ (the latter are also rotating frame precession rates) such that the recursion (2.2) transforms a large chemical shift bandwidth into a small effective bandwidth. Sections 2.1.3 and 2.1.4

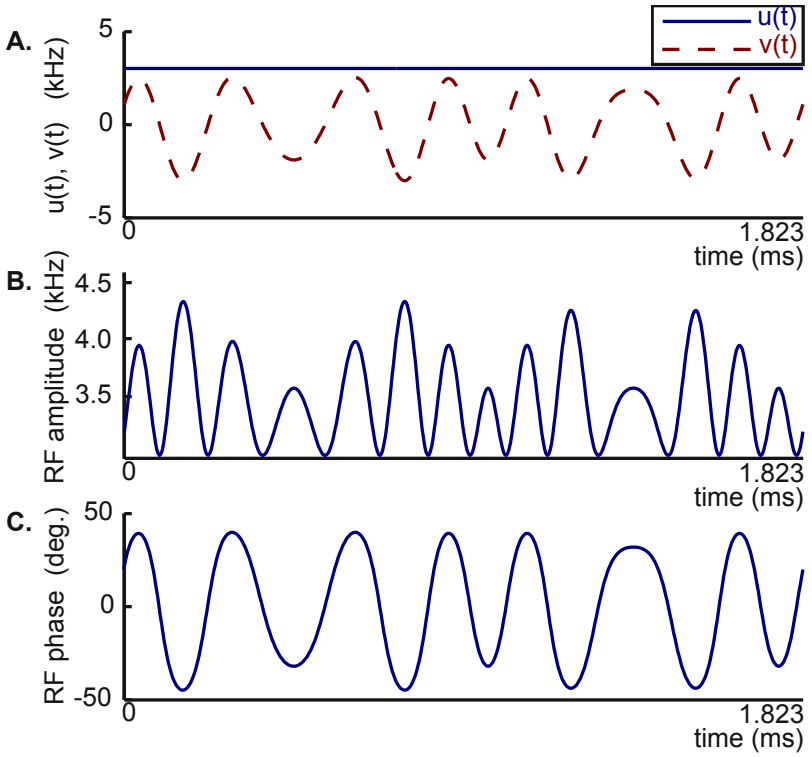

Figure 2.2: A pulse designed using three tilted, rotating frames. **A.** The Cartesian components have a static x-component and a y-component comprising multiple modulations, according to (2.4). The equivalent amplitude (**B.**) and phase (**C.**) functions are generated from the Cartesian functions $u(t)$ and $v(t)$. The root-mean-square amplitude of the pulse is 3.5 kHz. The pulse parameters for this example are given in Table 2.1.

show how to choose these free parameters. Each application of (2.2) further compresses the effective chemical shift range. Figure 2.1C is a schematic of the design process.

Figure 2.2 shows a typical pulse profile, for a pulse designed using three tilted, rotating frames. The parameters are summarized in Table 2.1. For the specific case of three rotating frames, the pulse shape is given explicitly by

$$\begin{aligned} u_0(t) &= u_0 \\ v_0(t) &= 2u_1 \sin(f_1 t) + 4u_2 \cos(f_1 t) \sin(f_2 t) + 8v_3 \cos(f_1 t) \cos(f_2 t) \cos(f_3 t) \end{aligned}$$

	$k=0$	1	2	3
u_k/v_3	3.0254	0.9460	0.5381	$v_3 = 0.1371$
f_k	-	3.8392	1.0969	0.5485
Tf_k	-	7	2	1

Table 2.1: Pulse amplitudes and frequencies (in kHz) for the pulse shape depicted in Figure 2.2. The pulse time is $T = 1.823$ ms and the root-mean-square RF power is 3.5 kHz. These four amplitudes and three frequencies, along with the pulse time, completely determine the pulse shape via (2.4). The pulse can be repeated to achieve spin-locking for longer periods of time, or scaled to another RF power level.

2.1.3 Frame alignment and choice of modulation frequencies

For each possible value of ω sampled from the original bandwidth, a series of frame changes is used to bring about (2.2). In this subsection, it is shown that if the rotation rates (i.e. pulse modulation frequencies) occur in integer multiples, then the net rotation of the state about the y-axis achieved in the final frame is also valid in the original frame.

The set of frame changes are each characterized by a unitary matrix $U_{\mathrm{k+1,k}}(\omega_\mathrm{k}, t)$, where explicit dependence on the pulse parameters has been omitted. This matrix transforms the Hamiltonian and quantum state (density matrix) from frame k to frame k+1. These time-varying frame changes are defined differently for each chemical shift value. This is repeated several times, so that (2.2) can be applied sufficiently many times to reduce the effective bandwidth. $U_{\mathrm{k+1,k}}(\omega_\mathrm{k}, t)$ comprises a tilt about the y-axis by $\theta_\mathrm{k} = \mathrm{atan2}(u_\mathrm{k}, \omega_\mathrm{k})$, followed by a rotation about the z-axis at rate $f_{\mathrm{k+1}}$:

$$U_{\mathrm{k+1,k}}(\omega_\mathrm{k}, t) = \exp(-if_{\mathrm{k+1}}tI_\mathrm{z})\exp(i\theta_\mathrm{k}I_\mathrm{y})$$

The transform from the original frame to the k^{th} rotating frame is composed of k such matrices:

$$U_{\mathrm{k,0}}(\omega, t) = U_{\mathrm{k,k\text{-}1}}(\omega_{\mathrm{k}-1}, t)U_{\mathrm{k\text{-}1,k\text{-}2}}(\omega_{\mathrm{k\text{-}2}}, t)...U_{1,0}(\omega, t)$$

For an arbitrary time t, the rotation axis for $U_{\mathrm{n},0}$ differs for different values of ω. However, suppose that all rotation frequencies obey $f_{\mathrm{k}}T = 2m_{\mathrm{k}}\pi$, where T is the pulse time and $\{m_{\mathrm{k}}\}$ are integers. In this case,

$$U_{\mathrm{k},0}(\omega, 0) = U_{\mathrm{k},0}(\omega, T) = \exp(i\sum_{\mathrm{j}=1}^{\mathrm{k}} \theta_{\mathrm{j}} I_{\mathrm{y}}) \tag{2.5}$$

which is a net tilt about the y-axis, regardless of the values of the tilt angles. The rotation axis does not depend on the effective chemical shifts in each constructed frame $\{\omega_1,\ \omega_2, \ldots, \omega_{\mathrm{k}}\}$, nor on the intrinsic chemical shift ω. This ensures that at the beginning and end of the pulse, the y-axis of each multi-tilted, multi-rotating frame is aligned with the y-axis in the original frame. However, during the pulse the frames are generally mis-aligned for different chemical shift values.

There are now two conditions on the choice of modulation frequencies: they occur in integer multiples (for frame alignment) and they decrease sufficiently quickly with each new frame that terms suppressed under the rotating wave approximation always oscillate faster than terms that are not suppressed. These conditions can be satisfied if $f_{\mathrm{k}+1}$ is at least twice as large as f_{k}. Examples are $f_4, \ldots, f_1 \propto 1, 2, 4, 8$ or $1, 2, 5, 10$, or $f_3, f_2, f_1 \propto 1, 2, 7$.

2.1.4 Choice of pulse amplitudes

In this section, a recursion for the pulse amplitudes is derived. Each additional tilted, rotating frame is used to further manipulate the effective bandwidth. In order to construct each new frame it is necessary to include a further sinusoidal modulation to the pulse. Therefore, the complete pulse comprises nested modulations. The y-component of the pulse profile obeys the recursion

$$v_{\mathrm{k}-1}(t) = 2v_{\mathrm{k}}(t)\cos(f_{\mathrm{k}}t) + 2u_{\mathrm{k}}\sin(f_{\mathrm{k}}t)$$

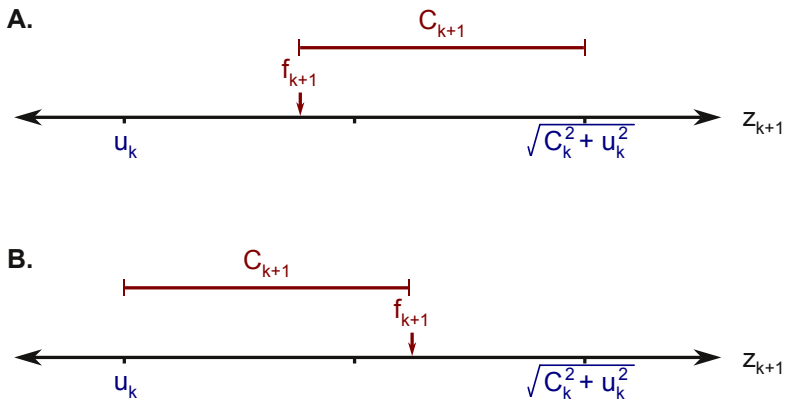

Figure 2.3: Choice of modulation frequencies. The bandwidth ($2C_{\mathrm{k+1}}$) must stretch from resonance ($\omega_{\mathrm{k+1}} = f_{\mathrm{k+1}}$) to the upper and lower limits of the calculated range of effective chemical shifts. For a fixed RF amplitude allocation u_{k}, the greatest reduction in effective bandwidth is achieved by using $f_{\mathrm{k+1}}$ to center the bandwidth, $f_{\mathrm{k+1}} = 0.5(\sqrt{C_{\mathrm{k}}^2 + u_{\mathrm{k}}^2} + u_{\mathrm{k}})$. **A.** The modulation frequency is lower than the middle of the range, and $C_{\mathrm{k+1}}$ must stretch to the upper limit. **B.** The modulation frequency is higher than the middle of the range, and $C_{\mathrm{k+1}}$ must stretch to the lower limit.

where $\{u_1, u_2, \ldots, u_{\mathrm{n}}\}$, v_{n}, and $\{f_1, f_2, \ldots, f_{\mathrm{n}}\}$ are design parameters. Finally, v_{n} is chosen to be constant and $u_{\mathrm{n}} = 0$. The Hamiltonian in the n^{th} frame is

$$H^{(\mathrm{n})} = \omega_{\mathrm{n}} I_{\mathrm{z}} + v_{\mathrm{n}} I_{\mathrm{y}}$$

If $|\omega_{\mathrm{n}}| \ll |v_{\mathrm{n}}|$ (that is, if differences in effective offset frequency have indeed been eliminated by the multi-frame process) then $\alpha = v_{\mathrm{n}} T$ is the flip angle about the y-axis.

Let $|\omega_{\mathrm{k}}|$ be upper bounded by C_{k}, so that the bandwidth in frame k is $2C_{\mathrm{k}}$. Suppose (2.2) is to be used to drive a large original bandwidth $|\omega_0| \leq C_0$ to a small final bandwidth $|\omega_{\mathrm{n}}| \leq C_{\mathrm{n}} \ll C_0$. Inspection of (2.2) reveals the minimum and maximum values of the effective chemical shift in the next frame: $\omega_{\mathrm{k+1}} \in [|u_{\mathrm{k}}| - f_{\mathrm{k+1}},\ \sqrt{C_{\mathrm{k}}^2 + u_{\mathrm{k}}^2} - f_{\mathrm{k+1}}]$. Clearly, $C_{\mathrm{k+1}}$ must be larger than both the lower and upper limits of $\omega_{\mathrm{k+1}}$, as depicted in Figure 2.3.

The frequency is chosen from somewhere between u_k and $\sqrt{C_k^2 + u_k^2}$:

$$f_{k+1} = \alpha u_k + (1 - \alpha)\sqrt{C_k^2 + u_k^2} \tag{2.6}$$

where α is between zero and one. Putting this together with the the range for ω_{k+1} shows that

$$C_{k+1} = \begin{cases} \sqrt{C_k^2 + u_k^2} - f_{k+1} & \text{if } \alpha \geq 0.5 \\ f_{k+1} - u_k & \text{if } \alpha \leq 0.5 \end{cases} \tag{2.7}$$

In these two expressions for C_{k+1}, the term f_{k+1} has opposite sign. For the case of $\alpha \geq 0.5$, the new bandwidth is decreased by increasing f_{k+1} to its maximum (achieved when $\alpha = 0.5$). Similarly, for the case of $\alpha \leq 0.5$, the bandwidth is decreased by *de*creasing f_{k+1} to its minimum (also achieved when $\alpha = 0.5$). Therefore, for a fixed RF amplitude allocation u_k, the greatest reduction in effective bandwidth is achieved by using f_{k+1} to center the bandwidth, i.e. $\alpha = 0.5$. This is illustrated in Figure 2.3. In this case,

$$f_k = \frac{\sqrt{C_{k-1}^2 + u_{k-1}^2} + |u_{k-1}|}{2} \tag{2.8}$$

$$C_k = \frac{\sqrt{C_{k-1}^2 + u_{k-1}^2} - |u_{k-1}|}{2} \tag{2.9}$$

Thus, the parameters in frame k can be calculated from the parameters in frame k - 1. This can be reversed so that parameters in frame k can be calculated from those in frame k + 1. Then the appropriate pulse amplitudes $\{u_k\}$ to achieve the desired effective bandwidth are given by a simple recursion, which runs *backwards* in frame number k:

$$C_{k-1} = 2\sqrt{f_k C_k} \tag{2.10}$$

$$|u_{k-1}| = |f_k - C_k| \tag{2.11}$$

The recursion is fixed by choice of C_{n} (maximum allowable offset in frame n) and frequencies $\{f_1, f_2, \ldots, f_{\mathrm{n}}\}$. Clearly, it must be required that $C_{\mathrm{n}} \ll |v_{\mathrm{n}}|$ to execute a uniform rotation (flip angle $\alpha = v_{\mathrm{n}}T$) around the y-axis over the bandwidth C_0 in the original frame of reference. For a chosen set of modulation frequencies and a desired effective bandwidth C_{n}, the pulse amplitudes $\{u_{\mathrm{k}}\}$ and the active bandwidth in the original frame C_0, are specified by (2.10) and (2.11). The pulse designer should choose the number of frames and the set of frequencies to achieve a satisfactory active bandwidth.

In the final frame, a uniform rotation about the y-axis is executed. The purpose of this is to spin-lock small residual chemical shifts and other unwanted drift terms in the Hamiltonian, for example correction terms arising from the neglect of rapidly oscillating fields. For a density matrix expressed in the final frame $\rho^{(\mathrm{n})}(0) = I_{\mathrm{y}}$, then for all time $\rho^{(\mathrm{n})}(t) = I_{\mathrm{y}}$; the nuclei are spin-locked to the y-axis (this assumes the final-frame spin-lock pulse is strong compared to any residual fields). Moreover, since the y-axes in all tilted, rotating frames are aligned at time T, it is also the case that $\rho(0) = \rho(T) = I_{\mathrm{y}}$ in the original frame of reference ($k = 0$). That is, at the beginning and end of the pulse all spins are in phase along the y-axis (they are not in phase *during* the pulse). For example, Figure 2.4A shows via simulation how magnetization returns to in-phase along the y-axis after the pulse for a range of chemical shift values.

In a sense, the frame changes have been used to simplify the calculation of the effective Hamiltonian (Haeberlen and Waugh 1968). As is the case for average Hamiltonian theory (Llor 1992; Haeberlen 1976), the Magnus expansion (Magnus 1954; Klarsfeld and Oteo 1989), and the Floquet expansion (Floquet 1883; Leskes et al. 2010), a time-invariant effective Hamiltonian has been constructed which is valid at the endpoints of each time-period. However, this iterative scheme is not general; it is specific to the RF pulse form suggested. The advantage is that the pulse design proceeds recursively and analytically. Each free parameter can be chosen in turn by consideration of (2.2) (and (4.1) for coupled spins, as

explained in Chapter 4), without using the full Magnus or Floquet machinery. Rather, the multi-frame method depends on some of the most fundamental and familiar NMR concepts (Cavanagh et al. 2007; Ernst et al. 1987)—choice of axes, rotating frames, the rotating wave approximation, sinusoidally modulated fields—to construct a time-varying RF pulse under which the effective time-invariant Hamiltonian has the desired form.

2.2 Robustness to RF inhomogeneity

Up to this point, the desired control fields have been specified *exactly*. In fact, it is more realistic to assume that their amplitude varies across the sample because of RF inhomogeneity, as described in Section 1.2.2. In this section, the effects of RF inhomogeneity during a multi-frame pulse are assessed.

Although the multi-frame method does not explicitly account for RF inhomogeneity, insensitivity to RF power variations in computer simulations are observed (as shown in Figure 2.4A) along with good performance in experiments for all pulses that were designed and tested, suggesting that RF inhomogeneity is not ruining the multi-frame scheme. This can be understood by consideration of a slightly modified version of (2.2)—even under RF inhomogeneity, there is still a similar systematic frame-by-frame reduction in effective chemical shift bandwidth.

In the presence of RF inhomogeneity all pulse amplitudes used in the calculation of effective chemical shifts should be scaled by σ_{RF}, an inhomogeneity factor sampled from a neighborhood of unity, e.g. $\sigma_{\mathrm{RF}} \in [0.9,\ 1.1]$. In particular, (2.2) would be instead

$$\omega_{\mathrm{k}} = \sqrt{\omega_{\mathrm{k-1}}^2 + \sigma_{\mathrm{RF}}^2 u_{\mathrm{k-1}}^2} - f_{\mathrm{k}} \tag{2.12}$$

This changes the calculated values of $\{\omega_{\mathrm{k}}\}$. Figure 2.4B shows an example of the recalculated

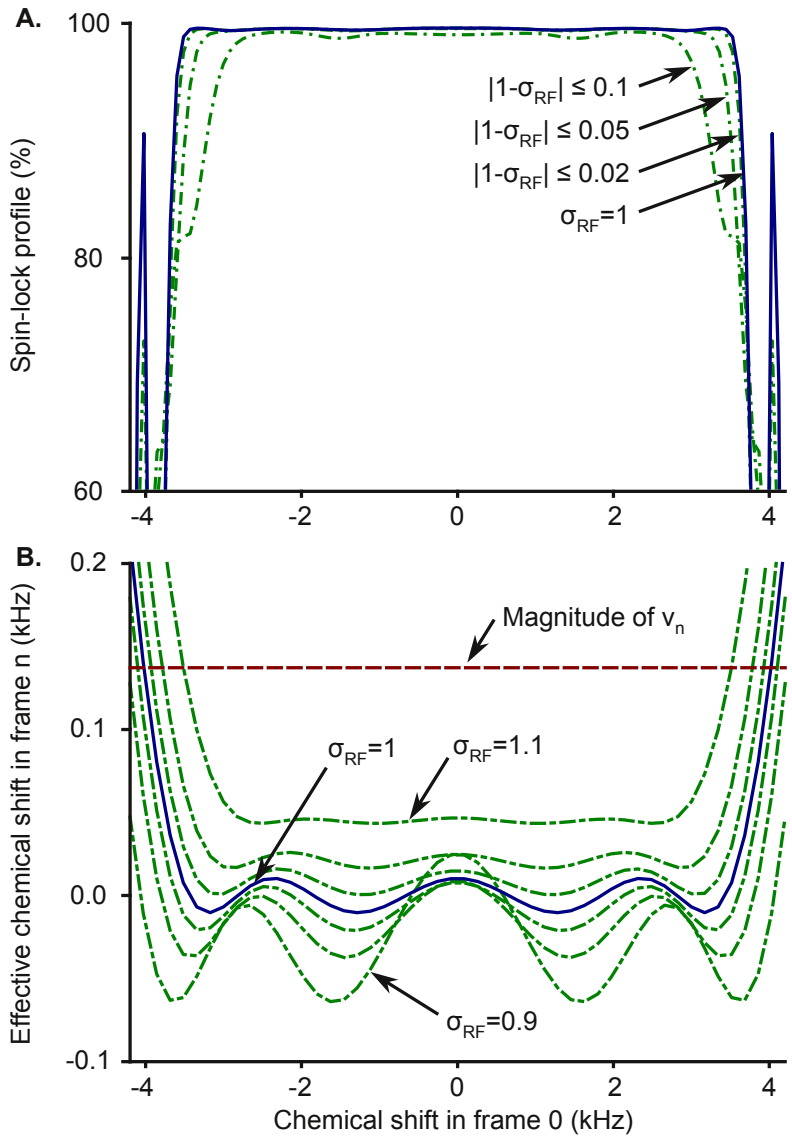

Figure 2.4: The effect of RF inhomogeneity on the final frame chemical shift. **A.** The pulse given in Table 2.1 is simulated for spin-locking of an ensemble of isolated spins-1/2. The initial state, and final measurement operator, are I_y. The profile is averaged over 20 values of the RF inhomogeneity, sampled uniformly between $\pm 2\%$, $\pm 5\%$, or $\pm 10\%$ (dot-dashed lines) of the nominal power. The profile at the nominal power (solid line) is also depicted. Magnetization is returned to near the y-axis at the end of the pulse over a large bandwidth. The duration is $4T = 7.2923$ ms (i.e. the pulse was repeated four times), and the power is 3.5 kHz. **B.** The recursion (2.12) is applied for $\sigma_{\mathrm{RF}} = 1$ (solid line) and $\sigma_{\mathrm{RF}} = 0.9$, 0.95, 0.98, 1.02, 1.05, and 1.1 (dot-dashed lines). The magnitude of the effective spin-lock field applied in the final frame is shown for comparison (dashed line). Even in the presence of large RF inhomogeneity, the effective bandwidth is reduced significantly and remains smaller than the spin-lock field over a wide bandwidth.

final-frame values. Since the algorithm is, by design, robust to variations in effective chemical shift in each frame, this change does not prevent adequate performance for $\sigma_{\mathrm{RF}} \approx 1$. The recalculated ω_{k} will typically remain within the design bandwidth $|\omega_{\mathrm{k}}| \leq C_{\mathrm{k}}$. The exception is at the edges of the bandwidth in frame k–1, where the (recalculated) effective chemical shift ω_{k} could fall outside of the design bandwidth C_{k}. Chemical shifts slightly outside of the design bandwidth are still reduced via subsequent frame changes; nonetheless, this effect is a source of error. RF inhomogeneity leads to larger than desired final-frame effective chemical shifts; however, simulations (e.g. Figure 2.4A) and experiments confirm that the effect is small.

The spin-locking n^{th} frame Hamiltonian is now $H^{(\mathrm{n})} = \omega_{\mathrm{n}} I_{\mathrm{z}} + \sigma_{\mathrm{RF}} v_{\mathrm{n}} I_{\mathrm{y}}$. This will still achieve spin-locking provided the (recalculated) effective chemical shift remains small compared to $|v_{\mathrm{n}}|$.

2.2.1 Modified design for RF inhomogeneity

The design algorithm can be modified to explicitly account for dispersion in RF field strength. The starting point is the range of offsets in frame k+1,

$$\omega_{\mathrm{k}} \in [(1-\Delta)|u_{\mathrm{k-1}}| - f_{\mathrm{k}},\ \sqrt{C_{\mathrm{k-1}}^2 + (1+\Delta)^2 u_{\mathrm{k-1}}^2} - f_{\mathrm{k}}]$$

where Δ is the maximum difference of RF inhomogeneity from one, e.g. $\Delta = 0.1$. Note that the lower limit used the minimum power and the upper limit uses the maximum power. The range is the difference in these limits, and the modulation frequency is chosen in the center of the range,

$$C_{\mathrm{k+1}} = 0.5 \left[\sqrt{C_{\mathrm{k-1}}^2 + (1+\Delta)^2 u_{\mathrm{k-1}}^2} - (1-\Delta)|u_{\mathrm{k-1}}| \right]$$
$$f_{\mathrm{k+1}} = 0.5 \left[\sqrt{C_{\mathrm{k-1}}^2 + (1+\Delta)^2 u_{\mathrm{k-1}}^2} + (1-\Delta)|u_{\mathrm{k-1}}| \right]$$

Equivalently,

$$u_{\mathrm{k}} = \frac{1}{1-\Delta}|f_{\mathrm{k}+1} - C_{\mathrm{k}+1}|$$
$$C_{\mathrm{k}} = 2\sqrt{f_{\mathrm{k}+1}C_{\mathrm{k}+1} - \Delta u_{\mathrm{k}}^2}$$

The new term $-\Delta u_{\mathrm{k}}^2$, which was not present in the original recursion (2.11), serves to limit the growth of bandwidth as k decreases. Clearly, for earlier (small k) frames—where the bandwidths and modulation frequencies are large compared to the applied fields—the effect is not very pronounced. However, for the later (large k) frame changes, bandwidths have already been substantially reduced, and the new term is crucial. In fact, if the final frame bandwidth is chosen too small, then $C_{\mathrm{n}-1}$ does not have a real value. The desired final frame bandwidth C_{n} can be increased until $C_{\mathrm{n}-1}$ is real.

In practice, to achieve a large bandwidth C_0 with the modified algorithm, the final frame bandwidth must be made quite large. Therefore, the modified recursions are of little practical benefit. On one hand, the original design algorithm can be used (and RF inhomogeneity ignored). Then the effective final-frame chemical shifts are increased once RF inhomogeneity is assessed via (2.12). On the other hand, the modified design method can be explicitly used, but the recursions are initiated with a larger effective bandwidth C_{n}. There is little difference in practice.

2.3 Scaling of power, pulse time, and bandwidth

This section is about the relative scaling of bandwidth, applied power, and pulse time as more rotating frame constructions are added.

For each frame change, f_{k} can be chosen to at least halve the effective bandwidth, irrespective of the amplitude allowance $|u_{\mathrm{k}-1}|$. This is because (2.9) implies $C_{\mathrm{k}+1} \leq C_{\mathrm{k}}/2$. Therefore $C_{\mathrm{k}} \geq 2^{\mathrm{n}-\mathrm{k}}C_{\mathrm{n}}$, so that the effective bandwidth C_{n} decays exponentially with the

number of tilted, rotating frames. However, each frame change adds an extra modulation to (2.4), which increases the average amplitude of the RF pulse. The root-mean-square average amplitude A of the RF pulse can be calculated from (2.4):

$$\begin{aligned} A^2 &= \frac{1}{T}\int_0^{\mathrm{T}} u^2(t) + v^2(t)dt \\ &= u_0^2 + 2u_1^2 + 4u_2^2 + \cdots + 2^{\mathrm{n}-1}u_{\mathrm{n}-1}^2 + 2^{\mathrm{n}}v_{\mathrm{n}}^2 \end{aligned} \tag{2.13}$$

Since $(u_{\mathrm{k}}, v_{\mathrm{k}}(t))$ is the effective RF pulse applied in frame k, it is natural to define A_{k}^2 as the RF power in frame k, which obeys

$$A_{\mathrm{k}}^2 = 2A_{\mathrm{k}+1}^2 + u_{\mathrm{k}}^2 \tag{2.14}$$

LIMITS: With large numbers of frames the pulse can, according to (2.10) and (2.11), cover bandwidths that greatly exceeds the applied power. In this regime $C_{\mathrm{k}} \gg u_{\mathrm{k}}$. Then (2.9) can be approximated by $C_{\mathrm{k}+1} = 2C_{\mathrm{k}}$. Moreover, the share of total RF power that is applied in an individual frame must be vanishingly small. Therefore (2.14) becomes $A_{\mathrm{k}}^2 \approx 2A_{\mathrm{k}+1}^2$, and

$$\frac{C_{\mathrm{k}}}{A_{\mathrm{k}}} \sim O(2^{-\mathrm{k}/2}) \tag{2.15}$$

This suggests that the for a desired final frame bandwidth C_{n} and power allowance A_0, the operating bandwidth C_0 can be increased without limit by adding more frames. However, the pulse time T must obey $2\pi = f_{\mathrm{n}}T$. It is clear from inspection of 2.8 and 2.9 that in the regime where $C_{\mathrm{k}} \gg u_{\mathrm{k}}$, modulation frequency scales with bandwidth. Since the frequencies must obey $f_{\mathrm{k}} \leq 2^{-\mathrm{k}} f_1$ and the pulse duration T is inversely proportional to f_{n}, both pulse time and bandwidth C_0 grow at order $2^{\mathrm{k}/2}$. This means that for a fixed power level, very large bandwidth comes at the expense of long pulse duration.

n	T (ms)	Design C_0 (kHz)	Simulation C_0 $\geq 95\%$ (kHz)	Simulation C_0 $\geq 99\%$ (kHz)	Simulation C_0 $\geq 99.9\%$ (kHz)
5	4.695	5.8	5.7	5.7	3.1
6	6.850	8.8	7.1	6.7	4.5
7	9.841	12.6	12.2	9.9	6.9
8	14.028	18.0	16.2	13.7	10.9
9	19.918	25.5	22.4	19.0	14.5
10	28.224	36.0	30.0	24.5	19.0
11	39.954	51.1	45.2	36.0	29.9

Table 2.2: Spin-locked bandwidth with a high number of rotating frames. High spin-locking bandwidths can be achieved with n ≥ 5 frames. The spin-locking is simulated for a full 2π rotation about y-axis, i.e. for duration $4T$ where T is the pulse time. The simulated spin-lock profile degrades near the edges of the bandwidth, so the chemical shift offsets at which the spin-locking becomes less than 95%, 99%, and 99.9% efficient are also recorded. The pulse power is 2 kHz in all cases. The best-fit growth rates for the bandwidth are $2^{0.52n}$ (design bandwidth), $2^{0.50n}$ (95% efficient spin-locking), $2^{0.47n}$ (99% efficient spin-locking), and $2^{0.45n}$ (99.9% efficient spin-locking). These rates are in reasonable agreement with (2.15).

Simulation results: The scaling of bandwidth, RF power, and pulse duration can also be explored numerically. Figure 2.5 shows how in-phase magnetization returns to the y-axis over a large bandwidth of chemical shifts for high numbers of rotating frames. The pulses were designed to have $v_{\mathrm{n}}/C_{\mathrm{n}} = 9$, total power 2 kHz, flip angle $\alpha = v_{\mathrm{n}}T = \pi/2$, and frequencies $f_{\mathrm{k}} = 2f_{\mathrm{k+1}}$. All remaining parameters are fixed by (2.10) and (2.11). The pulses are run four times, for a total rotation of 2π around the y-axis. The Subfigures 2.5A and 2.5B show the proportion of magnetization that returns to its starting point as a function of chemical shift offset.

Due to degraded performance near the edges of the bandwidth, the smallest offset frequencies for which less than 95%, 99%, and 99.9% of the magnetization returns to the y-axis were measured, and are summarized in Table 2.2 and Subfigure 2.5C. Regardless of which efficiency level is used, the bandwidth-to-RF power ratio approximately follows (2.15) for at least eleven frames. Clearly, spins can be locked to the y-axis over very large bandwidths with multi-frame pulses, however the durations of these pulses are too long for standard

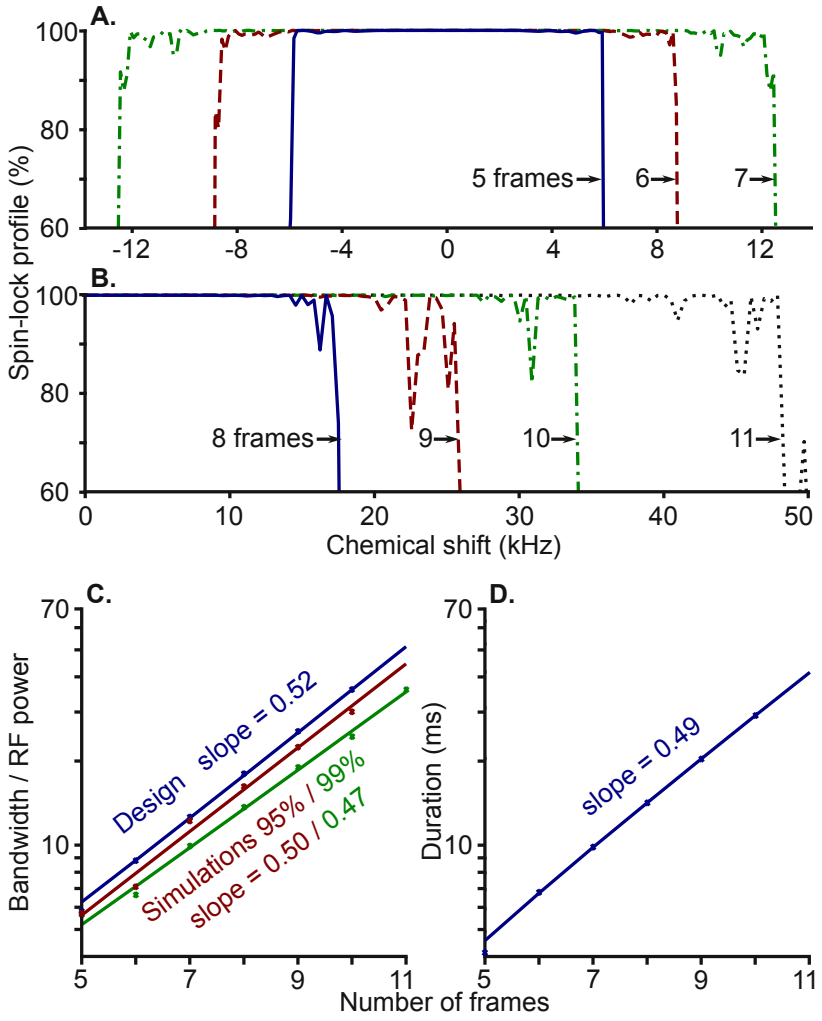

Figure 2.5: Spin-locking with a high number of rotating frames. **A.** Spin-locking performance for pulses with 5–7 modulations. The pulse power is 2 kHz, and the simulation is for $4T$, where T is listed in Table 2.2. **B.** Spin-locking performance for pulses with 8–11 modulations (half of the profile is omitted). Extremely high bandwidth-to-RF power ratios are possible with sufficiently many rotating frames. For visual clarity, some off-resonance effects outside of the displayed bandwidths were removed from each trace. **C., D.** The growth of bandwidth and pulse duration are around $\sim 2^{n/2}$ where n is the number of frames. The design bandwidth is plotted, along with the width of spectral regions for which spin-locking is 95% and 99% efficient (these data are recorded in Table 2.2). The bandwidth appears to continue growing for high numbers of frames. The long durations of these pulses make them impractical for mixing experiments in protein NMR.

applications in protein NMR.

Practical design: With 3 to 5 changes of frame, (2.10) and (2.11) yield pulses with bandwidth-to-RF amplitude ratios ($2C_0/A$) of two or higher. Pulse times T are on the order of milliseconds. Therefore, the pulse can be looped several times to get the appropriate mixing times for protein spectroscopy (order tens of milliseconds), cover the appropriate bandwidth (order kHz or tens of kHz), and obey average and peak RF amplitude limits (order kHz).

In Chapter 4 it will be demonstrated that with 3 to 5 changes of frame the J-coupling can be largely maintained between any two spins sampled from the bandwidth. Standard mixing pulses have bandwidth-to-RF amplitude ratios of about two (Glaser and Quant 1996). Therefore, for the same average RF amplitude larger mixing bandwidth can be achieved using a pulse designed using tilted, rotating frames.

At typical RF power levels for carbon channel TOCSY experiments, the use of more than 5 rotating frames will produce a pulse time of tens of milliseconds. This means it is difficult to match the desired mixing time, i.e. the pulse may be shorter than the required mixing time, but when repeated twice it may be longer than the required mixing time. Furthermore, with this many frames it is difficult to maintain the J-coupling between all possible spin pairs in the bandwidth. This is explored in more detail in Chapter 4.

2.4 Spin-locking over multiple frequency bands

When the chemical shift frequencies of interest fall into distinct, widely separated spectral regions, RF power can be saved by ignoring the empty parts of the spectrum and targeting the interesting frequency bands. For example, the carbon chemical shifts in protein samples fall into several distinct bands (Cavanagh et al. 2007), so it is sufficient to transfer polarization between and within these bands; there is no need to satisfy the Hartmann-Hahn mixing

condition in the unpopulated parts of the spectrum. Also, multi-band pulses can be used to resolve patticular patterns of interest by selectively excluding certain resonances from the effective spin network. In this section, (2.2) is used to effectively collapse and simplify a multi-band structure, so that the effective Hamiltonian can satisfy the Hartmann-Hahn condition over several distinct bands.

There were two major obstacles encountered in previous attempts to design homonuclear multi-band pulses: cross talk between bands, so that the bands had to be far apart (Grzesiek and Bax 1995; Carlomagno et al. 1996), and the restriction to equally wide, symmetric bands (Carlomagno et al. 1997). In fact, the multi-frame method can overcome both of these difficulties.

2.4.1 Simple dual-band pulses by removing u_{K}

Dual-band mixing pulses have previously been designed by adding an extra sinusoidal modulation to Gaussian inversion pulses (Carlomagno et al. 1996; Zuiderweg et al. 1996) or to the WALTZ-16 sequence (Grzesiek and Bax 1995), or in solid state NMR by adding an extra modulation to a spin-lock field (Zhang et al. 2012). This idea also arises naturally in the context of the multi-rotating frame method, where (2.4) shows that if u_{k} is set to zero then

$$v_{\mathrm{k}-1} = 2v_{\mathrm{k}}(t)\cos(f_{\mathrm{k}}t)$$

That is, an extra sinusoidal modulation is applied to an existing TOCSY pulse ($v_{\mathrm{k}}(t)$) to produce another pulse ($v_{\mathrm{k}-1}(t)$). The resulting pulse can be demodulated in frames rotating at either $+f_{\mathrm{k}}$ or $-f_{\mathrm{k}}$, so that the pulse is on-resonance with chemical shifts near both of these frequencies.

This idea can be used to engineer a dual-band pulse to match a particular experimental situation. Suppose that in frame k there are two equally wide bands of interest. The

frequency f_{k} can be chosen halfway between the midpoints of these bands, so that $|\omega_{\mathrm{k}}| \in [a,\ b]$, where $b > a > 0$. For dual-band structures in the original frame ($\mathrm{k} = 0$), this amounts to setting the carrier frequency for the pulse halfway between the bands. Next, set $u_{\mathrm{k}} = 0$ and $f_{\mathrm{k+1}} = (a+b)/2$. Applying (2.2)

$$\begin{aligned} \omega_{\mathrm{k+1}} &= |\omega_{\mathrm{k}}| - (a+b)/2 \\ &\in [(a-b)/2,\ (b-a)/2] \end{aligned}$$

Then $C_{\mathrm{k+1}} = (b-a)/2$. In frame k+1, there is a single band centered around $\omega_{\mathrm{k+1}} = 0$, with $|\omega_{\mathrm{k+1}}| \leq C_{\mathrm{k+1}}$. If this band is wide then further tilted, rotating frames can be constructed in order to reduce it. Alternatively, if this band contains more empty spectral regions, two of these regions can be overlaid in frame k+2, and so on. In this way, it is possible to have two active bands in the original frame, or four, or eight, and so on. For example, setting both u_0 and u_1 to zero will generate a four-band pulse.

The bands can be moved arbitrarily far apart without using more RF amplitude or taking more time. To see this, observe that increasing $f_{\mathrm{k+1}}$ (to move the bands further apart) does not change the RF amplitude (2.13). The pulse time T depends on $f_{\mathrm{n}}T = 2\pi$ and the flip angle $\alpha = v_{\mathrm{n}}T$. Neither of these constraints are changed by increasing $f_{\mathrm{k+1}}$ (for $k+1 \neq n$).

The spin-locked bands can also be quite close together, relative to their bandwidths. Other dual-band pulse design schemes require the bands to widely spaced (e.g. with a gap that is at least three times the bandwidth), limiting their range of possible applications (Carlomagno et al. 1996; Zuiderweg et al. 1996).

Subfigures 2.6A and 2.6B show the effect of setting $u_0 = 0$ on the pulse's spin-locking profile. In particular, and in contrast to other dual-band pulse schemes, the spin-locked bands are close together relative to their bandwidths. The bands can easily be moved further apart by increasing the modulation frequency f_1.

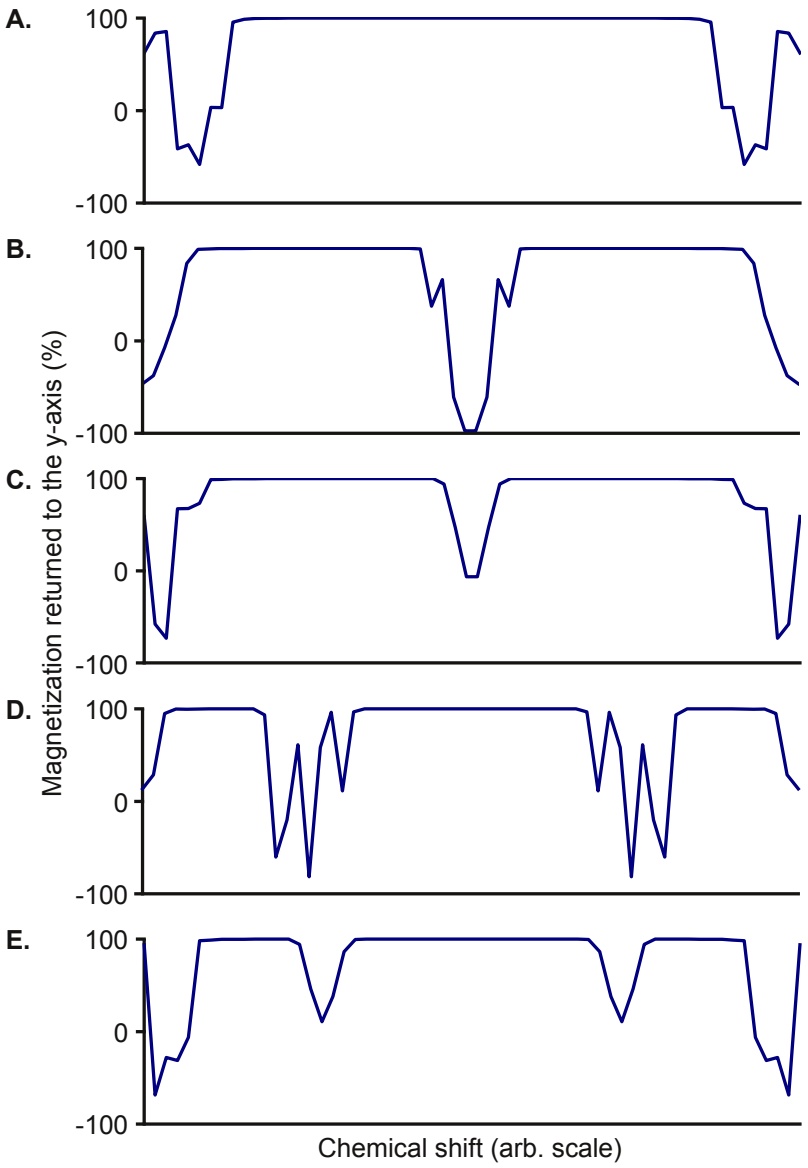

Figure 2.6: Simple dual-band and tri-band pulse design. **A.** A broadband pulse was designed using four rotating frames. The pulse parameters are given in Table 2.3. The bandwidth is approximately 3.5 times the average pulse amplitude. Here, the pulse was simulated four times in immediate succession and applied to a spin initially aligned with the y-axis. The proportion of magnetization along the y-axis at the final time is plotted. **B.** Setting $u_0 = 0$ produces a dual-band pulse. The bands can be moved further apart by increasing f_1. **C.** Scaling down $u_0 \to 0.5u_0$ also produces a dual-band pulse, but the bands are closer together. **D.** Setting $u_1 = 0$ produces a tri-band pulse. The spacings of the bands can be increased by increasing f_1 and f_2. **E.** Scaling down $u_1 \to 0.65u_1$ also produces a tri-band pulse, but the bands are closer together. All simulations were performed with average RF amplitude of 3 kHz, and chemical shifts between ± 7.5 kHz. However, the power can be scaled to match the desired bandwidth. Note that after removal/scaling of pulse amplitudes the total power was rescaled back to 3 kHz.

	$k=0$	1	2	3	4
$u_{\rm k}/v_4$	1.4369	1.1528	0.7871	0.4462	$v_4 = 0.1136$
f_k	-	3.6342	1.8171	0.9085	0.4543
Tf_k	-	8	4	2	1

Table 2.3: Pulse amplitudes and frequencies (in kHz) for the set of simple multiband pulses simulated in Figure 2.6. The parameters are given for the broadband version simulated in Figure 2.6A; the dual-band and tri-band pulses are created by scaling down one or both of u_0 and u_1. The pulse time is $T = 2.201$ ms. The final-frame spin-locking amplitude is $v_4 = \pi/(2T) = f_{\rm k}/4$, for a flip angle of $\pi/2$ about the y-axis. The RF power is 3 kHz.

2.4.2 Simple tri-band pulses by removing $u_{\rm K}$

Setting the first k pulse amplitudes to zero produces $2^{\rm k}$ equally wide bands. This is because a dual-band structure is generated in frame 0 by setting $u_0 = 0$, and then a further two bands are created in frame 1 by setting $u_1 = 0$, and so on. Of course, the pulse designer can choose to split the bandwidth into two parts in *any* subset of the n frames from k = 0 to k = n-1. For example, an easy way to make three spin-locking bands is to maintain the full bandwidth in frame 0 (by *not* adjusting u_0 from its value given by (2.11)), but to set $u_1 = 0$. This means that there are two bands in frame 1. Under (2.2), spins with large values positive of ω_1 have large *magnitude* ω, whereas spins with large negative values of ω_1 come from $\omega \approx 0$. Therefore, one of the bands in frame 1 spin-locks two distinct bands from frame 0: large positive ω and large negative ω. The other band in frame 1 spin-locks small magnitude ω. This makes three bands in frame 0 altogether. Therefore, a tri-band pulse can be designed simply by generating a set of pulse amplitudes $\{u_{\rm k}\}$ using the broadband multi-frame design algorithm, and setting $u_1 = 0$. The relative spacing of the bands in controlled by the first two modulation frequencies. The effect of setting $u_1 = 0$ is illustrated in Subfigure 2.6D.

Setting other pulse amplitudes (or sets of pulse amplitudes) to zero allows access to a rich space of band-structures. The relevant pulses can be generated almost instantly using

(2.10) and (2.11), and then removing some of the amplitudes. In practice, the easiest way to space the bands correctly is to simulate the pulse for a range of chemical shift frequencies, and then adjust the modulation frequencies to move bands further apart or closer together as desired. As with broadband pulses, the RF power can be scaled up or down to set the overall bandwidth.

Finally, note that none of the reasoning presented in this section crucially depends on *completely* removing any of the pulse amplitudes. Merely *scaling down* one or more of the pulse amplitudes will return a similar band-structure to the case where it was removed completely. This can, however, be used to put some of the bands closer together. Figure 2.6 catalogs some examples of band structures that can be generated by removing or scaling down some of the pulse amplitude from a four-frame broadband pulse.

2.4.3 Direct manipulation of Fourier components

The simple dual-band and tri-band pulses designed so far have spin-locking profiles that are symmetric about the carrier frequency of the pulse. However, the band structure of a practical sample will not necessarily fall into evenly spaced, equally wide bands. Therefore, it is worth exploring the design of multiband pulses with asymmetric bandwidths.

For example, in heteronuclear decoupling of the carbon channel it is desirable to simultaneously spin-lock aliphatic and aromatic carbon spins. These spins fall into two distinct, separated bands. However, the bandwidths are not equal. The aliphatic carbons occupy the spectral region 0–80 ppm, while the aromatics usually fall within the range 110–140 ppm. Therefore, a pulse with either a single spectral band or two equally wide bands will waste some power spin-locking a spectral range that contains no nuclei. Similarly, for mixing between the carbonyl and aliphatic regions, it is necessary to spin-lock the regions 0–80 ppm and 165–185 ppm.

Kupce and Freeman (1994) created dual-band pulses by taking a familiar broadband pulses

and editing it in the frequency domain (although they only produced symmetric spin-locking profiles). The motivation was to avoid sample heating arising from high powered heteronuclear decoupling pulses. Since the pulse's effect on a specific spin comes primarily from frequency components that are on resonance (or nearly on resonance), components at frequencies that correspond to unpopulated regions were selectively deleted from the pulse. Dual-band decoupling pulses were achieved with around 87% of the power of the original broadband pulse.

The idea of selectively editing a pulse in the frequency domain also arises very naturally in the context of the multi-frame method. For Kupce and Freeman (1994), the initial broadband pulses were sequences of phase-alternating rectangular pulses. The frequency domain description of these pulses comprises sets of sinc functions. However, the small set of sinusoidal modulations that constitute a multi-frame pulse makes the process of frequency-domain editing much more straight-forward, since the frequency domain representation is a set of spaced-out Dirac delta functions, and each frequency component performs a specific, independent role. The pulse amplitude u_{k} corresponds to 2^{k} frequency components, since (from (2.4)) the pulse $v_0(t)$ contains the component

$$v_0(t) = ... + 2^{\mathrm{k}} u_{\mathrm{k}} \sin(f_{\mathrm{k}} t) \cos(f_{\mathrm{k-1}} t) ... \cos(f_1 t) + ...$$

These 2^{k} frequencies are arranged symmetrically on either side of the carrier frequency of the pulse, and each has amplitude $\pm u_{\mathrm{k}}$. Therefore, deleting (or scaling down) the pulse amplitudes u_{k} allows access to a rich space of *symmetric* spin-locking profiles. This is achieved by creation of a *dual*-band pulse in frame k.

However, if only *some* of the 2^{k} frequency components with amplitude u_{k} are removed, and the rest are not altered, then the dual-band structure in frame k will be created only in

some spectral regions. For example, consider the term proportional to u_1:

$$\begin{aligned} H_{\mathrm{RF}}(t) &= ... + 2u_1 \sin(f_1 t) I_{\mathrm{y}} + ... \\ &= ... + u_1(\cos(f_1 t) I_{\mathrm{x}} + \sin(f_1 t) I_{\mathrm{y}}) - u_1(\cos(-f_1 t) I_{\mathrm{x}} \sin(-f_1 t) I_{\mathrm{y}}) + ... \end{aligned}$$

These two waves are oscillating at rates that differ by $2f_1$, which is in general considerably larger that the amplitude u_1. Therefore, the rotating wave approximation can be invoked in the following way: for spins with resonance frequency near f_1, the pulse component with frequency $-f_1$ is far off-resonance and therefore can be ignored. Conversely, for spins near $-f_1$, the pulse component at f_1 can be ignored. The analysis of the chemical shift reduction and effective band structure can proceed *independently* for the two groups of spins. To induce a dual band structure around $+f_1$, the amplitude of the $+f_1$ frequency component is reduced. To maintain a single band around $-f_1$, the amplitude of the $-f_1$ frequency component is not altered from its value given by (2.10) and (2.11).

Figure 2.7 shows the design process for a pulse capable of simultaneously spin-locking the aliphatic carbons and carbonyl, without expending power on any other spectral regions. The process begins with the design of a broadband pulse using (2.10) and (2.11). Next, the the pulse amplitudes u_0 and u_1 are set to zero. These two amplitudes correspond to three frequency components, so the pulse now has four distinct bands, as can be seen in Figure 2.7D. Two of these bands can be joined together by reinstating the full amplitude u_1 at frequency $+f_1$ (but *not* at frequency $-f_1$). Another band can be deleted altogether, since it is far away from the spectral regions of interest. To achieve all of this, the following frequency components are *removed* from the original broadband pulse:

- To create a dual band structure, delete frequency components

  $f = 0$ (carrier frequency, i.e. set $u_0 = 0$)

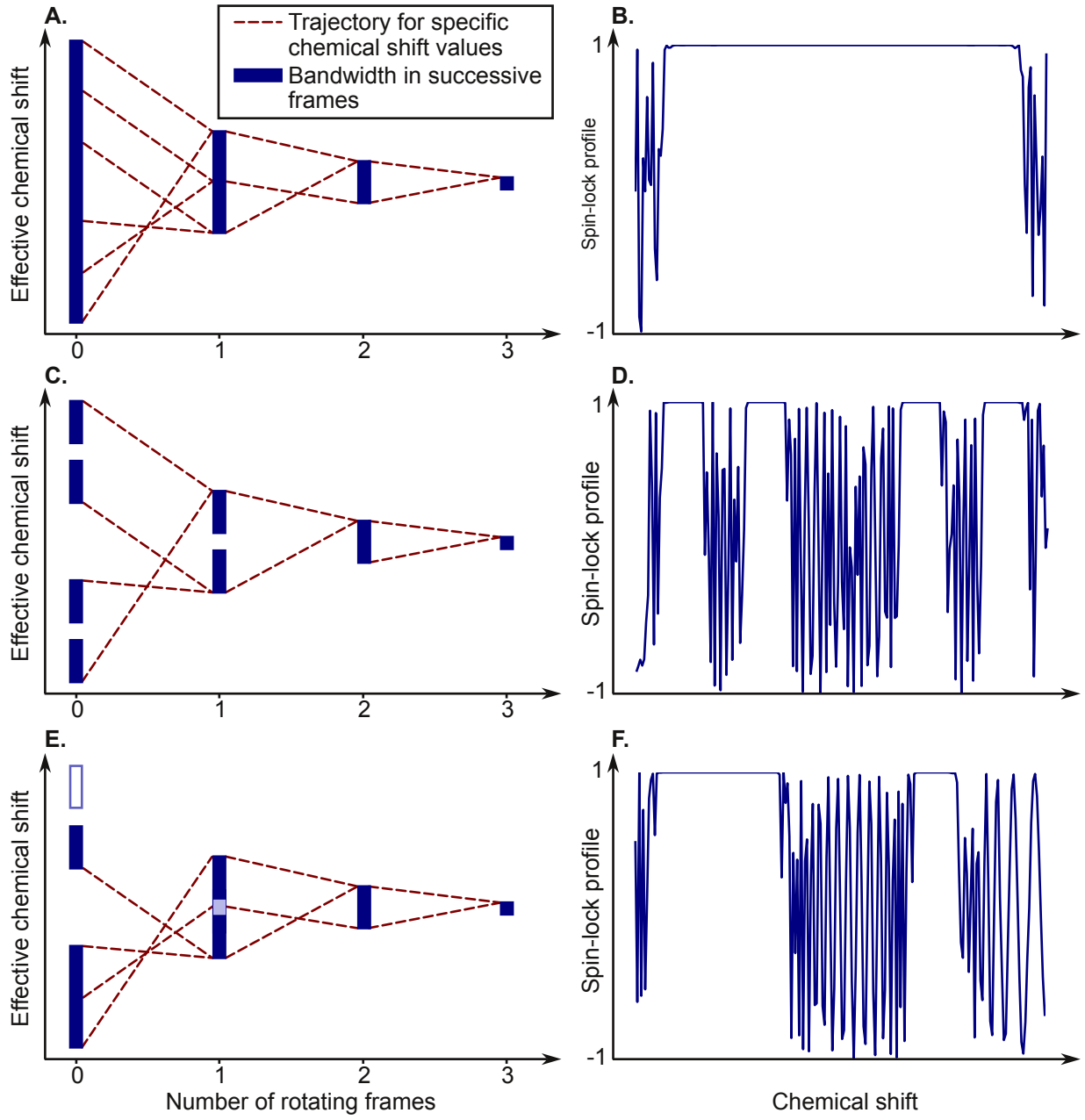

Figure 2.7: The design of a dual-band pulse with asymmetric bands. **A.** The design begins with a broadband pulse, designed by repeated application of (2.10) and (2.11). The pulse parameters are given in Table 2.4. This schematic tracks the values of effective chemical shift through several frames. **B.** The broadband pulse is simulated from initial state $\rho(0) = I_{\mathrm{y}}$, and the final y-component of magnetization is plotted for a range of chemical shifts. **C., D.** The first two pulse amplitudes are set to zero, bringing about a dual-band structure in each of the first two frames, i.e. four bands altogether. **E., F.** The Fourier components that were deleted are selectively reinstated, joining two of the bands into a single larger band. Also, the Fourier components corresponding to one of the other bands are deleted altogether. The final bands are of different widths.

	$k=0$	1	2	3	4	5
u_k/v_5	5.2160	2.5140	1.3471	0.6492	0.3571	$v_5 = 0.0859$
f_k	-	10.8201	4.3280	1.8033	0.7213	0.3607
Tf_k	-	30	12	5	2	1

Table 2.4: Pulse amplitudes and frequencies (in kHz) for the dual-band pulses simulated in Figure 2.7. The parameters are given for the broadband version (Subfigure 2.7B); the final pulse (Subfigure 2.7F) is created by removing various frequency components as described in the text. The pulse time is $T = 2.773$ ms. The RF power is 4 kHz.

- To further split the down-field (carbonyl) band in two, delete the component at

  $$f = f_1 + f_2$$

- To remove the furtherest down-field band completely, eliminate components at frequencies

  $$f = f_1 + f_2 \pm f_3$$

  $$f = f_1 + f_2 \pm f_3 \pm f_4$$

  $$f = f_1 + f_2 \pm f_3 \pm f_4 \pm f_5$$

The end result is a wide band, a gap, and a narrow band. The relative widths of these three features are approximately 1:1:0.25—perfect for the spacing of the aliphatic and carbonyl regions. The pulse parameters for the initial broadband pulse are given in Table 2.4, and the final spin-locking profile is displayed in Figure 2.7F.

2.5 Summary

So far, an algorithm has been developed to effectively spin-lock an ensemble of spins-1/2 to the y-axis of the Bloch sphere. *Effective* spin-locking means that the spins return to the y-axis at times 0, T, 2T, and so on. The proposed method has desirable properties compared to other spin-locking methods. For example, the ratio of bandwidth to applied

RF power is large, and the spin-locking performance is robust to experimentally reasonable RF inhomogeneities. Moreover, it is straightforward to create pulses that are selective for multiple frequency bands to match the band structures of particular applications.

However, for TOCSY pulses this is only half the story. The Hartmann-Hahn condition requires that the effective coupling constants are large compared to the effective bandwidth. Reducing the effective bandwidth by spin-locking will only produce cross polarization if the couplings are largely maintained. In Chapter 4, the multi-frame method is applied to isotropically coupled spins-1/2. Specifically, the coupling Hamiltonian is iteratively transformed through the various tilted, rotating frames, so that its effective magnitude can be calculated in the spin-locking frame. However, before moving on to coupled spin systems, Chapter 3 addresses the validity of the rotating wave approximations that were made during the derivation of the multi-frame method.

3

The effect of off-resonance terms

The derivation of the multi-frame design method relied on the rotating wave approximation to generate the k^{th} frame Hamiltonian, given by (2.3). Under this approximation, rapidly oscillating terms in the Hamiltonian are removed, and more slowly time-varying terms are assumed to account for the dynamics.

Rapidly oscillating terms average to zero over relatively short timescales, and so their overall effect is smaller than the slower terms. However, these terms can have a non-negligible impact on the dynamics. This can be captured by a time-invariant correction to the average Hamiltonian in the manner of perturbation theory, for example the Bloch-Siegert shift (Bloch

and Siegert 1940). For the familiar transform from the laboratory frame to the frame rotating at the Larmor frequency of a particular NMR-active isotope, the correction is negligible and is safely ignored. However, for the kHz-frequency terms that were generated by subsequent rotating frames in Chapter 2, the Bloch-Siegert corrections are not negligibly small.

Off-resonance effects can be analyzed using the first few terms of a series expansion of the solution to the Schrödinger equation which is valid at the end of the pulse. For example, average Hamiltonian theory (Haeberlen 1976; Llor 1992), the Magnus expansion (Magnus 1954; Klarsfeld and Oteo 1989), and the Floquet expansion (Floquet 1883; Leskes et al. 2010) all work in this way. However, these tools are not directly applicable to the iterative scheme discussed in Chapter 2, since the goal is to suppress rapidly time-varying terms, but *keep* other time-varying terms. For example, in each frame $v_{\mathrm{k}}(t)$ must be time-varying, but it is desirable to account for the extra terms that oscillate at frequency $2f_{\mathrm{k}}$.

Another strategy that is widely used in NMR (Cavanagh et al. 2007) is to find a frame-transformation of the Hamiltonian which renders it time-invariant. This can often be achieved using a frame of reference that is either rotating or contains another simple modulation. In this chapter, *specific* time-varying terms are removed using a toggling frame transformation in which the undesired modulations are replaced by time-invariant corrections, but the desired time-variation of $v_{\mathrm{k}}(t)$ is preserved.

The result is that the first-order perturbation corrections for the rapidly oscillating terms just add additional effective chemical shift offsets in each new frame. In other words, the undesired time-varying terms are swapped for a change in the effective chemical shift. Since the multi-frame method is robust to large bandwidths of chemical shift in successive frames, the corrections do not invalidate (2.1). As for the case of RF inhomogeneity (Section 2.2), the relevant correction reduces the precision of (2.2), but does not threaten the overall architecture of the multi-frame pulse design method.

3.1 The Bloch-Siegert shift

In this section, the lowest order correction for an off-resonance perturbation to the spin-1/2 Hamiltonian, which is known as the Bloch-Siegert shift, is reviewed. Consider an arbitrary shaped RF pulse ($A(t),\ \phi(t)$) applied off-resonance, i.e.

$$H(t) = \omega I_{\mathrm{z}} + A(t)\left(\cos(\omega_{\mathrm{RF}} t + \phi(t))I_{\mathrm{x}} + \sin(\omega_{\mathrm{RF}} t + \phi(t))I_{\mathrm{y}}\right)$$

where off-resonance means that ω_{RF}—the offset of the RF pulse carrier frequency—is large compared to the other parameters. The first term of the Magnus expansion is the time-average of the Hamiltonian over one period T, i.e. $\overline{H} = \omega I_{\mathrm{z}}$. This corresponds to neglecting the off-resonance pulse in accordance with the rotating wave approximation. The lowest order correction is given by the second Magnus term,

$$\begin{aligned}
\overline{H^{(2)}} &= \frac{1}{2T}\int_0^T [H(t), \int_0^t H(\tau)d\tau]dt = -\frac{\langle A(t)^2\rangle}{2\omega_{\mathrm{RF}}} I_{\mathrm{z}} \\
H^{\mathrm{eff}} &= \overline{H} + \overline{H^{(2)}} + O\left(\frac{1}{\omega_{\mathrm{RF}}^2}\right)
\end{aligned}$$

where angled brackets denote a time-average. This means that the apparent Larmor frequency (z-component) is shifted by the presence of the off-resonance pulse. The precise form of the pulse shape is unimportant in determining the shift; only the mean-square pulse amplitude and resonance offset are used to calculate $\overline{H^{(2)}}$. This correction has been established and confirmed using various analytical methods (Bloch and Siegert 1940; Ramsey 1955; Leskes et al. 2010), observed experimentally for a range of different pulse shapes (Emsley and Bodenhausen 1990; McCoy and Mueller 1992), and even used as the basis for novel magnetic resonance imaging techniques (Sacolick et al. 2010; Turk et al. 2014).

In the repeated rotating frame pulse design method, non-resonant terms are removed in

each new rotating frame. Specifically, the Hamiltonian decomposes into two parts

$$H^{(\mathrm{k})}(t) = \omega_{\mathrm{k}} I_{\mathrm{z}} + u_{\mathrm{k}} I_{\mathrm{x}} + v_{\mathrm{k}}(t) I_{\mathrm{y}}$$
$$H^{(\mathrm{k'})}(t) = \exp(i2f_{\mathrm{k}} I_{\mathrm{z}})\,(-u_{\mathrm{k}} I_{\mathrm{x}} + v_{\mathrm{k}}(t) I_{\mathrm{y}})\exp(-i2f_{\mathrm{k}} I_{\mathrm{z}})$$

That is, the error Hamiltonian $H^{(\mathrm{k'})}(t)$ contains a pulse with magnitude $\sqrt{u_{\mathrm{k}}^2 + v_{\mathrm{k}}^2(t)}$, off-resonance by $2f_{\mathrm{k}}$. The relevant Bloch-Siegert shift to the z-component of $H^{(\mathrm{k})}(t)$ is

$$\Delta\omega = -\frac{\langle u_{\mathrm{k}}^2 + v_{\mathrm{k}}(t)^2 \rangle}{4f_{\mathrm{k}}}$$

The problem is to understand why the multi-frame method, which does not account for this sizable correction, produces reliable spin-locking pulses which function correctly in simulations and experiments. Moreover, adjusting the design algorithm to account for the Bloch-Siegert shift in general produces spin-locking pulses of much poorer quality than those created using the standard algorithm, (2.10) and (2.11).

Note that the derivations of the Bloch-Siegert shift consider a Hamiltonian that has exactly two parts: a Zeeman term (i.e. a chemical shift frequency that encodes precession about the z-axis), and an off-resonance RF pulse. In particular, there are no on-resonance terms except for the chemical shift itself. However, when off-resonance waves are encountered in the multi-frame method, there are also on-resonance transverse fields $u_{\mathrm{k}} I_{\mathrm{x}}$ and $v_{\mathrm{k}}(t) I_{\mathrm{y}}$. In the next section, the lowest order correction for an off-resonance perturbation is addressed in the presence of an *on*-resonance pulse.

3.2 Interactions betweens oscillating and static fields

In this section, rapid oscillations are exchanged for time-invariant corrections in the case of a simple Hamiltonian containing both on- and off-resonance RF fields. Particular attention

is paid to the *phase* of the off-resonance wave. Consider the following Hamiltonian, which is expressed in an appropriately chosen rotating near-resonance frame such that $\omega \approx 0$,

$$H(t) = \omega I_{\mathrm{z}} + u I_{\mathrm{x}} + v I_{\mathrm{y}} + \alpha(\cos(ft + \phi) I_{\mathrm{x}} + \sin(ft + \phi) I_{\mathrm{y}}) \tag{3.1}$$

where u, v. and ω are time-invariant fields, and the Hamiltonian is perturbed by an oscillating field of magnitude α, frequency f, and arbitrary phase ϕ in the transverse plane. Of particular interest is the case where the oscillation is rapid, in the sense that f is significantly larger than the other parameters. In this case, the oscillations average out rapidly and might plausibly be neglected under the rotating wave approximation, or else accounted for by a small correction. That is, the unitary solution to the the Schrödinger equation for (3.1) at time T is

$$V(T) = \exp(-iT((\omega + \Delta_{\mathrm{z}}) I_{\mathrm{z}} + (u + \Delta_{\mathrm{x}}) I_{\mathrm{x}} + (v + \Delta_{\mathrm{y}}) I_{\mathrm{y}})$$

where the Δ_{x}, Δ_{y}, and Δ_{z} are corrections that account for the off-resonance wave, and the solution is valid at times that are multiples of $2\pi/f$. The approach is to find a frame of reference in which $H(t)$ becomes time-invariant. Consider the two unitary frame changes

$$\begin{aligned} U_1(t) &= \exp(iP(t) I_{\mathrm{x}}), \quad P = \frac{\alpha}{f}(\sin(ft + \phi) - \sin(\phi)) \\ U_2(t) &= \exp(iQ(t) I_{\mathrm{y}}), \quad Q = \frac{\alpha}{f}(\cos(\phi) - \cos(ft + \phi)) \end{aligned}$$

Notice that at times that are integer multiples of $2\pi/f$, both unitaries are equal to the identity. Therefore, changing the frame of the Hamiltonian by either of these does not effect the density matrix or the unitary propagator at these times. $P(t)$ and $Q(t)$ are chosen in this way because their time-derivatives match the oscillating fields, which will lead to cancellation

of the undesired terms. The Hamiltonian can be expressed in the frame of $U_1(t)$ using (A.2):

$$\begin{aligned} H &\rightarrow U_1 H U_1^\dagger - \alpha\cos(ft+\phi)I_\mathrm{x} \\ &= \omega(\cos(P)I_\mathrm{z} + \sin(P)I_\mathrm{y}) + uI_\mathrm{x} + (v + \alpha\sin(ft+\phi))(\cos(P)I_\mathrm{y} - \sin(P)I_\mathrm{z}) \\ &= (\omega - vP - \alpha\sin(ft+\phi)P)I_\mathrm{z} + uI_\mathrm{x} + (v + \alpha\sin(ft+\phi) + \omega P)I_\mathrm{y} + O(\frac{1}{f^2}) \end{aligned}$$

Terms higher than first-order in $1/f$ have been neglected, since f is much larger than the other parameters. Next, the Hamiltonian is expressed in the frame of $U_2(t)$ in the same way:

$$\begin{aligned} H &\rightarrow U_2 H U_2^\dagger - \alpha\sin(ft+\phi)I_\mathrm{y} \\ &= (\omega - vP - \alpha\sin(ft+\phi)P + uQ)I_\mathrm{z} + (u - \omega Q)I_\mathrm{x} + (v + \omega P)I_\mathrm{y} + O(\frac{1}{f^2}) \end{aligned}$$

once again, terms higher than first-order in $1/f$ have been removed. Therefore, the time-averaged Hamiltonian in the toggling frame of $U_2(t)U_1(t)$, including corrections up to first-order in $1/f$, is

$$\overline{H} = (\omega - \frac{\alpha^2}{2f} + \frac{\alpha}{f}(u\cos(\phi) + v\sin(\phi)))I_\mathrm{z} + (u - \omega\frac{\alpha}{f}\cos(\phi))I_\mathrm{x} + (v - \omega\frac{\alpha}{f}\sin(\phi))I_\mathrm{y} \quad (3.2)$$

The correction to the chemical shift frequency proportional to α^2 is the Bloch-Siegert shift, which arises from interactions between the x and y components of the oscillating field. The other correction in the z-direction is due to the interaction between the transverse static fields and the off-resonance oscillations. Crucially, the *phase* of the oscillating field, relative to the transverse field, determines the shift in the apparent Larmor frequency. There is also a phase dependent first-order correction in the $x-y$ plane. Note that in the case where the on-resonance pulse is absent ($u = v = 0$), the Bloch-Siegert shift is the only correction to the Hamiltonian.

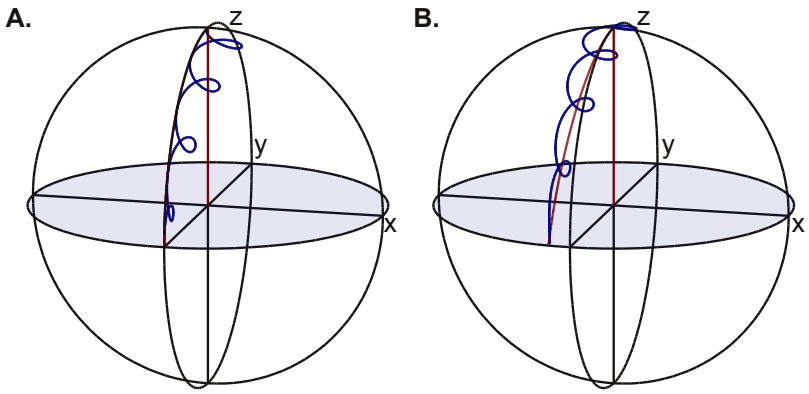

Figure 3.1: Numerical integration of Hamiltonians from Example 3.1. **A.** The Hamiltonian $H_1(t)$ excites $\rho(0) = I_z$ to very near $\rho(T) = -I_y$. This behavior is captured by the average Hamiltonian $\overline{H}_1 = 0.5I_x$. **B.** The Hamiltonian $H_2(t)$ also has rapidly oscillating terms, however these have a different phase from $H_1(t)$. This leads to a slightly different final state. The net evolution of $\rho(0) = I_z$ is described by $\overline{H}_2$, which includes a small time-invariant correction in the z-direction. The evolutions of both $H_2(t)$ and $\overline{H}_2$ are depicted, demonstrating the high level of accuracy with which $\overline{H}_2$ matches $H_2(t)$ at the initial and final times, and the difference between the final state under the two different phases of the rapidly-oscillating terms.

Example 3.1 *To illustrate how the first-order correction changes with the phase of the rapidly-oscillating field, the following two Hamiltonians were simulated:*

$$H_1(t) = (0.5 + \cos(8t))I_x + \sin(8t)I_y$$

$$H_2(t) = (0.5 + \cos(8t + \pi/2))I_x + \sin(8t + \pi/2)I_y$$

for time $t \in [0,\ \pi]$. *The only difference is the phase of the oscillating part relative to the static part, which is* $\phi = 0$ *for* H_1 *and* $\phi = \pi/2$ *for* H_2. *Clearly, to zeroth-order (i.e. under the rotating wave approximation) both Hamiltonians produce a rotation about the* x *axis with flip-angle* $\frac{\pi}{2}$. *However, the average Hamiltonians after first-order corrections differ. Using*

(3.2), *the corrected average Hamiltonians are*

$$\overline{H}_1 = 0.5I_x$$

$$\overline{H}_2 = 0.5I_x - 0.0625I_z$$

where the I_z correction to H_2 is the Bloch-Siegert shift. The shift does not appear for H_1, since it is canceled under (3.2). *Figure 3.1 shows the evolution of $\rho(0) = I_z$ for the two time-varying Hamiltonians, found by numerical integration. It is clear that the Bloch-Siegert shift applies to $H_2(t)$. However, for $H_1(t)$ the rapidly oscillating parts can be dropped without applying a correction, since the total first-order correction to the chemical shift frequency is zero.*

It is clear that when first-order corrections for the rotating wave approximation are constructed, the correction depends not only the amplitude and frequency of the suppressed oscillation, but also on its phase. Of particular interest is the correction to the transverse components in (3.2). Specifically, off-resonance terms with phase 0, π lead to *no* first-order correction to the y-component of the Hamiltonian. This observation will turn out to be crucial for understanding the effect of the rotating wave approximations that were made in Chapter 2.

The following additional example adds a second off-resonance wave to $H_2(t)$ from the previous example. This complicates the magnetization trajectory; the system exhibits jagged and highly epicyclical behavior. However the required correction arising from the removal of the second wave exactly negates the correction from removing the first wave. Note that this is not achieved by having the two waves off-resonance in opposite directions. That is, the oscillating terms are not divided between *above* and *below* resonance, to give opposite Bloch-Siegert shifts, viz. $\frac{-\alpha_1^2}{2f_1} + \frac{-\alpha_2^2}{2f_2} = 0$. Rather, the waves are both above resonance, and the cancellation of corrections arises specifically from the two waves' differing ϕ-dependent

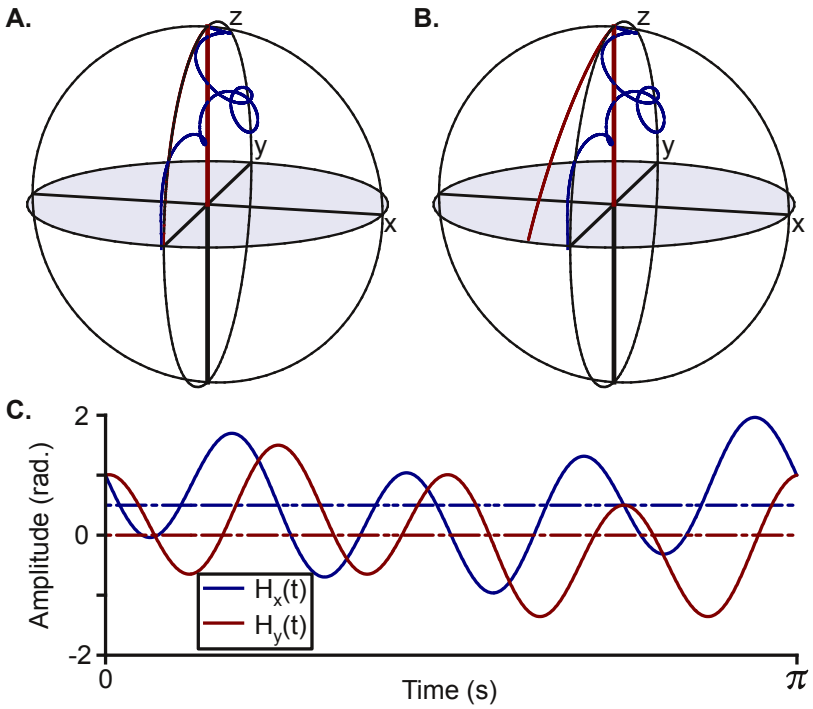

Figure 3.2: Numerical integration of the Hamiltonian $H_3(t)$ from Example 3.2. **A.** The Hamiltonian $H_3(t)$ excites $\rho(0) = I_z$ to very near $\rho(T) = -I_y$, despite the presence of two relatively high amplitude, off-resonance waves. This behavior is captured by the average Hamiltonian $\overline{H}_3$, from which the off-resonance terms have been removed without applying any net correction. **B.** The Hamiltonian $\overline{H}_3'$, which includes a Bloch-Siegert correction for each off-resonance wave that was removed, does not faithfully predict the final state. **C.** The x and y components of $H_3(t)$ (solid lines) contain high amplitude oscillations about their respective means (dot-dashed lines). According to (3.2) these oscillations can be removed without applying a correction.

interaction with the transverse field uI_x.

Example 3.2 *First-order correction for multiple off-resonance fields. The Hamiltonian $H_2(t)$ from Example 3.1 is perturbed by second above-resonance field. The additional corrections from a second application of* (3.2) *lead to cancellation, and the net first-order correction*

is zero.

$$\begin{aligned} H_3(t) &= H_2(t) + 0.5\cos(2t))I_x + 0.5\sin(2t)I_y \\ &= (0.5 + \cos(8t + \pi/2) + 0.5\cos(2t))I_x + (\sin(8t + \pi/2) + 0.5\sin(2t))I_y \end{aligned}$$

The time axis is $t \in [0,\ \pi]$*. The average Hamiltonians after first-order corrections is*

$$\overline{H}_3 = 0.5I_x$$

Subfigure 3.2A shows the effect of $H_3(t)$ *and* $\overline{H}_3$ *on an initial state* $\rho(0) = I_z$*. Clearly, the average Hamiltonian captures the net evolution of the system with high accuracy; the two magnetization trajectories both end up close to* $\rho(T) = -I_y$*. This should be contrasted with the (incorrect) average Hamiltonian* $\overline{H}'_3$*, which includes only the Bloch-Siegert shift associated with each wave,*

$$\begin{aligned} \overline{H}'_3 &= 0.5I_x + \frac{-1}{16}I_z + \frac{-0.5^2}{4}I_z \\ &= 0.5I_x - 0.1250I_z \end{aligned}$$

Subfigure 3.2B shows that the trajectory of $\overline{H}'_3$ *does not match the dynamics of the complete Hamiltonian* $H_2(t)$*. Note that if the oscillating terms with frequency* 2 *are phase shifted by* $\pm\pi/2$*, then the first-order corrections no longer cancel out, and* $\overline{H}'_3$ *is the correct average Hamiltonian.*

The important insight is that corrections due to a set of removed waves do not necessarily accumulate as a sum of Bloch-Siegert shifts. Rather, each wave's phase must be taken into account, as must the on-resonance transverse fields uI_{x} and vI_{y}. Depending on the distribution of phases, amplitudes, and frequencies of the waves being removed, as well as

on the parts of the Hamiltonian that are being kept, the rotating wave approximation could necessitate drastic corrections, minor corrections, or, in certain contrived circumstances, no corrections at all.

3.2.1 Nutating frame spectroscopy with first-order correction

In this subsection, the multi-frame algorithm is applied for the case of $n = 1$, i.e. a single rotating frame. This has been called *nutating frame spectroscopy* (Grzesiek and Bax 1995). However, (3.2) is used to more accurately predict the effective chemical shift in the nutating frame, as compared with (2.2). Finally, this more accurate effective Hamiltonian is used to improve the nutating frame pulse.

For a single rotating frame, the multi-frame pulse reduces to

$$H_{\mathrm{RF}} = u_0 I_{\mathrm{x}} + 2\cos(f_1 t) v_1 I_{\mathrm{y}} \tag{3.3}$$

so that the Hamiltonian for an isolated spin, expressed in frame 1, is

$$\begin{aligned} H^{(1)} &= (\sqrt{\omega_0^2 + u_0^2} - f_1) I_{\mathrm{z}} + v_1 I_{\mathrm{y}} + v_1(\cos(2f_1 t) I_{\mathrm{y}} + \sin(2f_1 t) I_{\mathrm{x}}) \\ &= (\sqrt{\omega_0^2 + u_0^2} - f_1) I_{\mathrm{z}} + v_1 I_{\mathrm{y}} - v_1(\cos(-2f_1 t - \frac{\pi}{2}) I_{\mathrm{x}} + \sin(-2f_1 t - \frac{\pi}{2}) I_{\mathrm{y}}) \end{aligned}$$

The oscillating terms have been expressed in this way to match (3.1). Using (3.2), this averages to

$$\overline{H} = (\sqrt{\omega_0^2 + u_0^2} - f_1 - \frac{v_1^2}{4f_1}) I_{\mathrm{z}} + (v_1 + \frac{v_1}{2f_1}(\sqrt{\omega_0^2 + u_0^2} - f_1)) I_{\mathrm{y}}$$

The terms with f_1 in the denominator are due to the first-order corrections, which were neglected in Chapter 2. There is now dispersion in the y-component, due to the presence of ω_0, and an offset in the effective chemical shift of $-\frac{v_1^2}{4f_1}$.

Suppose that the pulse time is $T = 2\pi$, and $f_1 = 1$ for frame alignment. Furthermore, choose $v_1 = 0.25$ so that the flip angle is $\frac{\pi}{2}$ radians about the y-axis. The maximum allowable offset in frame 1 is set to $C_1 = 0.025$, or 10% of the magnitude of the spin-locking field v_1. Then (2.10) and (2.11) give an x-component of $u_0 = 0.975$ and a working bandwidth in frame 0 or $2C_0 = 0.6325$. With these parameters, the first-order correction to the z-component is $-\frac{1}{64}$.

In Subfigure 3.3A the effective Hamiltonian for (3.3) is calculated numerically for a range of chemical shifts, using the matrix-logarithm of the numerically-integrated unitary propagator. The z-component is compared to the prediction given by (2.2) and (3.2). The latter, which includes first-order corrections, is more accurate.

It is clear at this point that the design parameters should be modified to account for the first-order correction to the effective chemical shift. As in Subsection 2.1.4, the first step is to find the range of chemical shifts in the first rotating frame, and use f_1 to center the bandwidth. This approach is repeated here, with the first order corrections included:

$$\begin{aligned}
\min(\omega_1) &= u_0 - f_1 - \frac{v_1^2}{4f_1} \\
\max(\omega_1) &= \sqrt{C_0^2 + u_0^2} - f_1 - \frac{v_1^2}{4f_1} \\
\therefore 2f_1 &= \sqrt{C_0^2 + u_0^2} + u_0 - \frac{v_1^2}{2f_1} \\
\therefore 2C_1 &= \sqrt{C_0^2 + u_0^2} - u_0
\end{aligned}$$

This can be rearranged so that u_0 and C_0 can be calculated from the frame 1 parameters:

$$u_0 = f_1 - C_1 + \frac{v_1^2}{4f_1} \tag{3.4}$$

$$C_0 = 2\sqrt{f_1 C_1 + C_1 \frac{v_1^2}{4f_1}} \tag{3.5}$$

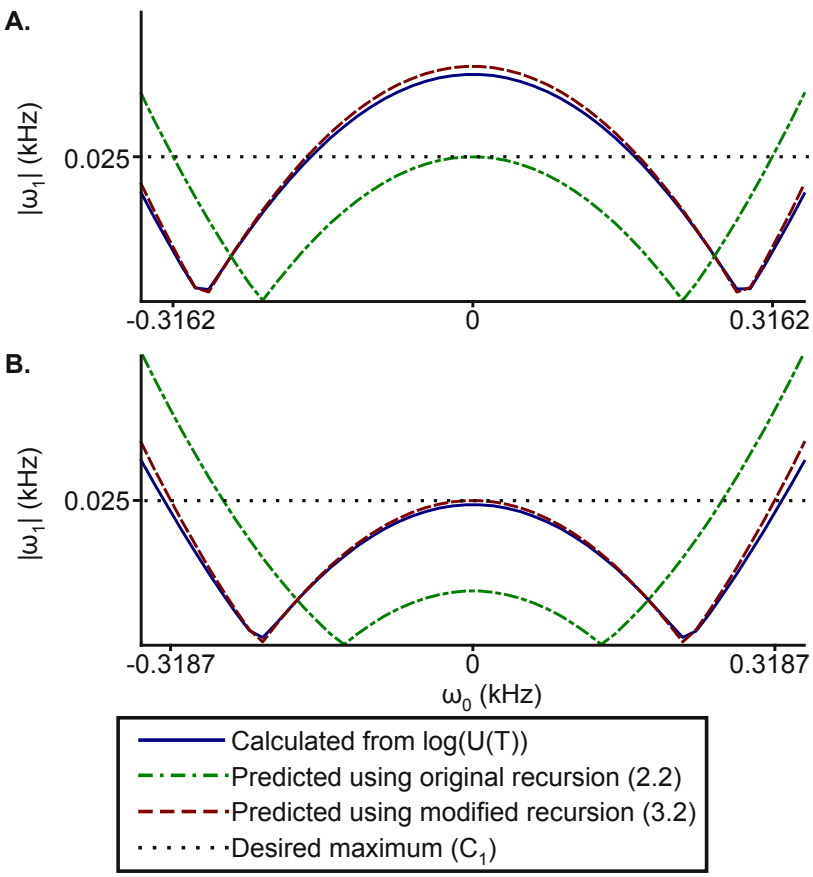

Figure 3.3: The magnitude of the effective chemical shift in the nutating frame. **A.** The pulse (3.3) was simulated for a range of offsets, and the matrix logarithm of the unitary propagator at time T was used to calculate the effective offset frequency (solid line). This is compared to the prediction of offset frequency found using (2.2) (dot-dash line) which was designed to keep the offset less than $C_1 = 0.025$ kHz (dotted line). Clearly, the numerically calculated offset exceeds this limit inside the bandwidth. The offset frequency is more accurately tracked by (3.2) (dashed line). **B.** When the design recursions (3.4) and (3.5) are used, the numerically calculated offset frequency obeys the design limit.

Table 3.1 shows the pulse parameters, derived using the original design algorithm, (2.10) and (2.11), and the modified algorithm, (3.4) and (3.5). The parameter u_0 and the active bandwidth C_0 are adjusted marginally. Figure 3.3B shows that the modified design algorithm (3.4) and (3.5) succeeds in keeping the effective offset below the chosen limit C_1.

	T	v_1	C_1	f_1	u_0	C_0
Original method	2π	0.25	0.025	1	0.975	0.3162
Modified method	2π	0.25	0.025	1	0.9906	0.3187

Table 3.1: Comparison of the pulse parameters generated by (2.10) and (2.11) versus the modified version, (3.4) and (3.5), for the case of one rotating frame. The modified recursion assigns slightly more amplitude to the static x-axis field (u_0).

3.3 Error toggling frame

The revised design recursion (3.4) and (3.5) can be applied in the case of a single nutating frame. However, the multi-frame method developed in Chapter 2 requires one rotating wave approximation each time a new rotating frame of reference is constructed. Moreover, $v_{\mathrm{k}}(t)$ in general contains a range of frequency components, which means that the off-resonance terms proportional to $v_{\mathrm{k}}(t)$ is in fact the superposition of a range of off-resonance terms. A further complication is that the time-varying terms cannot all be averaged away using average Hamiltonian theory; the frame k + 1 RF pulse must be time-varying in order to bring about the iterative design method.

The problem is of the following form: to account for rapidly-oscillating terms $A(t)I_{\mathrm{x}}$ and $B(t)I_{\mathrm{y}}$, where

$$H(t) = H_0(t) + A(t)I_{\mathrm{x}} + B(t)I_{\mathrm{y}}$$

$$H_0(t) = \omega I_{\mathrm{z}} + uI_{\mathrm{x}} + v(t)I_{\mathrm{y}}$$

$$A(t) = -u\cos(2ft) + v(t)\sin(2ft), \quad B(t) = v(t)\cos(2ft) + u\sin(2ft)$$

Reference to the frame number k has been removed, since the same problem is faced in each frame. The strategy is to construct a toggling frame in which $A(t)$ and $B(t)$ are largely

converted to time-invariant corrections. Define $P(t)$ and $Q(t)$ by

$$\begin{aligned} P(t) &= -\frac{u}{2f}\sin(2ft) + \frac{v}{2f}(1-\cos(2ft)) \\ \dot{P} &= A(t) + \frac{\dot{v}}{2f}(1-\cos(2ft)) \\ Q(t) &= \frac{v}{2f}\sin(2ft) + \frac{u}{2f}(1-\cos(2ft)) \\ \dot{Q} &= B(t) + \frac{\dot{v}}{2f}\sin(2ft) \end{aligned}$$

Clearly $P(T) = P(0) = 0$ and $Q(T) = Q(0) = 0$, so that the toggling frames will fall into alignment at the end of the pulse; a change of frames given by $U(t) = \exp(iQ(t)I_{\mathrm{y}})\exp(iP(t)I_{\mathrm{x}})$ will align with the original frame at stroboscopic times. Beginning with the toggling frame $\exp(iP(t)I_{\mathrm{x}})$:

$$\begin{aligned} H(t) &\to \exp(iP(t)I_{\mathrm{x}})H(t)\exp(-ip(t)I_{\mathrm{x}}) - \dot{P}(t) \\ &= (\omega\cos(P) - (v+B)\sin(P))\,I_{\mathrm{z}} + \left(u - \frac{\dot{v}}{2f}(1-\cos(2ft))\right)I_{\mathrm{x}} \\ &\quad + (v\cos(P) + \omega\sin(P) + B\cos(P))\,I_{\mathrm{y}} \end{aligned}$$

Next, the Hamiltonian is expressed in the toggling frame $\exp(iQ(t)I_{\mathrm{y}})$, as

$$\begin{aligned} H(t) \to & \\ &\left(\omega\cos(P)\cos(Q) - (v+B)\sin(P)\cos(Q) + u\sin(Q) - \frac{\dot{v}}{2f}(1-\cos(2ft))\sin(Q)\right)I_{\mathrm{z}} \\ &+ \left(-\omega\cos(P)\sin(Q) + (v+B)\sin(P)\sin(Q) + u\cos(Q) - \frac{\dot{v}}{2f}(1-\cos(2ft))\cos(Q)\right)I_{\mathrm{x}} \\ &+ \left(v\cos(P) + \omega\sin(P) + B(\cos(P)-1) - \frac{\dot{v}}{2f}\sin(2ft)\right)I_{\mathrm{y}} \end{aligned}$$

So far no approximations have been made; this Hamiltonian is equivalent to the original Hamiltonian, except that it is expressed in the toggling frame of $U(t)$. The toggling frame

has canceled a large part of the magnitude of the error terms $A(t)$ and $B(t)$, generated time-invariant correction terms, as well as generated additional oscillating fields (which are lower amplitude and oscillate more quickly than $A(t)$ and $B(t)$).

Subfigure 3.4A shows the x, y, and z-components of a Hamiltonian in the presence of a multi-frame pulse. The Hamiltonian is expressed in the first tilted, rotating frame. The x and y components contain high amplitude, rapid oscillations about their approximate values (dashed lines) under the rotating wave approximation. In Subfigure 3.4B only the off-resonance terms are plotted. Subfigure 3.4C shows the same Hamiltonian, expressed in the toggling frame of $U(t)$. The time-averaged x and z components, as well as the desired y-component $v_{\mathrm{k}}(t)$ are plotted too (dashed lines). Clearly, the toggling frame produces a Hamiltonian with fewer unwanted oscillations, and these are displayed in Subfigure 3.4D. They are lower in magnitude, and generally higher in frequency, than the unwanted terms in Subfigure 3.4B. Therefore, in the toggling frame of $U(t)$ the unwanted time-varying terms are smaller than they are in the first tilted, rotating frame. However, the average magnitude of the x-component, and the average magnitude of the z-component (which will form the chemical shift in the next frame, in accordance with the multi-frame method), are changed in the toggling frame. That is, the unwanted oscillations have largely been exchanged for additional chemical shift.

Observe that for a zeroth-order in $\frac{1}{f}$ approximation, $\cos(P) = \cos(Q) = 1$ and $\sin(P) = \sin(Q) = 0$. This gives $H(t) = H_0(t)$, which corresponds to simply ignoring $A(t)$ and $B(t)$. This is the rotating wave approximation that was used in Chapter 2. This can be improved upon by taking account of terms of order $\frac{1}{f}$ and higher.

Corrections to first-order in $\frac{1}{f}$ are found using the small angle approximation, i.e. by

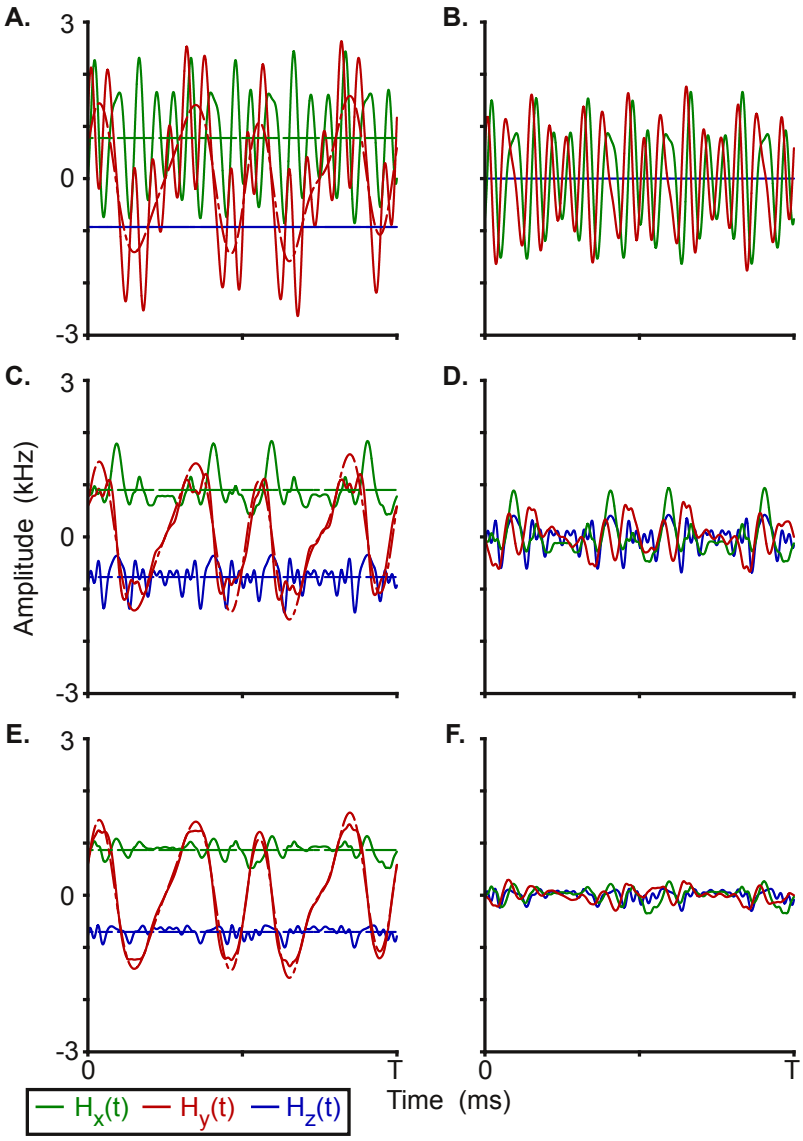

Figure 3.4: The frame 1 Hamiltonian in the presence of a multi-frame pulse is expressed in various toggling frames. The pulse parameters are given in Table 3.2. $\omega_0 = 1$ kHz, and $\omega_1 = -0.93$ kHz. **A.** The first tilted rotating frame. The full Hamiltonian (solid lines) contains large oscillates which are removed by the rotating wave approximation, leaving the desired Hamiltonian (dashed lines). **B.** The terms which have been ignored. **C.** The Hamiltonian is now expressed in the toggling frame of $U(t)$. The average x- and z-components, and the desired y-component $v_{\mathrm{k}}(t)$ are shown (dashed lines). **D.** The residual oscillations in the toggling frame are smaller. **E.** A second toggling frame is constructed numerically to account for the remaining error. In this frame, the full Hamiltonian takes very nearly the form of (2.1). **F.** The remaining oscillations have low amplitude. All three Hamiltonians are equivalent, in the sense that they imply the same unitary propagator at time T.

setting $\cos(P) = \cos(Q) = 1$, $\sin(P) = P$, and $\sin(Q) = Q$,

$$\begin{aligned} H(t) \approx &\left(\omega - (v+B)P - uQ + \frac{\dot{v}}{2f}(1-\cos(2ft))Q\right) I_{\mathrm{z}} \\ &+ \left(-\omega Q + vPQ + u - \frac{\dot{v}}{2f}(1-\cos(2ft))\right) I_{\mathrm{x}} \\ &+ \left(v + \omega P - \frac{\dot{v}}{2f}\sin(2ft)\right) I_{\mathrm{y}} \end{aligned}$$

Time-invariant terms that are order $\frac{1}{f}$ and all terms that are of order 1 will be kept, as was done by Leskes et al. (2010). Observe that $\overline{P(t)} = 0$, and $\dot{v}(t)$ has no component at frequency $2f$, so the time average of the last term in the y direction is zero. Also, $\omega P(t)$ contains only oscillations, and these are proportional to $\frac{1}{f}$. Therefore, the y-component of the corrected Hamiltonian is simply $v(t)$; there is no static correction along the y-axis. Next,

$$\overline{-(v(t)+B(t))P(t) - uQ(t)} = \frac{-\overline{v(t)^2} + 3u^2}{4f}$$

This is reminiscent of the Bloch-Siegert shift, plus a second correction $\overline{uQ(t)} = \frac{u^2}{2f}$ which arises from interactions between the off-resonance and on-resonance terms, as was explored in Section 3.2. Also, $\dot{v}(t)$ shares no frequencies with $(1-\cos(2ft))Q(t)$, so there is no static correction from that term. Finally, the x-component: since $\overline{Q(t)} = \frac{u}{2f}$, there is a static correction of $-\omega\frac{u}{2f}$. The term $v(t)P(t)Q(t)$ has no time-invariant terms of low enough order to include. Therefore, the corrected Hamiltonian is

$$H(t) = \left(\omega + \frac{-\overline{v(t)^2} + 3u^2}{4f}\right) I_{\mathrm{z}} + \left(u - \omega\frac{u}{2f}\right) I_{\mathrm{x}} + v(t) I_{\mathrm{y}} \tag{3.6}$$

The effective chemical shift in this frame is shifted by a correction, which is *not* of the form of a Bloch-Siegert shift. There is also dispersion in the x-component. Crucially, both instances of the dispersive parameter ω, as well as the first-order corrections for the removed terms,

	$k=0$	1	2	3	4
u_k/v_4	0.9845	0.7769	0.5183	0.2881	v_4 =0.0729
f_k	-	2.3342	1.1671	0.5835	0.2918
Tf_k	-	8	4	2	1
C_{k}	3.5500	1.3497	0.3902	0.0652	0.0036

Table 3.2: The amplitudes u_k and frequencies f_k of the modulations in each frame in kHz for the pulse used as an example in Figures 3.4 and 3.5. The pulse time $T = 3.427$ ms and the power is 4 kHz. This list of parameters completely determines the pulse shape via (2.4). The root-mean-square RF power is 3 kHz.

are contained in the $x-z$ plane. The effective shift in the *next* frame is found by combining the I_{z} and I_{x} terms, so that both the appearances ω can be thought of as contributing to the effective chemical shift in the the subsequent frame. The absence of any correction in the y-component ensures that the scheme described in Chapter 2 can be iterated, since further modulations that can generate additional rotating frame constructions are encoded in $v_{\mathrm{k}}(t)$. Specifically, the design method systematically reduced dispersion in the $x-z$ plane, and the first order corrections in each new frame are confined to this plane.

Alternative derivation: There is a different approach to arrive at (3.6) directly from (3.2). It is more difficult to keep track of the order of the terms ignored, but the role of the phase of the error waves is clearer.

The Hamiltonian $H_0(t)$ is perturbed by two off-resonance waves. One with amplitude u, frequency $-2f$, and phase π. The other has (relatively slowly) time-varying amplitude $v(t)$, frequency $-2f$ and phase $\pi/2$. That is, the phase of the two waves differs by $\frac{\pi}{2}$. Applying the corrections from (3.6) yields

$$H(t) = \left(\omega + \frac{-v(t)^2 + 3u^2}{4f}\right) I_{\mathrm{z}} + \left(u - \omega\frac{u}{2f}\right) I_{\mathrm{x}} + \left(v(t) - \omega\frac{v(t)}{2f}\right) I_{\mathrm{y}}$$

Taking the time-average of the corrections gives (3.6).

SECOND TOGGLING FRAME: It is possible to repeat the toggling frame construction, and reduce the remaining undesired oscillations (shown in Subfigure 3.4D) still further. This can most easily be done numerically. The procedure is as follows: choose one of the three axes, and subtract out the part that violates (2.1) using (A.2). For example, the z-term ought to be constant in time, so define

$$R(t) = \int_0^t H_{\mathrm{z}}(\tau) - \overline{H_{\mathrm{z}}(\tau)} d\tau$$

and then express the Hamiltonian is the toggling frame of $U_{\mathrm{R}}(t) = \exp(iR(t)I_{\mathrm{z}})$. This will produce small changes in the x- and y-components of the Hamiltonian, even as it removes the unwanted terms from the z-component. These small changes are inversely proportional to the frequencies of the terms being removed. Similarly, the y-component ought to be $v_{\mathrm{k}}(t)$, so that the unwanted variation around this is removed in the toggling frame given by $U_{\mathrm{S}}(t) = \exp(iS(t)I_{\mathrm{z}})$, where

$$S(t) = \int_0^t H_{\mathrm{y}}(\tau) - v_{\mathrm{k}}(\tau) d\tau$$

This procedure can be iterated, cycling through the three axes. Subfigures 3.4E and 3.4F show a Hamiltonian that has been expressed in a numerically constructed toggling frame, as well as the remaining oscillations. The unwanted time-varying terms in Subfigure 3.4F are significantly smaller than the ones in Subfigure 3.4B. Meanwhile, the toggling frames have slightly changed the time-averaged z- and x- components of the Hamiltonian. The three Hamiltonians plotted in Figure 3.4 are equivalent, in the sense that they all produce identical unitary solutions to the Schrödinger equation at time T, when all toggling frames fall into alignment.

Figure 3.5 shows this calculation for a four-frame pulse with root-mean-square average amplitude of 4 kHz. Subfigure 3.5A is the spin-locking performance of the pulse over time

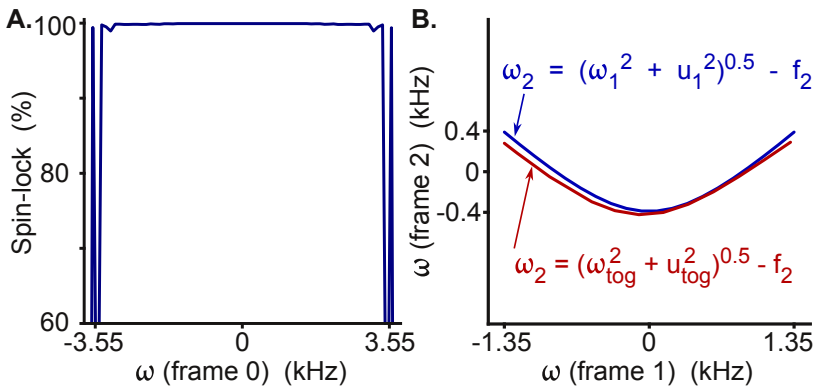

Figure 3.5: Toggling frame Hamiltonian. **A.** Spin-locking performance of a four-frame pulse with $A = 4$ kHz, for duration $4T$. The bandwidth is approximately 7 kHz. **B.** When frame 1 is constructed, there are also off-resonance terms. Ignoring these allows the frame 2 chemical shifts to be calculated using (2.2) (upper trace). Alternatively (lower trace), the z- and x-components are recalculated in a suitable toggling frame (similar to Subfigure 3.4E), and those values are used in (2.2). In either case, the frame 2 bandwidth is successfully reduced to around 0.8 kHz.

$4T$, showing magnetization returned to the y-axis over approximately 7 kHz. In the first tilted, rotating frame, the z- and x-components are $\omega_1 I_z + u_1 I_x$, and there are also terms that are off-resonance by $2f_1$. Subfigure 3.5B shows two ways to calculate the chemical shift in frame 2: In the first calculation (upper trace) rapidly oscillating terms are ignored, and (2.2) is applied. Alternatively (lower trace), the z- and x-components are recalculated in a suitable toggling frame, and those values are used in (2.2). Either way, the frame 2 bandwidth is successfully reduced to around 0.8 kHz.

3.4 Summary

This chapter began with a review of the Bloch-Siegert shift in effective chemical shift frequency due to an off-resonance RF pulse. However, in Section 3.2, corrections that arise from the interaction between on- and off-resonance terms were added to the picture. Simple examples were constructed to demonstrate that lowest-order corrections for the rotating

wave approximation do not necessarily accumulate as a sum of Bloch-Siegert shifts for each off-resonance term that is removed. Rather, depending on the relative phase of on- and off-resonance RF fields, corrections can partially or completely cancel out.

The toggling-frame approach was applied to in the context of the multi-frame pulse, and first-order corrections for the approximations made in Chapter 2 were derived. Additional, numerically constructed toggling frames were used to further suppress the unwanted, rapidly oscillating Hamiltonian terms. Partial cancellation amongst first-order terms in the z-component led to corrections that were smaller than would be obtained by (incorrectly) including only Bloch-Siegert shifts.

Crucially, the corrections generated were confined to the z-x plane, where they manifest as additional chemical shift offsets in subsequent frames. These are then reduced by further applications of (2.2). That is, the necessary corrections to the rotating wave approximations made in Chapter 2 to not invalidate the overall architecture of the repeated rotating frame design method.

4

Broadband homonuclear mixing

To function properly, a homonuclear mixing pulse must produce an average Hamiltonian which has a small effective chemical shift bandwidth (i.e. spin-locking) and comparatively large effective J-couplings. The first part of this—broadband spin-locking—was demonstrated using multi-frame pulses in Chapter 2. This chapter addresses the effective coupling magnitude in the presence of these pulses.

The starting point is the transformation of the J-coupling tensor from the original frame into the multi-rotating spin-lock frame. The effective strength of the coupling—its magnitude when expressed in the n^{th} rotating frame—determines the rate of cross polarization. The

effective coupling strength varies with the offset frequency in each constructed frame. This leads to a simple recursion for the magnitude of the longitudinal (I_zS_z) and transverse ($I_xS_x + I_yS_y$) parts of the coupling, driven by the tilt angles of the n nutating frames. It is demonstrated that the coupling can be largely maintained over a wide spectral region, as compared with existing TOCSY pulse sequences.

In Section 4.2, a set of three example TOCSY pulses are presented. These have high transfer efficiency over a broad range of chemical shift frequencies. It is demonstrated that with three rotating frames, the mixing bandwidth can be larger than the widely-used FLOPSY-16 sequence, which is generally considered to be the best available broadband mixing pulse (Glaser and Quant 1996; Cavanagh et al. 2007; Kovacs and Gossert 2014). With four rotating frames, the bandwidth can be made even higher—about 35% higher than FLOPSY-16. However, further frames cannot be used to increase the mixing bandwidth at will, since the coupling magnitude cannot be maintained over arbitrarily wide spectral widths. This issue is explored in Subsection 4.2.4.

For experimental verification, broadband mixing pulses are applied to a simple pentapeptide sample, described in Figure 4.1, and to larger protein samples. These experimental tests prove that the pulses can be implemented in practice, and demonstrate the higher bandwidth that can be achieved with multi-frame pulses as compared with existing TOCSY sequences.

One particular example pulse, designed using four rotating frames, is explored in detail, via direct comparison with FLOPSY-16 in simulation and experiment. The new pulse, called NF4, compares very favorably to FLOPSY-16. Experimental tests of TOCSY transfer at low RF power demonstrate the larger bandwidth of the new pulse: at low power levels we observe FLOPSY failing to resolve cross peaks near the edges of the spectrum, while NF4's spectrum at equal or lesser RF power levels includes all expected peaks.

Relaxation processes are continually diminishing the NMR signal during all stages of an experiment. The autorelaxation rates of spins aligned with the longitudinal axes differs from

the rate for spins in the transverse plane, and for complicated magnetization trajectories, the two rates combine to form an *effective* autorelaxation rate. Similarly, in the case of cross relaxation the magnetization trajectories of the two involved spins determines the effective rate. In Section 4.3 the effective relaxation rate during a multi-frame pulse are compared with the rate for FLOPSY-16. This analysis is carried out for both autorelaxation and cross relaxation, although the former is usually more relevant for TOCSY. Although relaxation was not considered in the derivation of pulse parameters, the effective autorelaxation rates are no worse than for FLOPSY.

Two standard metrics have previously been defined for the performance of TOCSY pulses. These are called active bandwidth and quality factor. In Section 4.4, the multi-frame method is modified in order to create pulses with either high active bandwidth or high quality factor. Simulations suggest that multi-frame pulses can have active bandwidth or quality factor that surpasses what has been achieved by any known computer optimized pulses.

4.1 Transforming the J-coupling tensor into new frames.

In Chapter 2, isolated spins were expressed in a series of tilted, rotating frames. These frame changes, in concert with the suggested parametric form of the pulse, ensured that spins sampled from a large bandwidth of chemical shift frequencies were effectively spin-locked to the y-axis. Crucially, spins with different chemical shifts were expressed in different frames (although these frames all fell into alignment periodically).

In this section, two isotropically coupled spins are expressed in their respective tilted, rotating frames, and the effect on their coupling is calculated. For two spins I and S, with frequencies ω_{I} and ω_{S}, the total density matrix and Hamiltonian are transformed by the

Figure 4.1: (next page) Assigned TOCSY spectrum and coupling topology. Mixing experiments in this thesis were mostly performed on a synthetic pentapeptide PIFHA, which was ^{13}C- and ^{15}N-labeled. The sample preparation is described elsewhere (Coote et al. 2013). **A.** TOCSY spectrum of the aliphatic carbons in the pentapeptide, recorded using a 3.5 kHz RF power multi-frame pulse. The pulse parameters are given in Table 2.1. The mixing time is 29 ms and the carrier frequency is 40 ppm. All cross peaks are resolved over the 6.25 kHz bandwidth. All peaks are in -phase; colors are added to clarify the resonance assignment. **B.** There are three kinds of coupling networks in the sample. Alanine, histidine, and phenylalanine have two coupled aliphatic carbon nuclei. These residues each generate two diagonal peaks and two cross peaks. Isoleucine has five spins in a non-linear (i.e. branched) network, and produces five diagonal peaks and 20 cross peaks. Proline has four spins in a linear chain, and also a small two-bond coupling between the alpha and delta nuclei. It has four diagonal peaks and twelve cross peaks. There are 15 diagonal peaks and 38 cross peaks in the fully resolved spectrum. These residues also contain further spins that resonate at frequencies that are outside of the aliphatic region.

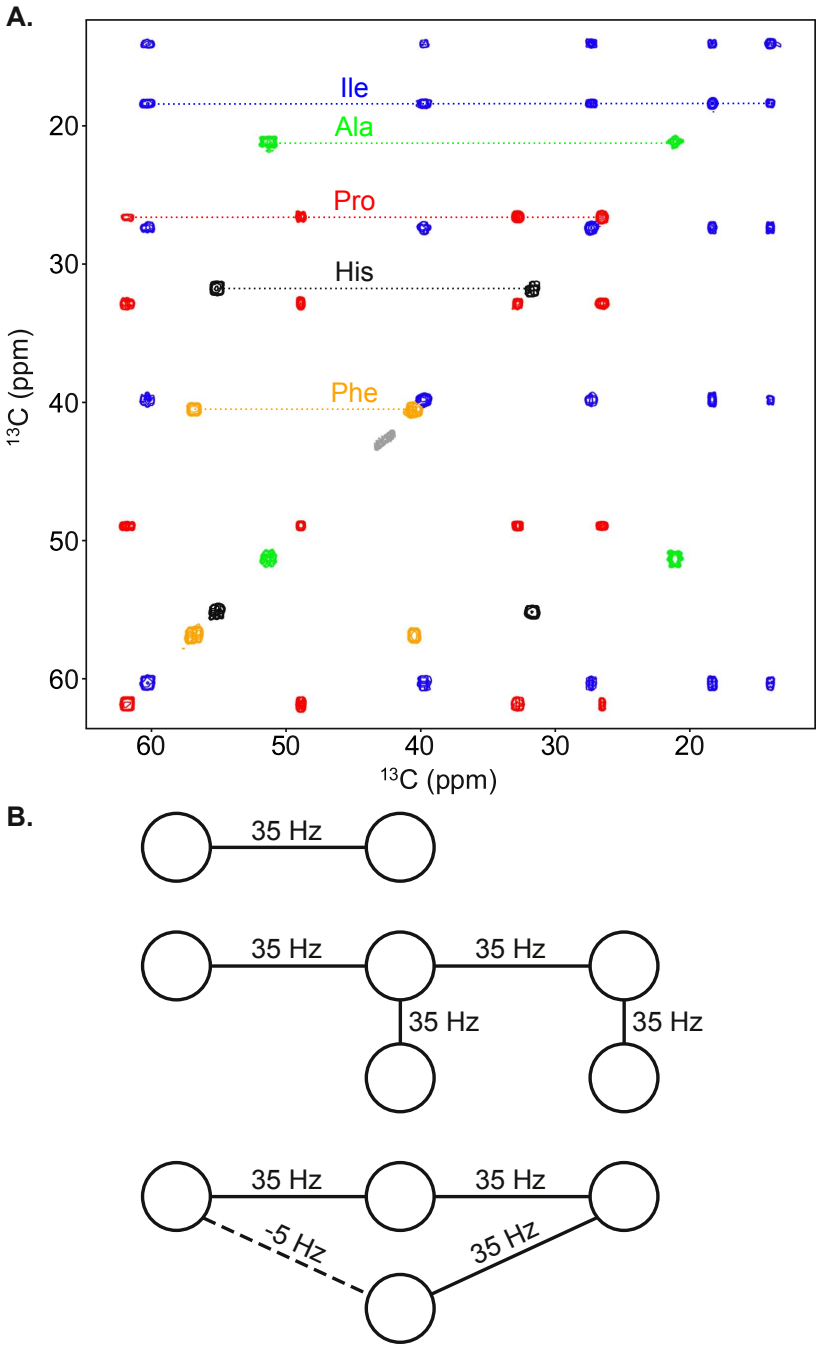
A.
Ile
Ala
Pro
His
Phe
20
30
40
50
60
^{13}C (ppm)
60
50
40
30
20
^{13}C (ppm)
B.
35 Hz
35 Hz
35 Hz
35 Hz
35 Hz
35 Hz
35 Hz
-5 Hz
35 Hz

unitary matrix

$$U = \exp(-if_1 tI_z)\exp(i\text{atan2}(u_0, \omega_I)I_y) \otimes \exp(-if_1 tS_z)\exp(i\text{atan2}(u_0, \omega_S)S_y)$$

This says that the two spins are tilted through different angles about their respective y-axes, and precess at rate f_1 about their (new) respective z-axes. It has been demonstrated already that this procedure causes the chemical shift and RF Hamiltonians for each spin to average out into effective spin-locking about the y-axis. Now, this set of frame-changes is applied to the coupling Hamiltonian.

In the original frame of reference, the coupling Hamiltonian for spins I and S is

$$H_J = 2\pi JI.S = 2\pi J(I_z S_z + I_x S_x + I_y S_y)$$

Under the multi-frame spin-locking procedure, each spin's frame is tilted differently. Spin I is tilted by $\theta = \text{atan2}(u_0, \omega_I)$, while spin S is tilted by $\phi = \text{atan2}(u_0, \omega_S)$. The time-averaged coupling Hamiltonian in the first tilted, rotating frame is

$$\overline{H_J^{(1)}} = 2\pi J(\cos(\theta - \phi)I_z S_z + \frac{\cos(\theta - \phi) + 1}{2}(I_x S_x + I_y S_y))$$

The range of tilt angles in the ensemble is determined by the RF amplitude allowance for $|u_0|$ and the chemical shift bandwidth. This equation has previously been used for dual-band nutating frame spectroscopy (Grzesiek and Bax 1995), but it is also valid for a single broad spectral region. This calculation must now be generalized to the case of a series of rotating frame constructions, since subsequent frame tilts and rotations further truncate the effective coupling strength. If the tilt angles for the k^{th} change of frames are θ_k (for spin I) and ϕ_k

(for spin S), then the components of the average coupling Hamiltonian evolve as

$$\begin{aligned}\overline{H_{\mathrm{J}}^{(\mathrm{k})}} &= a_{\mathrm{k}} I_{\mathrm{z}} S_{\mathrm{z}} + b_{\mathrm{k}} (I_{\mathrm{x}} S_{\mathrm{x}} + I_{\mathrm{y}} S_{\mathrm{y}}) \\ \begin{bmatrix} a_{\mathrm{k+1}} \\ b_{\mathrm{k+1}} \end{bmatrix} &= \begin{bmatrix} \cos(\theta_{\mathrm{k}})\cos(\phi_{\mathrm{k}}) & \sin(\theta_{\mathrm{k}})\sin(\phi_{\mathrm{k}}) \\ \sin(\theta_{\mathrm{k}})\sin(\phi_{\mathrm{k}})/2 & (\cos(\theta_{\mathrm{k}})\cos(\phi_{\mathrm{k}})+1)/2 \end{bmatrix} \begin{bmatrix} a_{\mathrm{k}} \\ b_{\mathrm{k}} \end{bmatrix}\end{aligned} \tag{4.1}$$

The initial conditions are $a_0 = b_0 = 2\pi J$. Only the time-averaged values are retained after each frame change; the parts that oscillate at multiples of frequency f_{k} are neglected. These terms average out during the pulse. In practical applications, J is tens of Hertz, while f_{k} is kilohertz, so the suppressed terms are very weak and highly oscillatory, and are therefore negligible.

Two cases in particular are worth exploring: firstly, when ω_{I} and ω_{S} are equal. This is the main diagonal of a two dimensional spectrum. In this case, for all k, $(a_{\mathrm{k}} + b_{\mathrm{k}})/2 = 2\pi J$, so that $I_{\mathrm{y}} \rightarrow S_{\mathrm{y}}$ in time $t_{\mathrm{mix}} = 1/(2J)$. Secondly, when $\omega_{\mathrm{I}} = -\omega_{\mathrm{S}}$ and the separation is large, so that $\theta_1 = \phi_1 + \pi$. This occurs in dual-band pulses (discussed in Chapter 5). In this case, $a_1 = -2\pi J$ and $b_1 = 0$; that is, an effective coupling is maintained that is orthogonal to the spin-locking axis. Since $(a_{\mathrm{k}} + b_{\mathrm{k}})/2 = -\pi J$, the apparent strength of the coupling is halved, and dual-band pulses will transfer polarization between a scalar-coupled pair in time $t_{\mathrm{mix}} = 1/J$.

In general, the cross-polarization during the mixing period can be approximated by the average Hamiltonian in the n^{th} frame. Let T be the pulse time, r be the number of times the pulse is repeated, and $V(t)$ be the unitary solution to the Schrödinger equation for the coupled two spin system, expressed in the n^{th} frame of reference. At times $t = rT$, the n^{th} frame is tilted about the y-axis with respect to the original frame (see (2.5)). This tilt commutes with density matrices that are spin-locked to the y-axis, and with the measurement operators of interest, I_{y} and S_{y}, so it has no effect of the measurement expectation values

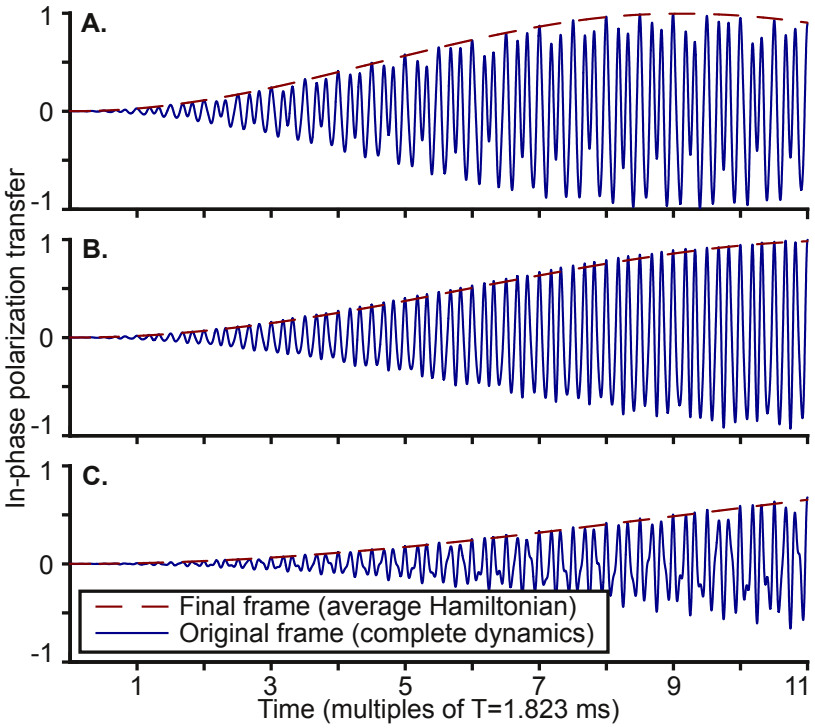

Figure 4.2: Homonuclear cross-polarization using the n$^{\text{th}}$ frame average Hamiltonian (4.2) is compared to the complete Schrödinger dynamics in the original frame, for various chemical shift offsets. $J_{\text{IS}} = 35$ Hz, the initial density matrix is $\rho(0) = I_{\text{y}}$, and the in-phase transfered magnetization $2\text{tr}(S_{\text{y}}\rho(t))$ is plotted. The average power is 3.5 kHz, and the pulse parameters are given in Table 2.1. Crucially, the magnetization is in-phase along the y-axis precisely at integer multiples of time T, when the y-axes of all frames are aligned. Chemical shift offsets in the original frame of reference are $\omega_{\text{I}} = 1$ kHz and **A.** $\omega_{\text{S}} = -1$ kHz, **B.** $\omega_{\text{S}} = -2$ kHz, and **C.** $\omega_{\text{S}} = -3$ kHz. The rate of transfer is slower for the the more widely separated pairs of spins.

(Isham 1995). Therefore, $V(t)$ is adequate for modeling in-phase cross-polarization in frame 0 as well as frame n. Then

$$\begin{aligned}\overline{H^{(n)}} =& a_{\text{n}} I_{\text{z}} S_{\text{z}} + b_{\text{n}}(I_{\text{x}} S_{\text{x}} + I_{\text{y}} S_{\text{y}}) + \\ & v_{\text{n}}(I_{\text{y}} + S_{\text{y}}) + \omega_{\text{n}}(\omega_{\text{I}}) I_{\text{z}} + \omega_{\text{n}}(\omega_{\text{S}}) S_{\text{z}} \\ V(rT) \approx& \exp(-i\overline{H^{(\text{n})}} rT) \end{aligned} \tag{4.2}$$

where a_{n} and b_{n} are generated by (4.1), v_{n} is the time-invariant effective pulse applied in

the final frame, and the two ω_{n} are generated by applying the recursion (2.2) to the initial chemical shifts ω_{I} and ω_{S} (by design, these ω_{n} values are much smaller than v_{n}). These constants can be calculated from the pulse parameters and chemical shifts much faster than a full simulation of the time-varying Hamiltonian in the original frame of reference. However, the y-axes for these frames align at times $t = rT$. For polarization transfer between coupled spins (which are spin-locked to the y-axis in the n^{th} frame), $(a_{\mathrm{n}} + b_{\mathrm{n}})/2$ must be large enough to dominate the residual chemical shifts $|\omega_{\mathrm{n}}| \leq C_{\mathrm{n}}$. In other words, the Hartmann-Hahn mixing condition must be satisfied for the average Hamiltonian in the final frame, for all desired pairs of chemical shift offsets. Figure 4.2 compares (4.2) to the complete dynamics in the original frame of reference, and shows that cross-polarization (at stroboscopic times) can be accurately predicted by the average Hamiltonian in the final tilted, rotating frame.

4.2 Mixing efficiency and example tocsy pulses

In this section, several example broadband mixing pulses are designed, simulated, and tested experimentally. Particular attention is paid to the bandwidth of these pulses compared to the widely-used FLOPSY-16 sequence, which is generally considered to be the best available broadband mixing sequence (Cavanagh et al. 2007; Kovacs and Gossert 2014).

The most thoroughly tested of these is called NF4 (for 4^{th} nutating frame). It has been demonstrated to have considerably higher bandwidth than FLOPSY and good relaxation properties (Coote et al. 2014).

At the end of this section, it is argued that adding more modulations (i.e. more rotating frame constructions) to the design process cannot further increase the mixing bandwidth. With high numbers of frames, effectively decoupled pairs of spins within the spin-locked bandwidth are unavoidable.

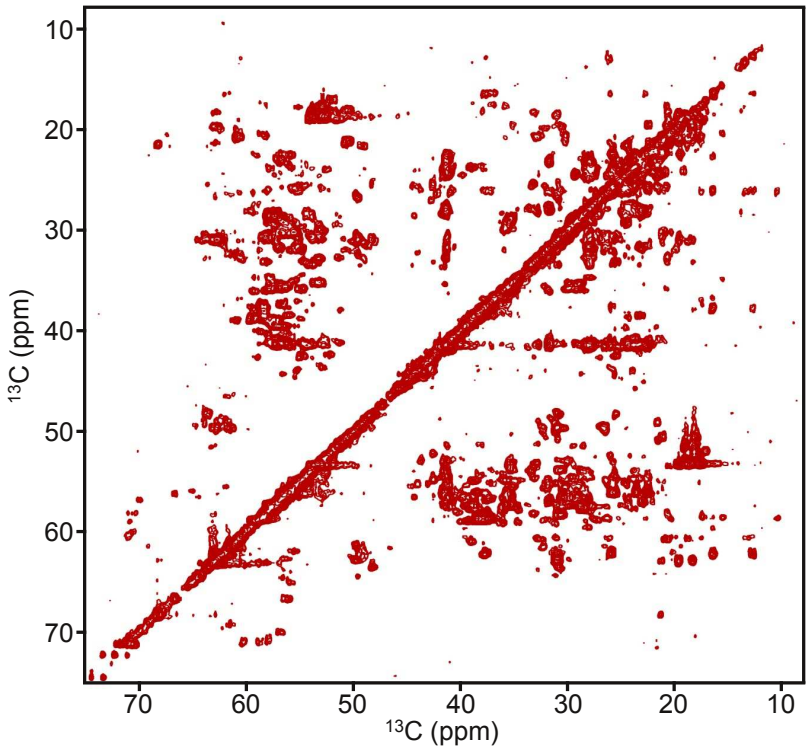

Figure 4.3: A 3.5 kHz multi-frame mixing pulse is used for TOCSY of the protein human carbonic anhydrase II. The pulse was designed using three rotating frames. Cross peaks are resolved over a broad spectral width.

4.2.1 Example 1: A three-frame pulse

The pulse shape depicted in Figure 2.2 and used as an example throughout Chapter 2 has also been tested for homonuclear mixing. The pulse parameters are given in Table 2.1, and the robustness to RF inhomogeneity of this pulse was demonstrated in Figure 2.4. Figure 4.2 is a simulation of mixing with this pulse at a power level of 3.5 kHz. Transfer of magnetization is simulated for chemical shift differences ranging from 2 to 4 kHz. The in-phase magnetization buildup on the destination spin is slower for more widely separated spin pairs, as is typical for TOCSY pulses.

The spectrum in Subfigure 4.1A, in which the pentapeptide sample's resonance assignment is shown, was recorded using this pulse. The power level was 3.5 kHz, and the mixing

time was $16T = 29$ ms. All the expected cross peaks in the carbon aliphatic region were resolved. This pulse has also been tested on a protein sample, human carbonic anhydrase II. This sample has a molecular mass of 29 kDa, and contains 260 amino acids. As usual, the sample has been enriched with NMR-active nuclei (carbon-13 and nitrogen-15). The spectrum is displayed in Figure 4.3. Qualitatively, the pulse appears to be functioning properly, since cross peaks have appeared over a wide spectral width, in agreement with theory and simulation results.

These tests show that the three-frame pulse performs as expected, and can be substituted into standard protein NMR experiments. However, the mixing bandwidth is approximately equal to the standard sequence FLOPSY-16. To be useful for NMR spectroscopy, multi-frame pulses must outperform existing options. The next two example broadband pulses have been shown to have higher bandwidth than FLOPSY-16.

4.2.2 Example 2: A four-frame pulse

The second example pulse designed by multi-rotating frames is compared to the FLOPSY-16 sequence in Figure 4.4. The average RF amplitude is set to 2.6 kHz. This power level was chosen in order to demonstrate the different bandwidths of FLOPSY and the candidate multi-frame pulse: FLOPSY fails to cover the aliphatic peaks in the pentapeptide sample, whereas the multi-frame pulse resolves all cross peaks in the same sample. The pulse parameters are given in Table 4.1.

Subfigures 4.4A and 4.4B are simulations of homonuclear cross-polarization between two isotropically coupled spins, under FLOPSY-16 and the multi-frame pulse, demonstrating the larger bandwidth of the latter. The J-coupling is 26.5 Hz. The multi-frame pulse was run eight times in immediate succession, while FLOPSY-16 was run once, so the that the mixing time was close to $t_{\mathrm{mix}} = (2J)^{-1}$ for both pulses. RF inhomogeneity and relaxation effects were ignored.

	$k=0$	1	2	3
u_k/v_3	1.956	1.038	0.391	$v_3 = 0.158$
f_k	-	2.943	1.261	0.420
Tf_k	-	7	3	1

Table 4.1: Pulse amplitudes and frequencies (in kHz) for the second example broadband TOCSY pulse described in Subsection 4.2.2. The pulse time is $T = 2.379$ ms and the RF power is 2.6 kHz. These four amplitudes and three frequencies, along with the pulse time, completely determine the pulse shape via (2.4). The pulse can be repeated to achieve spin-locking for longer periods of time.

Subfigures 4.4C and 4.4D compare the pulses in experiment. The multi-frame pulse resolves several cross peaks around the edge of the spectrum that are not present in the FLOPSY spectrum. In particular, the five-spin isoleucine pattern is missing peaks along the top and down the right hand side under FLOPSY-16 (Subfigure 4.4C). These peaks are clearly resolved in the multi-frame TOCSY spectrum (Subfigure 4.4D). Also, the four-spin proline pattern along the bottom and left hand side of the spectrum is mostly missing from Subfigure 4.4C, but all expected cross peaks are present in Subfigure 4.4D. The three two-spin systems in the sample—alanine, histidine, and phenylalanine—are well-resolved in both spectra. The observation of missing peaks around the edges of the FLOPSY spectrum confirms that the multi-frame pulse has higher bandwidth-to-RF power ratio than FLOPSY-16 in identical experimental settings.

4.2.3 Example 3: NF4

The final example broadband mixing pulse is called NF4, for 4^{th} nutating frame mixing. NF4 was designed to resolve the aliphatic carbon spectrum at lower RF power than other available pulses. The root-mean-square average RF power is 3 kHz and the duration is $T = 3.477$ ms. The pulse can, as usual, be repeated to achieve a desired mixing time, and the power level and duration can be inversely scaled to achieve any RF power. The bandwidth changes

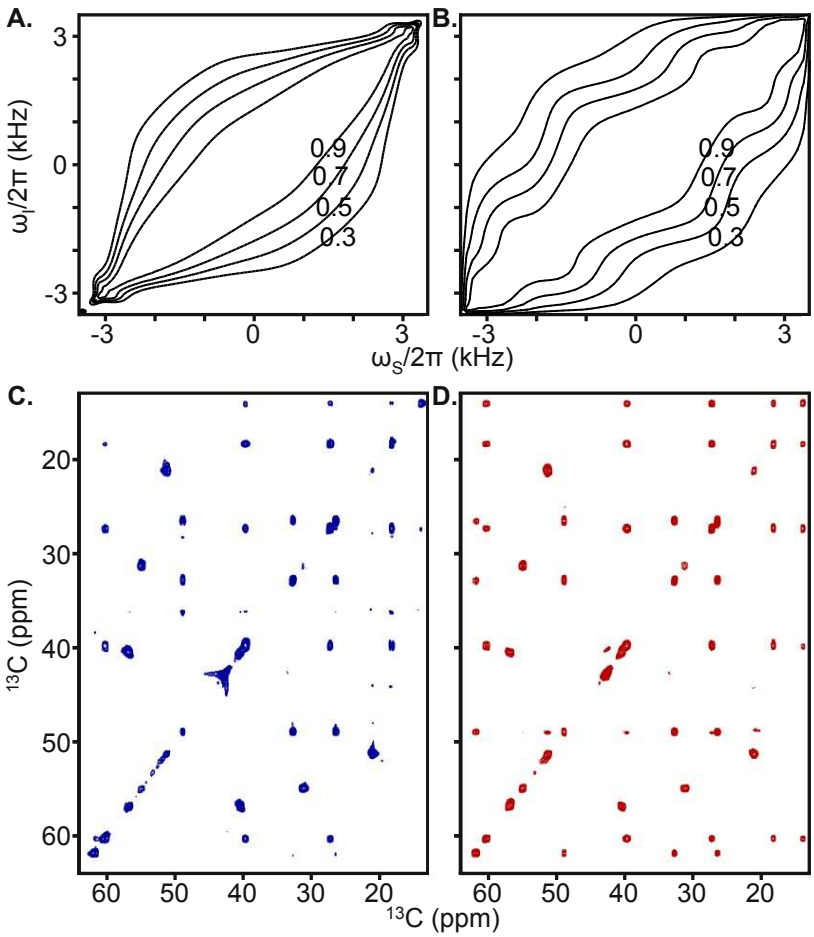

Figure 4.4: A mixing pulse designed with three tilted, rotating frames is compared to FLOPSY in simulation and experiment on the PIFHA peptide. The average RF power is 2.6 kHz, and the parameters are listed in Table 4.1. **A.** FLOPSY-16 simulation of in-phase transfer $I_z \rightarrow S_z$ as a function of offset frequencies. $J_{IS} = 26.5$ Hz so that the FLOPSY-16 duration is $1/(2J_{IS})$. **B.** Multi-frame simulation of in-phase transfer $I_y \rightarrow S_y$. The pulse is repeated eight times to achieve approximately the same mixing time as FLOPSY-16. The coupling is $J_{IS} = 26.5$ Hz. **C.** FLOPSY-16 is applied to a sample. It fails to resolve, or weakly resolves, various cross peaks near the edges of the spectrum. **D.** The multi-frame pulse resolves all cross peaks in the aliphatic spectral region. The average RF amplitude, carrier frequency, mixing time (37 ms), number of scans, and display settings are the same for the two spectra.

proportionally to the power. The pulse parameters were expressed for an RF power level of 3 kHz arbitrarily. The pulse parameters are given in Table 4.2.

TOCSY transfer was simulated as a function of the offset frequencies of the two isotrop-

ically coupled spins with $J_{IS} = 35$ Hz. Subfigures 4.5A,B compare the transfer $I_y \rightarrow S_y$ for NF4 with $I_z \rightarrow S_z$ under FLOPSY-16. Relaxation effects and RF inhomogeneity were neglected during the mixing time. Note that the unitary propagator (solution to the time-dependent Schrödinger equation) was simulated for one period of each pulse, with duration t_p, and then the propagator for the desired mixing time t_m was calculated via $U(0, t_m) = U(0, t_p)^{t_m/t_p}$. In experiments, we can only repeat the *complete* pulse, i.e. t_m/t_p must be an integer; however, in simulations we can set t_m/t_p to a non-integer to ensure that $t_m = 1/(2J_{IS})$. In Subfigures 4.5A and 4.5B NF4 had $t_m/t_p = 4.12$, and FLOPSY-16 had $t_m/t_p = 0.91$. Note that the duration of NF4 is only 22% as long as FLOPSY-16 per repetition, so that in experiments a desired mixing time can be chosen more precisely with NF4.

Subfigures 4.5C–E show traces of the transferred magnetization onto the S spin, for three different offsets of the I spin. Both pulses were simulated for a whole (integer) number of repetitions, and the J-couplings were adjusted so that the mixing time was $t_m = 1/(2J_{IS})$. These simulations include RF inhomogeneity uniformly distributed between ±10%. Relaxation was ignored.

Clearly, transfer is achieved for a larger range of offsets under NF4 along the main diagonal. The width along the anti-diagonal is similar for the two pulses—FLOPSY is about 8% wider on resonance, in terms of full-width at half-maximum measured on Subfigure 4.5C. However, when spin I is 2 kHz off-resonance, NF4 is 6% wider than FLOPSY (Subfigure 4.5D). Moreover, NF4 continues to function properly for offsets outside the working bandwidth of FLOPSY (Subfigure 4.5E).

For the aliphatic carbons, the bandwidth of chemical shifts is around 80 ppm. However, characteristic chemical shift values from the Biological Magnetic Resonance Data Bank (Ulrich et al. 2008) show that the largest chemical shift *differences* between any two directly bonded nuclei are about 48 ppm (for the $J_{\beta\gamma 2}$ coupling in threonine) followed by 30-35 ppm

	$k=0$	1	2	3	4
u_k/v_4	1.9285	1.0880	0.7450	0.2755	v_4 =0.0734
f_k	0	4.0260	1.7254	0.8627	0.2876
Tf_k	0	14	6	3	1
C_{k}	5.8118	2.0975	0.6374	0.1177	0.0121

Table 4.2: The amplitudes u_k and frequencies f_k of the modulations in each frame in kHz for NF4, described in Subsection 4.2.3. This list of parameters completely determines the pulse shape via (2.4). The root-mean-square RF power is 3 kHz and he pulse time is $T = 3.477$ ms. The limits of the bandwidth of chemical shifts in each frame are also listed. The spin-locking bandwidth in the original frame, $2C_0$, is over 11 kHz.

(for the $J_{\alpha\beta}$ couplings in alanine and proline). Other residues, such as isoleucine, have large overall bandwidth, but have smaller separations between directly bonded spin pairs, and so require large bandwidth on the main diagonal but smaller anti-diagonal bandwidth. Therefore, to resolve the aliphatic carbon TOCSY spectrum at low power, the pulse needs to have bandwidth 80 ppm along the main diagonal, and needs to maintain a width along the anti-diagonal of 40-50 ppm. Figure 4.5 suggests that NF4 is well-suited to this application.

Experimental tests of NF4 were carried out on the synthetic pentapeptide PIFHA, using a Bruker 500 MHz spectrometer equipped with a cryogenically cooled TXO probe. The TOCSY experiments were performed with proton and nitrogen decoupling during the indirect and direct dimension carbon evolution. The shaped amplitude and phase profiles of the NF4 mixing pulse were finely discretized due to spectrometer software requirements (the discretization sampling time was $T/500$). The pulse shape was repeated 9 times to achieve a mixing time of $9T$. The FLOPSY-16 sequence was repeated 2 times. This ensured approximately equal mixing times for the two sequences: at 3 kHz power the mixing times were 31.29 ms for NF4 and 31.41 ms for FLOPSY-16, and proportionally longer for the lower RF power trials (since pulse durations scale inversely with power levels). The experiments

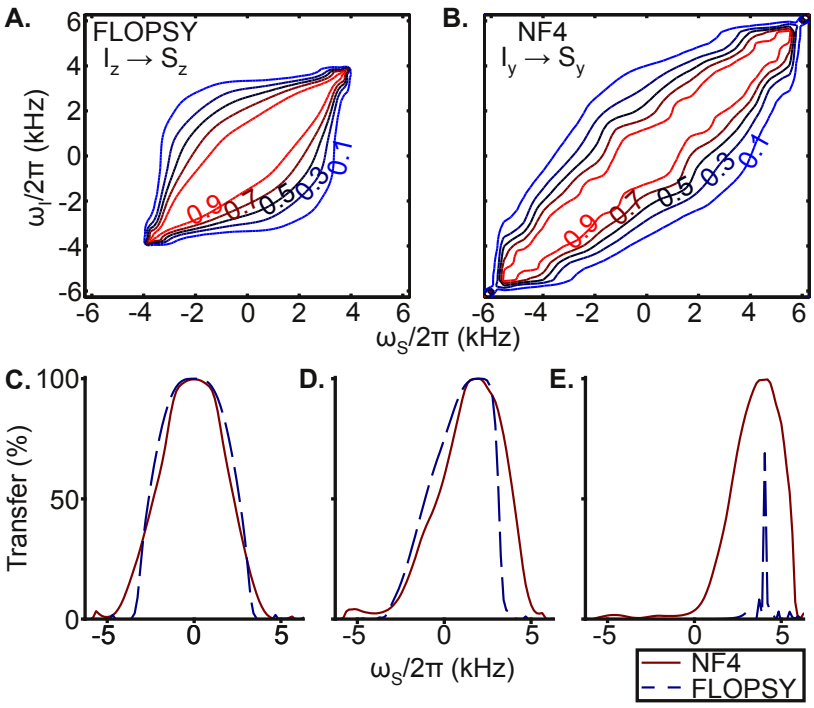

Figure 4.5: Simulated transfer of magnetization for two isotropically coupled spins under NF4 and FLOPSY-16. The mixing time is $t_m = 1/(2J_{IS})$ and the RF power is 3 kHz. **A.** FLOPSY-16 transfer $I_z \rightarrow S_z$ with with $J_{IS} = 35$ kHz. **B.** NF4 transfer $I_y \rightarrow S_y$ with $J_{IS} = 35$ kHz. Contour levels show the proportion of in-phase magnetization originally on the I spin that has migrated to the S spin at time t_m. Both pulses have high transfer efficiency near the main diagonal, which decreases away from the main diagonal. NF4 has a wider bandwidth along the main diagonal.
Simulations were also performed of transfer of magnetization from a spin which is **C.** on resonance, **D.** 2 kHz offset, and **E.** 4 kHz offset. FLOPSY-16 transfers (dashed lines) are $I_z \rightarrow S_z$, while NF4 transfers (solid lines) are $I_y \rightarrow S_y$. Transfers in time $1/(2J_{IS})$ are plotted as a function of offset frequency of the S spin, averaged over 20 values of RF inhomogeneity uniformly distributed between ± 10 %. The average RF power is 3 kHz, and $J_{IS} = 31.85$ for FLOPSY and $J_{IS} = 36$ for NF4, so that the mixing time is an integer multiple of the pulse time. At $\omega_I = 0$ kHz, the FLOPSY-16 transfer profile is marginally wider than the NF4 profile, however at $\omega_I = 2$ kHz, the NF4 profile is wider. At $\omega_I = 4$ kHz FLOPSY-16 is not effective, while NF4 still transfers magnetization to a broad range of offsets ω_S.

were done at 298 K. The spectra were processed and plotted with NMRPipe (Delaglio et al. 1995), and are presented in Figure 4.6.

At the highest power tested (3 kHz) all the expected intra-residue cross peaks were resolved

Figure 4.6: (next page) 2D-TOCSY spectra recorded using FLOPSY-16 (left column) and NF4 (right column). The root-mean-square average RF power is (**A.**, **B.**) 1.8 kHz, (**C.**, **D.**) 2.2 kHz, (**E.**, **F.**) 2.6 kHz, and (**G.**, **H.**) 3 kHz. The sample is the pentapeptide PIFHA. The carrier frequency, number of scans, and display settings are the same for all spectra, and the mixing times are approximately equal at each power level. We observe that NF4 resolves all cross peaks for power levels of at least 2.2 kHz, whereas FLOPSY-16 requires 3 kHz power to resolve all cross peaks. The isoleucine and alanine patterns are labeled in **H.**

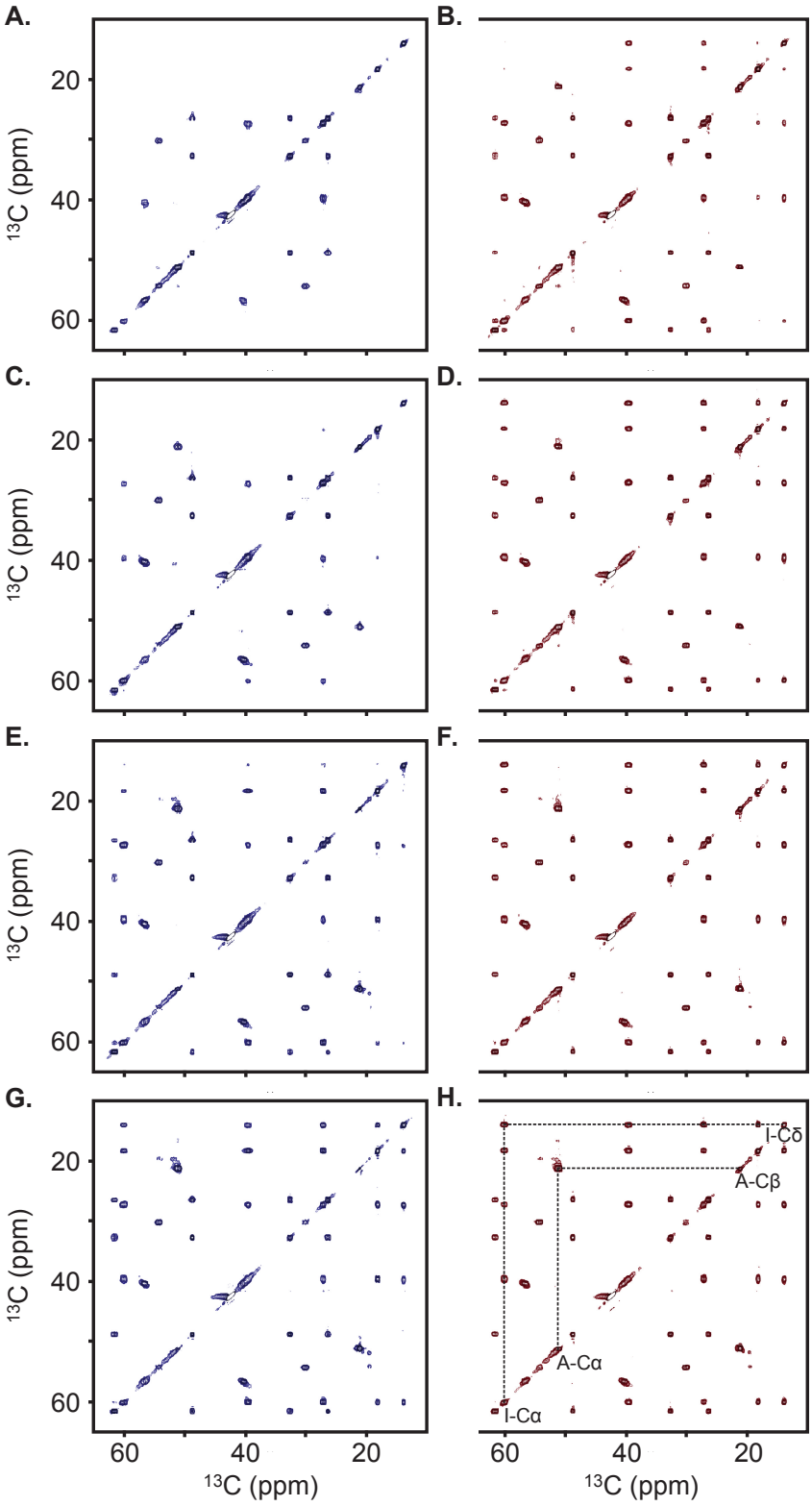
A.
B.
C.
D.
E.
F.
G.
H.
20
40
60
^{13}C (ppm)
I-Cδ
A-Cβ
A-Cα
I-Cα

by both mixing sequences. However, NF4 resolves all cross peaks for power levels of at least 2.2 kHz, while FLOPSY requires the full 3 kHz power. This suggests that the working bandwidth of NF4 is approximately 35% larger than for FLOPSY-16 (although this single metric does not really capture the differing shape of the two sequences' transfer efficiencies along the main diagonal and the anti-diagonal).

The difference in practical performance is clearly illustrated with the mixing patterns of isoleucine and alanine, which are labeled in Subfigure 4.6H. With FLOPSY, the mixing between the the CA and CB nuclei of alanine (separated by approximately 30 ppm) is observed at 2.2 kHz and above. However, with NF4 this cross peak can clearly be seen at 1.8 kHz power in Subfigure 4.6B. Similarly, the mixing between isoleucine CD and CA nuclei fails below a field strength of 3 kHz for FLOPSY. However, with NF4 the isoleucine pattern is weakly resolved at 1.8 kHz and clearly observed at 2.2 kHz. This is because of the increased bandwidth of NF4 along the main diagonal, shown in Figure 4.5. Although the CD and CA nuclei are 50 ppm apart, they are connected via sequential bonds with smaller separations, and each of the directly coupled spin pairs in isoleucine maintains a strong coupling under NF4, even at low RF power.

NF4 will be especially useful for experiments such as CACA-TOCSY (Takeuchi et al. 2010) (which requires a mixing time on the order of hundreds of ms to resolve weak inter-residue couplings, and therefore requires a mixing pulse with low RF power) and in applications that are sensitive to sample heating from RF pulses (Hiller et al. 2009). The direct comparison of the FLOPSY-16 sequence with NF4, first using simulations, and then under identical experimental conditions, demonstrated that the mixing bandwidth of NF4 is about 35% greater than FLOPSY-16. Furthermore, NF4 is robust to reasonable RF inhomogeneity. Because of these favorable properties, NF4 is a better choice for use in broadband TOCSY applications than other available pulses.

4.2.4 Large numbers of frames

With three rotating frames, it is possible to create a pulse which outperforms the FLOPSY-16 sequence. With four frames, the bandwidth can be increased even further, as evidenced by NF4. This raises the question of how broadband a multi-frame mixing pulse can be. In Chapter 2, it was demonstrated that increasing the number of frames, n, led to an increase in spin-locking bandwidth at rate $2^{n/2}$. However, the J-coupling cannot be maintained for all spin pairs for arbitrarily high bandwidths.

This can be understood in the following way. The time-averaged coupling is scaled down by each frame change in accordance with (4.1). In the presence of spin-locking about the y-axis, the effective magnitude of the coupling interaction is given by the average of the I_zS_z and I_xS_x terms, $\frac{1}{2}(a_k + b_k)$. This means that in frame 1 the coupling is scaled down (i.e. $J \to s_1 J$) from its intrinsic strength by

$$s_1(\omega_I,\ \omega_S) = \frac{3}{4}\cos(\theta_1 - \phi_1) + \frac{1}{4}$$

This is zero for $\theta_1 - \phi_1 = 109.5°$, i.e. when $|\omega_I - \omega_S| \approx 2\sqrt{2}u_0$. The power allocated to u_0 limits the mixing bandwidth of the pulse, and u_0 cannot be increased beyond the total RF power A of the pulse. Indeed, some power must be reserved for the remaining pulse amplitudes, so that u_0 must be lower than the pulse's RF power. Therefore, spin-locking bandwidths of greater than $2\sqrt{2}A$ will invariably contain pairs of resonance frequencies which are effectively decoupled.

Figure 4.7 shows the effect on the mixing efficiency of adding more rotating frames. The pulses were designed to have $C_n/v_n = 8.8$, total power 3 kHz, flip angle $\alpha = v_nT = \pi/2$, and frequencies $f_k = 2f_{k+1}$. All remaining parameters are fixed by (2.10) and (2.11). For the three-frame pulse, $u_0 = 1.81$ kHz, and mixing can be observed for spins with chemical shift differences of up to about 5 kHz in Subfigure 4.7A.

Adding a fourth rotating frame increases the bandwidth along the main diagonal (Subfigure 4.7B). However, now $u_0 = 1.40$ kHz, and there is no mixing between spins with chemical shift differences of about 4 kHz. Near the opposite edges of the bandwidth, i.e. $|\omega_I - \omega_S| \approx 10$ kHz, the tilt angles are $\theta_1 - \phi_1 > 109.5°$; that is, these widely-separated spins are far enough from resonance that they are beyond the zero at 109.5°. A slow transfer of magnetization is observed in the simulation for these spin pairs.

For the case of five tilted, rotating frames (Subfigure 4.7C), the power applied in the original frame is $u_0 = 1.06$ kHz. The reason that the magnitude of u_0 is decreasing with each additional frame is that an extra modulation, with amplitude u_n is being added to the pulse, which requires some of the available power. The zero in the effective coupling strength occurs for spin pairs with chemical shift separations of about 3 kHz. For widely separated spins from near opposite edges of the bandwidth, some polarization transfer occurs. The five-frame pulse has significantly increased bandwidth along the main diagonal, but has insufficient power in u_0 to maintain a strong J-coupling for spin pairs away from the diagonal.

Adding further rotating frames exacerbates this problem. It is easy to increase the bandwidth along the main diagonal, but much more difficult to ensure a strong coupling for spin pairs away from the diagonal.

4.3 Analysis of relaxation

Relaxation processes are continually diminishing the signal throughout the NMR experiment. Before using a new TOCSY pulse, it is important to understand its relaxation properties. Autorelaxation, by which individual spins tend to move towards their equilibrium state aligned with the z axis, is particularly relevant to TOCSY. It is described by two rate parameters R_1 and R_2. R_1 is the rate at which longitudinal magnetization moves towards equilibrium; R_2 is the rate at which transverse magnetization components (I_x and I_y) decay

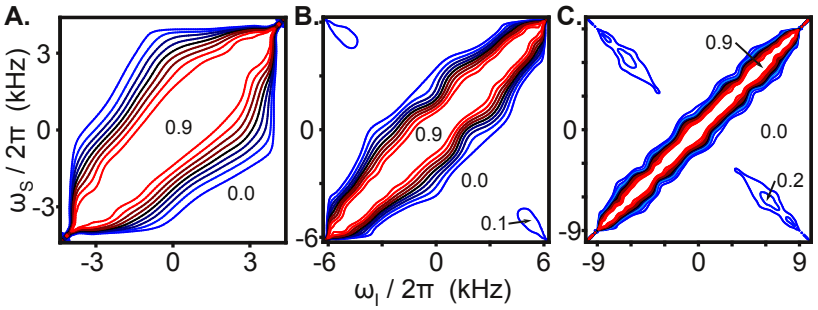

Figure 4.7: Transfer efficiency with large numbers of frames. **A.** A pulse designed with three rotating frames exhibits broadband polarization transfer. **B.** With four frames, the bandwidth is significantly increased along the main diagonal. However, the off-diagonal efficiency is not increased. **C.** Adding a fifth frame further increases the main-diagonal bandwidth, but the pulse has poor off-diagonal efficiency. Each simulation had an RF power level of 3 kHz, coupling strength of 35 Hz, and mixing time of $t_{\text{mix}} = (2J_{\text{IS}})^{-1}$. Relaxation and RF inhomogeneity were ignored.

towards zero (Levitt 2008).

FLOPSY-16 transfers longitudinal magnetization $I_z \rightarrow S_z$, while multi-frame pulses transfer transverse magnetization $I_y \rightarrow S_y$. Longitudinal relaxation (R_1) is generally far slower than transverse relaxation (R_2) (Cavanagh et al. 2007), suggesting the possibility that multi-frame pulses could produce more rapid loss of signal than FLOPSY. However, analysis of the magnetization trajectories *during* the pulse reveals very similar autorelaxation performance. The simulations presented here use the pulse NF4 as an example.

During an RF pulse, magnetization will follow a trajectory that is (in general) not always aligned with the longitudinal axis nor always contained in the transverse plane. Therefore, it is subject to a mixture of R_1 and R_2 relaxation effects. The method of invariant trajectories predicts relaxation based on simulated or calculated periodic magnetization trajectories on the Bloch sphere (Griesinger and Ernst 1988; Glaser and Quant 1996; Furrer et al. 2004; Felli et al. 2009). The transverse weight σ_T is the time-averaged component of magnetization in

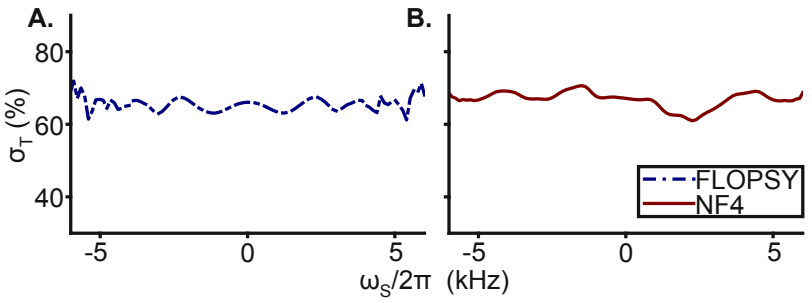

Figure 4.8: Comparison of the transverse weight of (**A.**) FLOPSY-16 and (**B.**) NF4 as a function of offset frequency. Simulations used an average RF amplitude of 3 kHz applied to an isolated spin. The time-averaged projection of the magnetization trajectory onto the $x-y$ plane during one period is plotted, averaged over 20 values of RF inhomogeneity between ± 10 %. The initial magnetization is $\rho(0) = I_z$ for FLOPSY and $\rho(0) = I_y$ for NF4. During the pulses the spins spend a similar proportion ($\sim 2/3$) of their time near the transverse plane, and are therefore subject to similar weightings of R_2 versus R_1 autorelaxation.

the $x - y$ plane,

$$\sigma_{\mathrm{T}} = \frac{1}{T}\int_0^T n_{\mathrm{x}}^2(t) + n_{\mathrm{y}}^2(t)dt$$

where $\vec{n}(t)$ is the periodic magnetization vector under the RF pulse. The transverse weight determines the effective relaxation rate R_e via

$$R_{\mathrm{e}} = \sigma_{\mathrm{T}} R_2 + (1 - \sigma_{\mathrm{T}})R_1$$

Figure 4.8 shows a simulation of the transverse weight under NF4 and FLOPSY-16 as a function of offset frequency. Simulations assumed an isolated spin without relaxation, for one period of the applied RF pulse. This signal was averaged over RF inhomogeneities uniformly distributed between $\pm 10\%$. Under either pulse, and for a wide range of offset frequencies, the magnetization vector projects onto each of the three axes for approximately equal amounts of time. This leads to a transverse weight of about 2/3 for both FLOPSY and NF4. It can be concluded that signal loss due to autorelaxation is similar for FLOPSY and NF4.

The invariant trajectories method can also be used to asses cross relaxation between pairs

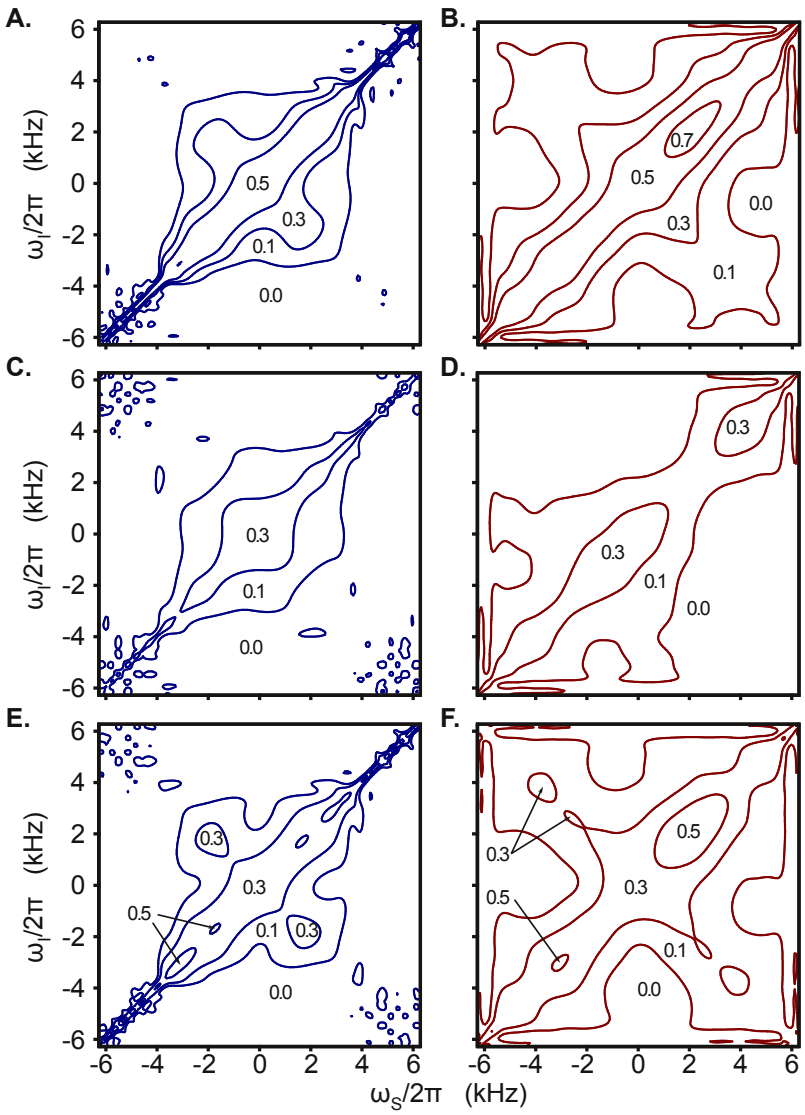

Figure 4.9: Comparison of the cross relaxation of FLOPSY-16 (left column) with NF4 (right column). **A., B.** Scaling of the transverse cross relaxation rate. **C., D.** Scaling of the longitudinal cross relaxation rate. **E., F.** For large, slowly tumbling samples, the effective cross relaxation rate is given by the transverse rate minus half the longitudinal rate. This is shown here in units of the transverse rate. In general, the cross relaxation profiles for multi-frame pulses are not as symmetric as for FLOPSY. However, the effective rates are not significantly higher than for FLOPSY.

of spins (Griesinger and Ernst 1988). Suppose that $\vec{n}(t)$ and $\vec{m}(t)$ are the periodic magnetization trajectories on the Bloch sphere for the two spins. These are found by simulating one period of the pulse and assuming isolated spins (i.e. not including and coupling or relaxation

effects). Then the scaling of the transverse cross relaxation rate is

$$s_{\mathrm{T}} = \frac{1}{T}\int_0^T n_{\mathrm{x}}(t)m_{\mathrm{x}}(t) + n_{\mathrm{y}}(t)m_{\mathrm{y}}(t)dt$$

and the scaling of the longitudinal cross relaxation rate is

$$s_{\mathrm{L}} = \frac{1}{T}\int_0^T n_{\mathrm{z}}(t)m_{\mathrm{z}}(t)dt$$

Clearly, for spins along the z-axis, $s_{\mathrm{L}} = 1$ and $s_{\mathrm{T}} = 0$. The spins cross relax at their characteristic longitudinal rate. Similarly, for spins that are locked by a strong pulse to the x- or y-axis, $s_{\mathrm{L}} = 0$ and $s_{\mathrm{T}} = 1$. In this case, the spins cross relax at their characteristic transverse rate. For more complicated magnetization trajectories, such as occur during a TOCSY pulse, the spins are subject to a mixture of longitudinal and transverse cross relaxation.

Figure 4.9 compares the scaling of transverse (Subfigures 4.9A,B) and longitudinal (Subfigures 4.9C,D) under the influence of FLOPSY-16 and NF4. The NF4 profiles are less symmetric than the FLOPSY profiles, however the rates are not significantly different. A particular case of interest is the so-called *spin-diffusion limit* of slow molecular tumbling, in which the rate of transverse cross relaxation is -2 times the longitudinal cross relaxation rate (Griesinger and Ernst 1988). Therefore, for large protein samples, the effective cross relaxation during the TOCSY pulse is

$$R_{\mathrm{cross}}^{\mathrm{eff}} = (s_{\mathrm{T}} - 0.5s_{\mathrm{L}})\, R_{\mathrm{cross}}^{\mathrm{trans}}$$

where $R_{\mathrm{cross}}^{\mathrm{trans}}$ is the intrinsic transverse cross relaxation rate. The effective rates under FLOPSY-16 and NF4 are compared in Subfigures 4.9E,F, expressed in units of $R_{\mathrm{cross}}^{\mathrm{trans}}$. Both pulses produce small regions near the main diagonal in which the effective rate is above

50% of the intrinsic transverse rate, as well as small regions off the main diagonal where the scaling is above 30%. This simulation suggests that the effective cross relaxation rates are similar for FLOPSY-16 and NF4.

4.4 Two widely-used optimization criteria

In this section, the multi-frame algorithm is adapted to respect two measures of quality that have previously been used to compare TOCSY pulses (Glaser and Drobny 1990; Glaser and Quant 1996). These criteria are, firstly, to maximize the bandwidth over which at least half the intrinsic coupling strength is maintained (called *active bandwidth*), and, secondly, to maximize the minimum rate of transfer for any two spins sampled from a certain predefined bandwidth (called *quality factor*).

4.4.1 Optimizing for $J^{\text{EFF}} \geq 0.5J$

Several researchers have defined the active bandwidth of a TOCSY sequence as two times the largest chemical shift offset Ω for which all $|\omega_{\text{I}}|,\ |\omega_{\text{S}}| \leq \Omega$ have $J_{\text{IS}}^{\text{eff}} \geq 0.5J_{\text{IS}}$. Another way of understanding this definition is as the size of the largest square which can be inscribed in the 0.5 contour line of a transfer efficiency plot (see Figure 4.10).

Although this metric is not necessarily directly proportional to the final signal in complex multi-resonance experiments, it has been adopted in various studies of TOCSY pulse performance (Kovacs and Gossert 2014; Glaser and Quant 1996). Therefore, it is a valuable exercise to optimize a multi-frame pulse with respect to this definition of bandwidth. The first step is to derive a set of necessary conditions under which 50% of the coupling strength is maintained, and then alter the design method to respect this. A finished pulse is presented in Table 4.3 and simulated in Subfigure 4.10A.

To begin, it must be ensured that the first change of frame preserves at least half the cou-

pling, for all spin pairs with chemical shift offsets sampled from within the active bandwidth. If the first frame truncates the coupling too much, then there is no way to restore it with further frame changes. Using (4.1), the average coupling in frame 1 is calculated and set to be at least half of the intrinsic coupling:

$$\frac{1}{2}(a_1 + b_1) = 2\pi J(\cos(\theta_1 - \phi_1)\frac{3}{4} + \frac{1}{4}) \geq \pi J$$
$$\cos(\theta_1 - \phi_1) \geq \frac{1}{3}$$

Therefore, $\theta_1 - \phi_1$ must be less than 70.5°, which is achieved if and only if $C_0/u_0 \leq 0.707$. Notice that the spin pair whose coupling has been truncated all the way to 50% has chemical shifts $\omega_{\mathrm{I}},\ \omega_{\mathrm{S}} = \pm C_0$. These have identical effective chemical shifts in all subsequent frames, so that no further reduction of coupling strength occurs under (4.1) for this spin pair. The following requirement is necessary to ensure that $J_{\mathrm{IS}}^{\mathrm{eff}} \geq 0.5 J_{\mathrm{IS}}$:

$$\text{Condition 1: } C_0/u_0 \leq \frac{1}{\sqrt{2}}$$

Applying the design recursion (2.10) and (2.11), along with the requirement that $C_0/u_0 = 0.707$, gives inconsistent results in general. However, we can revert to (2.7) and adjust α, which is the parameter that controls where f_1 is placed relative to the limits of the bandwidth in frame 1. Note that (2.7) and (2.8) imply a modified design recursion:

$$u_{\mathrm{k}} = f_{\mathrm{k+1}} + C_{\mathrm{k+1}}(1 - \frac{1}{\alpha_{\mathrm{k}}})$$
$$C_{\mathrm{k}} = \sqrt{(C_{\mathrm{k+1}} + f_{\mathrm{k+1}})^2 - u_{\mathrm{k}}^2}$$

which can be used to generate C_0 and u_0 (for arbitrary α_{k}) from parameters in later frames (there is no reason not to let α change in different frames, so α_{k} is used in the recursion

rather than α). In particular, increasing α_1 will decrease the ratio C_0/u_0, as required.

For the second change of frames, (4.1) must be applied again. Once again, the largest reduction in coupling strength occurs for the spin pair with effective chemical shifts at opposite ends of the bandwidth, i.e. with chemical shift difference of $2C_1$. Crucially, the effective coupling between these two spins was *already* reduced by the first application of (4.1). That is, the effective coupling was truncated under two sequential changes of frame. The combined effect of both reductions must be considered. In frame 0, this spin pair had $\omega_{\mathrm{I}},\ \omega_{\mathrm{S}} = 0,\ \pm C_0$, and subsequently these evolved by (2.2) to their values in frame 1 at the upper and lower limits of the bandwidth $2C_1$. Since the ratio C_0/u_0 was already set by Condition 1, the scaling of J by first application of (4.1) can be calculated to be 86.44%. Clearly, if the *second* application of (4.1) preserves at least 57.84% of the coupling, then altogether the effective coupling will stay above the 50% threshold. This is achieved by $\theta_2 - \phi_2 \leq 64°$, or, equivalently,

$$\text{Condition 2: } \frac{C_1}{u_1} \leq 0.6249$$

Once again, this necessitates placing f_2 not in the *middle* of the frame 2 bandwidth, but instead closer to one of the limits. Therefore, α_2 should be increased until the appropriate ratio of C_1/u_1 is achieved. The spin pair with $\omega_{\mathrm{I}},\ \omega_{\mathrm{S}} = 0,\ C_0$ have the same chemical shift in frames 2 and higher, and therefore suffer no more reduction in coupling strength in subsequent frames.

In principle we should continue in the same way, i.e. find the chemical shifts of the spin pair that is most reduced in frame 3, and derive the maximum allowable difference in tilt angles $\theta_3 - \phi_3$, or equivalently the maximum ratio C_2/u_2 to ensure that 50% of the coupling is preserved. However, in practice the ratio $C_{\mathrm{k}}/u_{\mathrm{k}}$ becomes extremely small after a few changes in frame (recall that the whole point of the multi-frame approach is to *reduce* C_{n} to much

	$k=0$	1	2	3	4
$u_{\rm k}/v_4$	3.5216	1.0858	0.4392	0.2281	$v_4 = 0.0575$
$f_{\rm k}$	-	3.6791	1.1497	0.4599	0.2299
$Tf_{\rm k}$	-	16	5	2	1
$C_{\rm k}/u_{\rm k}$	0.8278	0.8220	0.5825	0.2120	0.0556
$\alpha_{\rm k}$	-	0.85	0.8	0.7	0.63

Table 4.3: The amplitudes u_k and frequencies f_k in kHz for the pulse with large active bandwidth. The pulse time T =4.349 ms and the power is 4 kHz. The ratios $C_{\rm k}/u_{\rm k}$ and resonance frequency parameters $\alpha_{\rm k}$ are also given. These are relevant to the design process, as explained in the text, but only the frequencies, amplitudes, and pulse time are needed to parameterize the pulse using (2.4).

smaller than the RF power in frame n). This means that for the later frame changes, the range of tilt angles is very small and (4.1) has a negligible effect on the magnitude of the couplings. The vast bulk of the loss of coupling strength takes place in the first few frame changes.

Upper bound for active bandwidth: Condition 1 can be used to put an upper bound on the active bandwidth achievable with a multi-frame pulse. The power allocated to u_0 is strictly less than the root-mean-square power A of the pulse. Therefore, Condition 1 implies that $C_0 \leq \frac{1}{\sqrt{2}}A$. Therefore, the bandwidth in frame 0 (which is $2C_0$) cannot exceed 141% of the pulse power. This is not a very tight upper bound, since is does not take into account the power that must be allocated to subsequent fields $\{u_1,\ u_2, \dots\}$ to ensure spin-locking. Nonetheless, the pulse presented in Table 4.3 and Figure 4.10 achieves a bandwidth of 134% of the pulse power, which is 94% of the upper bound.

In practice, the design recursion equations are implemented, complete with $\alpha_{\rm k}$, to generate the field amplitudes $\{u_{\rm k}\}$. The first few $\alpha_{\rm k}$ are increased until the ratios $C_{\rm k}/u_{\rm k}$ satisfy the necessary conditions derived above. This can be done in a few moments by inspection. For practical reasons, it seems prudent to let the spin-locking bandwidth $C_{\rm k}$ grow slightly larger

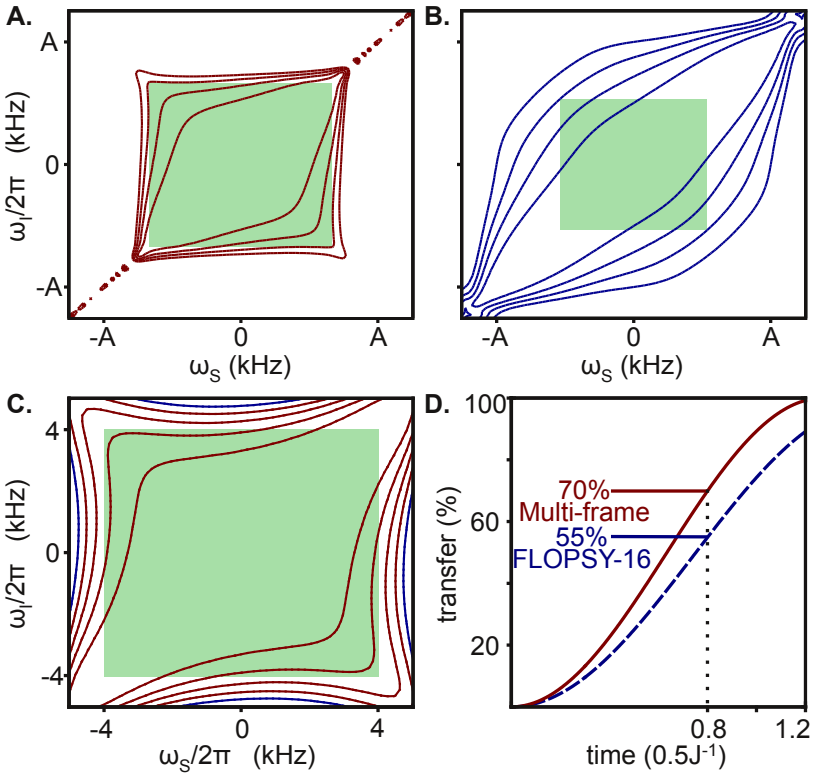

Figure 4.10: Transfer efficiency optimized for active bandwidth or quality factor. **A.** Simulation of transfer $I_y \rightarrow S_y$ under a four-frame pulse designed to maintain at least 50% of the coupling magnitude. The 50% contour line almost forms a square; no power is spent maintaining any couplings between frequencies outside of the active bandwidth. **B.** Transfer $I_z \rightarrow S_z$ with FLOPSY-16. The shaded boxes in **A.** and **B.** show the largest offset Ω for which $|\omega_I|,\ |\omega_S| \leq \Omega$ and $J_{IS}^{eff} \geq 0.5 J_{IS}$. Contour lines are at 90%, 70%, 50%, and 30% transfer, and the mixing time is $t_{mix} = (2J_{IS})^{-1}$. The maximum offset Ω is 25% larger for the four-frame pulse than for FLOPSY-16. **C.** Simulation of quality factor vs. offset under a four-frame pulse optimized for high quality factor. Contour lines are at 0.9, 0.8, 0.7,... The minimum for bandwidth ± 4 kHz (shaded box) is 0.76. **D.** Transfer from $\omega_I = +4$ kHz to $\omega_S = -4$ kHz. The minimum transfer in the interval $t \in [0.8,\ 1.2] \times (0.5J^{-1})$ for the multi-frame pulse is higher than for FLOPSY-16. The average RF power was **A.,B.** $A = 4$ kHz and **C.,D.** $A = 10$ kHz. The coupling was **A.,B.** $J = 35$ Hz and **C.,D.** $J = 10$ Hz. Relaxation and RF inhomogeneity were ignored.

than the values derived in this section, to leave room for off resonance effects near the edges of the bandwidth, for example due to RF inhomogeneity (as explained in Section 2.2). It would be a poor outcome to maintain the required coupling but fail to keep the spins in-phase near the edge of the bandwidth.

Table 4.3 shows the parameters of a pulse that achieves $J_{\mathrm{IS}}^{\mathrm{eff}} \geq 0.5J_{\mathrm{IS}}$ over a wide bandwidth. The ratios $C_{\mathrm{k}}/u_{\mathrm{k}}$ are included, and these violate the limits set above slightly, so that the spin-locking bandwidth is marginally larger that bandwidth for which $J_{\mathrm{IS}}^{\mathrm{eff}} \geq 0.5J_{\mathrm{IS}}$. The pulse is simulated in Subfigure 4.10A. FLOPSY-16 is simulated, at the same power level, in Subfigure 4.10B, and the active bandwidth is indicated for both pulses. Observe that the active bandwidth—the region with at least 50% effective coupling magnitude—is 25% larger for the multi-frame pulse than for FLOPSY-16. The square shape of the transfer efficiency profile shows that the pulse apportions its available power to ensure $J_{\mathrm{IS}}^{\mathrm{eff}} \geq 0.5J_{\mathrm{IS}}$ in a square region $|\omega_{\mathrm{I}}|,\ |\omega_{\mathrm{S}}| \leq \Omega$. The pulse does not expend any of its power allowance maintaining spin-locking along the main diagonal beyond $\pm\Omega$. To the author's knowledge, there is no other pulse available which has a larger active bandwidth[1].

Selectivity Ironically, consideration of this metric for *broadband* TOCSY pulses has led to a pulse that is highly selective for a certain range of chemical shifts, and are therefore very useful for *narrowband* TOCSY applications. The most striking feature of the pulse simulated in Subfigure 4.10A is not its high active bandwidth, but rather its sharply selective mixing profile. The utility of narrowband pulses is explored in Section 5.2.

4.4.2 Optimizing for quality factor

In this section, a relatively small bandwidth-to-RF amplitude ratio of $C_0/A = 0.8$ is nominated, and the value of J^{eff} under a multi-frame pulse for spin pairs sampled from this bandwidth is maximized. This is motivated by several studies of mixing pulses that have considered this bandwidth as part of the definition of a pulse's *quality factor*. This is used particularly in work that aims to *compare* a variety of pulses (Glaser and Quant 1996; Bai

[1]See for example the pulses cataloged in Cavanagh et al. (2007) or Glaser and Quant (1996). Scientists at NMR spectroscope manufacturer Bruker BioSpin recently chose FLOPSY-16 as the most broadband sequence available with respect to the $J^{\mathrm{eff}} \geq 0.5J$ requirement (Kovacs and Gossert 2014).

and Ramachandran 1993; Glaser and Drobny 1990).

The bandwidth is fixed to 8 kHz, i.e. $C_0 = 4$ kHz on either side of the carrier frequency. The applied power is $A = 10$ kHz, and the intrinsic coupling is $J = 10$ Hz. This situation is obviously modeled on proton TOCSY, rather than carbon TOCSY, which is why the parameters are quite different to what has been used elsewhere in this thesis. For example, compared to carbon, the proton channel can usually handle higher RF power, the J couplings are small, and the chemical shift bandwidth is narrow (Cavanagh et al. 2007).

Glaser and Drobny (1990) define the quality factor in the following way. For any pair of spins sampled from the bandwidth, calculate the *local* quality factor q: the minimum transfered magnetization in the interval $T \in [\frac{0.8}{2J},\ \frac{1.2}{2J}]$. For example, for initial condition $\rho(0) = I_\mathrm{x}$, the transfer $\langle S_\mathrm{x}\rangle(t) = 2\,\mathrm{tr}(S_\mathrm{x}\rho(t))$ is calculated for all times between 80% and 120% of the nominal mixing time $t^* = \frac{1}{2J}$, and the local quality is the minimum of this transfer (normalized by $\frac{1}{\sin^2(0.4\pi)}$ so that the maximum local quality factor is one). The *global* quality factor Q of the pulse sequence is the lowest local quality factor for any two spins in the bandwidth. The quality factor can be calculated separately for each of the x, y and z components of magnetization transfer.

For as isotropic effective coupling, and assuming that $J^\mathrm{eff} \leq J$, (1.1) shows that the local quality factor is

$$\begin{aligned} q_\mathrm{y} &= \frac{\sin^2(J^\mathrm{eff}\pi\frac{0.8}{2J})}{\sin^2(0.4\pi)} \\ &\approx C(J^\mathrm{eff})^2 \end{aligned}$$

where C is a constant, and the approximation is found by a Taylor expansion of q_y when the argument of the numerator is near $\frac{\pi}{2}$. Clearly, to maximize the global quality factor Q_y it is necessary to ensure that the smallest $J^\mathrm{eff}_\mathrm{IS}$ is as large as possible for spin pairs $(\omega_\mathrm{I},\ \omega_\mathrm{S})$ sampled from the bandwidth.

As in the previous section, the first step is to find the minimum effective coupling strength in the first frame. This occurs for spins from opposite ends of the bandwidth, $\omega_{\mathrm{I}},\ \omega_{\mathrm{S}} = C_0,\ -C_0$. The coupling is scaled down by

$$s(C_0,\ -C_0) = \frac{3}{4}\cos(\theta_1 - \phi_1) + \frac{1}{4}$$

where θ_1 and ϕ_1 are the tilt angles corresponding to opposite ends of the frame 0 bandwidth, and s is the ratio of effective to intrinsic coupling magnitude. The parameter s is called the scaling factor (Glaser and Quant 1996), and it is dependent on chemical shift offset. After the first frame change, these two spins have the same effective chemical shift and no further reduction in coupling strength occurs.

The greatest reduction of coupling strength for the second rotating-frame construction is for spins at $\pm C_1$, which had intrinsic shifts $\omega_{\mathrm{I}},\ \omega_{\mathrm{S}} = 0,\ \pm C_0$.

$$s(0,\ \pm C_0) = \left(\frac{3\cos(\theta_1 - \phi_1)}{4} + \frac{1}{4}\right)\left(\frac{3\cos(\theta_2 - \phi_2)}{4} + \frac{1}{4}\right)$$

where θ_2 and ϕ_2 are the tilt angles from opposite ends of the frame 1 bandwidth, and θ_1 and ϕ_1 are the tilt angles for $\omega_{\mathrm{I}},\ \omega_{\mathrm{S}} = 0,\ \pm C_0$.

It is clear that the most judicious choice of parameters brings about $s(0,\ \pm C_0) = s(C_0,\ -C_0)$. That is, the two spin pairs considered should have *the same* effective coupling, because only the *minimum* effective coupling determines the global quality factor. If the two effective couplings were unequal, than we could improve the quality factor by increasing one effective coupling at the expense of the other. Of course, we have only considered two spin-pairs from the entire bandwidth, so we have only derived a necessary (not a sufficient) condition to maximize the quality factor. Nonetheless, the practical pulse design was guided by this condition.

	$k=0$	1	2	3
$u_{\rm k}/v_3$	9.2836	2.3457	0.7899	$v_3 = 0.1984$
$f_{\rm k}$	-	9.5209	2.3802	0.7934
$Tf_{\rm k}$	-	12	3	1
$C_{\rm k}\ /u_{\rm k}$	0.5082	0.3806	0.1642	0.0357
$\alpha_{\rm k}$	0.79	0.79	0.67	0.67

Table 4.4: Pulse amplitudes and frequencies (in kHz) for the high quality factor pulse simulated in Subfigure 4.10C. The pulse time is $T = 1.260$ ms. The RF power is 10 kHz. The pulse is completely parametrized by the amplitudes and frequencies listed in the top two rows via (2.4); the other listed details are relevant to design process, as discussed in the text.

Upper bound for quality factor: At this point we can calculate an upper bound for the quality factor achievable with a multi-frame pulse. Suppose that all the available RF power was assigned to u_0, so that $u_0 = 10$ kHz. Of course, this is not possible; some power needs to used in subsequent frames to ensure bandwidth-reduction and spin-locking. Nonetheless, for $C_0 = 4$ kHz the tilt angles must obey $\cos(\theta_1 - \phi_1) \leq 0.7241$, so that $s(C_0, \ -C_0) = 0.7931$. That is, about 79% of the coupling can be maintained at the extremes of the bandwidth, and the local quality factor is

$$\begin{aligned} q_{\rm y} &= \frac{\sin^2(0.7931 J\pi \frac{0.8}{2J})}{\sin^2(0.4\pi)} \\ &= 0.779 \end{aligned}$$

Therefore, we cannot hope to achieve a better *global* quality factor than $Q_{\rm y} = 0.779$.

Table 4.4 gives the parameters for a pulse designed to have high quality factor. The pulse was designed by manipulating the values of $\alpha_{\rm k}$ to decrease the ratios $C_{\rm k}\ /u_{\rm k}$. In effect, this loads most of the available power into u_0, and allocates just enough power to $u_1,\ u_2$, and v_3 to ensure effective spin-locking. In practice, the $\alpha_{\rm k}$ were iteratively adjusted until transfer rates were approximately equal for $\omega_{\rm S} \in [0,\ 4]$ kHz, with $\omega_{\rm I} = -4$ kHz. This ensured that

the effective coupling, and therefore the local quality factor, was equal around the edges of the bandwidth of interest.

The offset dependence of the local quality factor is presented in Subfigure 4.10C. For transfer $I_{\mathrm{y}} \rightarrow S_{\mathrm{y}}$, the lowest transfered magnetization in time $0.4/J_{\mathrm{IS}}$ occurs at chemical shifts 1.6 kHz and -4 kHz. The transfer is 0.688, which equates to a global quality factor of 0.76. For comparison, the global quality factor for FLOPSY-16 is 0.62. Note that at various points where one of the spins resonates near $\pm$ 4 kHz, the transfer is very close to the minimum; the 80% contour line closely follows the edges of the bandwidth of interest.

At the nominal RF power level, this pulse transfers x and z magnetization. For transfers $I_{\mathrm{z}} \rightarrow S_{\mathrm{z}}$ and $I_{\mathrm{x}} \rightarrow S_{\mathrm{x}}$ the lowest transfer efficiency is at the extreme anti-diagonal position, i.e. chemical shifts 4 kHz and -4 kHz. The transfer is 0.48, which corresponds to a quality factor of 0.53. However, in the presence of RF inhomogeneity this transfer is severely reduced. As usual for multi-frame pulses, the transfer $I_{\mathrm{y}} \rightarrow S_{\mathrm{y}}$ is robust to reasonable RF inhomogeneity.

To the author's knowledge, there is no other mixing pulse which has a larger global quality factor. Certainly, the pulse given in Table 4.4 has higher quality factor than standard pulses listed by Glaser and Quant (1996) or Cavanagh et al. (2007).

4.5 Summary

In this chapter, the effect of multi-frame pulses on the J-coupling Hamiltonian was calculated. This, along with the analysis of spin-locking from Chapter 2, allowed for broadband homonuclear mixing pulses to be designed.

Three example pulses were tested in simulation and experiment. The best of these, NF4, has a considerably larger working bandwidth than FLOPSY-16. This suggests that it is highly suitable for mixing experiments, especially when the available RF power is limited. This will be particularly useful for emerging applications at high Zeeman field or with long

mixing duration.

Relaxation processes were accounted for using the method of invariant trajectories. Under a multi-frame pulse, the time-averaged projection of the magnetization vector onto each of the three axes of the Bloch sphere is approximately equal. This means that the nuclei are subject to around 2/3 of their transverse relaxation rate, plus 1/3 of their longitudinal relaxation rate. This is very similar to other TOCSY pulse sequences. Cross relaxation effects are not as pronounced as autorelaxation during TOCSY mixing periods. Nonetheless, the transverse and longitudinal cross relaxation profiles was also assessed for multi-frame pulses. The effective cross relaxation rate are less symmetrical than under FLOPSY-16 (see Figure 4.9), but they are not significantly larger.

Two standard metrics exist for the performance of TOCSY pulses: active bandwidth and quality factor. These are more suited to to experiments on the proton channel than the carbon channel. It was demonstrated that the multi-frame method can be adapted to respect either measure. Simulations suggest that the active bandwidth and quality factor achievable with multi-frame pulses surpass what has been achieved by any known pulses, including computer-optimized pulses.

In the next chapter, the repeated rotating frame design method is extended to pulses that are narrowband (i.e. selective) or multi-band, to suit particular applications in protein spectroscopy. It is also shown than by sequentially applying pulses with different chemical shift dependencies, a range of novel patterns of correlation can be generated.

5

Multi-band, narrowband, and temporal mixing

In protein NMR spectroscopy, mixing pulses which cover large bandwidths of chemical shift frequencies are usually preferred (Glaser and Quant 1996). However, there are also situations in which it is preferable to use pulses that are selective for one or more specific spectral regions (Carlomagno et al. 1996; Zuiderweg et al. 1996). These can be used to save RF power, by neglecting unpopulated frequency bands, or to manipulate the spin network by excluding certain resonances from the TOCSY experiment.

The design of multi-band-selective pulses is straightforward using the multi-frame methodology, as discussed earlier in Section 2.4. In Section 5.1 these ideas are applied to coupled

spin systems, and a variety of pulses are developed to correlate widely separated resonances at acceptably low power RF levels. Several of these pulses have been demonstrated experimentally. In contrast to existing dual-band mixing pulses, multi-frame pulses allow for closely spaced bands, asymmetric offset dependence (i.e. the active bands can have different bandwidths), and more than two bands. This versatility can be used to tailor the pulse to specific applications.

Highly selective narrowband pulses are useful for resolving particular patterns of correlation. For example, the alpha carbons in a protein fall in a narrow spectral width (about 25 ppm, which corresponds to 3 kHz on a 500 MHz spectrometer). These nuclei are strongly coupled to other carbon spins in the same amino acid ($J \approx 35$ Hz), and very weakly coupled to each other ($J \approx 2$ Hz). Therefore, in a broadband mixing experiment, the strong intra-residue couplings dominate the Hamiltonian and the weak inter-residue cross peaks are not observed. However, in this chapter it is demonstrated that using a narrowband pulse designed with multiple rotating frames the carbon alphas can be selectively mixed. The strong couplings are excluded from the average Hamiltonian so that the weak couplings can evolve. This allows for inter-residue correlations to be observed. Narrowband pulse design is discussed in Section 5.2.

Section 5.3 introduces temporally orchestrated mixing pulses. These are pulses which resolve one set of couplings for part of the mixing time, and another set of couplings during another part of the mixing time. In other words, the effective J-couplings are made to vary in time. This allows for high mixing efficiency for certain transfers, beyond what can be achieved with time-invariant couplings strengths. This approach can be used to, for example, generate multiple correlations between neighboring amino acids (Subsection 5.3.1), or rapidly assign the aromatic carbons in phenylalanine (Subsection 5.3.2). In Subsection 5.3.3 time-varying J-couplings can also be used to increase the transfer efficiency from methyl carbons to carbon alphas in ILV (isoleucine; leucine; valine) systems, which are particularly

	$k=0$	1	2	3	4
u_k/v_4	0	1.8167	1.2573	0.3365	$v_4 = 0.1246$
f_k	-	8.5469	2.8490	1.4245	0.3561
Tf_k	-	24	8	4	1

Table 5.1: The amplitudes u_k and frequencies f_k in kHz for the dual-band pulse that correlates aliphatic and carbonyl resonances. The pulse time T =2.808 ms and the power is 3.75 kHz. The dual-band behavior is generated by setting $u_0 = 0$, and the bands are widely separated by the large modulation frequency f_1. Note that the separation of the bands can be precisely controlled by adjusting f_1. For example, $f_1T = 23$ moves the bands slightly closer together; $f_1T = 25$ moves them further apart. For a carrier frequency of 105 ppm, the bands cover the aliphatic and carbonyl regions of the spectrum.

relevant for NMR spectroscopy of large proteins.

5.1 Multi-band mixing

Simple pulse design for dual-band and tri-band spin-locking was described in Section 2.4, along with slightly more complicated procedures that relied on manipulation of the Fourier components of broadband multi-frame pulses. In this section, the J-couplings for spin pairs between and within the bands are analyzed. This leads to a variety of band-selective mixing pulses which have been tested in simulations and experiments.

5.1.1 Dual-band mixing

In this subsection the problem of designing a dual-band pulse for either aliphatic-aromatic or aliphatic-carbonyl mixing is addressed. Firstly, recall from Section 4.1 that a dual-band pulse preserves at best 50% of the coupling strength between spins sampled from different bands. This is seen by noting that when $u_0 = 0$, the tilt angles are $\theta_1 = 0$ for spins from one band, and $\phi_1 = \pi$ for spins from the other band. Under (4.1), the planar part of the coupling is eliminated ($b_1 = 0$) and the longitudinal part is fully maintained ($a_1 = a_0 = 2\pi J_{\rm IS}$). The average magnitude of the coupling in frame 1 is $\frac{1}{2}(a_0+b_0) = \pi J_{\rm IS}$, i.e. the effective magnitude

is half of the intrinsic magnitude. Further frame changes will result in additional applications of (4.1), and therefore produce further truncation of the effective coupling strength.

As noted in Section 2.4, the bands can be moved arbitrarily far apart without using any extra RF power or time. This means that is straightforward to cover, for example, the widely separated aliphatic carbons (5–75 ppm) and carbonyl (165–185 ppm) bands, while excluding the large region in between. This region is mostly unpopulated, but does contain the aromatic carbon resonances (110–140 ppm), which will not be included in the TOCSY transfer. Alternatively, the down-field band can be placed over the aromatics, and the carbonyl nuclei excluded.

Table 5.1 gives the parameters for a pulse which mixes between the aliphatic and carbonyl bands. The RF power is 3.75 kHz, and the duration is $T = 2.808$ ms. Figure 5.1 shows the effective chemical shift, calculated using (2.2), that is produced by the pulse. Clearly, the bandwidth is reduced to near zero in two separate spectral regions, which have been placed over the required parts of the carbon spectrum. The large effective shifts that occur in between these two bands ensure that the Hartmann-Hahn mixing condition cannot be satisfied between the bands; the effective chemical shifts are up to several kilohertz, while the intrinsic couplings in protein samples are much smaller—on the order of tens of Hertz. However, the Hartmann-Hahn condition *is* satisfied for spin pairs sampled from the two mixing bands, including the case where one chemical shift frequency is sampled from each band.

Figure 5.1 also contains a spectrum of the pentapeptide sample that was recorded using the dual-band pulse. Cross peaks are observed amongst aliphatic spins (15–65 ppm), and between the aliphatic and carbonyl spins (the latter are near 175 ppm). Each carbonyl nucleus is directly bonded to only to its local carbon alpha (45–65 ppm). This means that several of the visible aliphatic-carbonyl cross peaks were generated by magnetization which

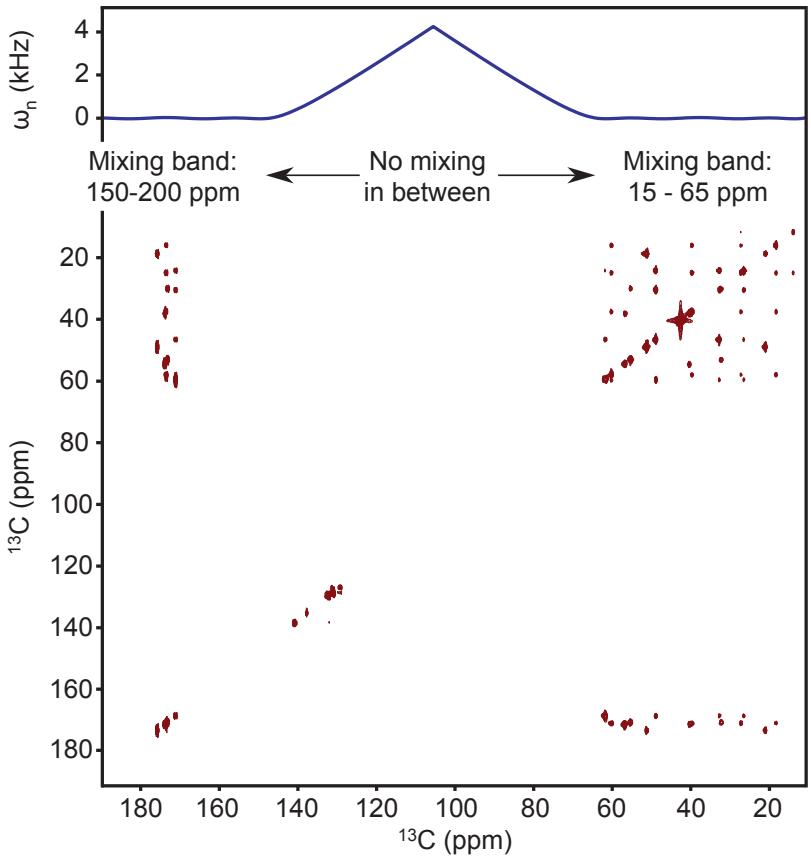

Figure 5.1: A dual-band mixing pulse is tested experimentally with the PIFHA peptide. The carrier frequency is 105 ppm so that the two bands fall over the aliphatic and carbonyl regions of the carbon spectrum. The solid line shows the effective chemical shift in the n^{th} frame calculated using (2.2). The mixing time is $20T \approx 56$ ms. The average RF amplitude is 3.75 kHz, while the bandwidth is 2×6.25 kHz with a 10.7 kHz gap. Cross peaks are observed between and within the carbonyl and aliphatic spectral regions.

has moved through more than one aliphatic spin, as well as across the alpha-carbonyl bond, all during the mixing period. The aromatic resonances are visible along the main diagonal (around 130 ppm); however, these are effectively decoupled from the other spins, so there are no cross peaks linking the aromatics with the other populated regions. In Figure 5.2, the same pulse is applied to a protein sample.

The most broadband mixing pulse available, NF4, which was described in Subsection 4.2.3, would require an RF power level of approximately 10 kHz to cover the same bandwidth as the

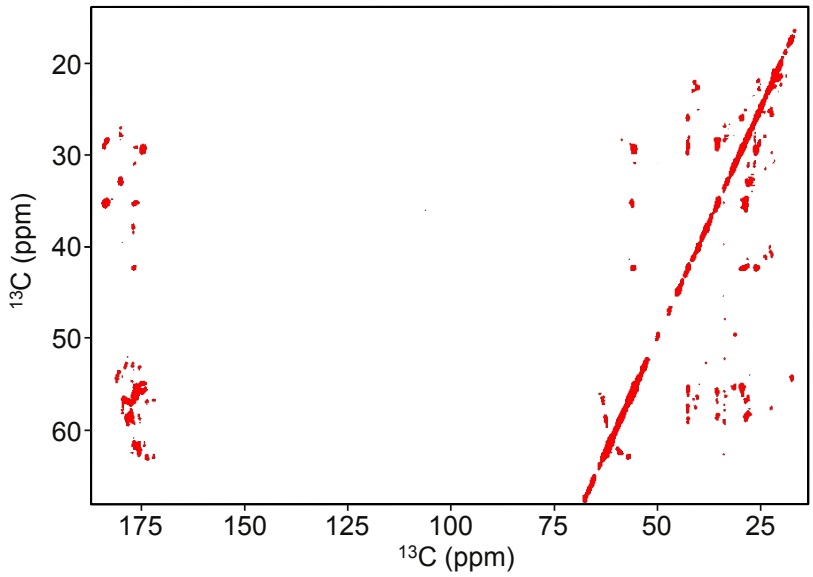

Figure 5.2: A 3.75 kHz multi-frame dual-band mixing pulse is used for dual-band TOCSY of a protein sample, BCL-X_L. The pulse was designed using four rotating frames. The same pulse was used for Figure 5.1.

dual band pulse. Therefore, the dual-band pulse, using only 3.75 kHz power, is an attractive option for generating correlations between widely separated bands of resonances.

Asymmetric bandwidths: In Section 2.4, a dual-band spin-locking pulse was designed in which the two bands were different widths. This is a more comfortable fit for the carbon spectrum than pulses with two equal bandwidths; the main spectral regions of interest for carbon are not all equally wide. In particular, the pulse parameterized in Table 2.4 is tailored to the wide aliphatic and narrow carbonyl bands. This is clear from the spin-locking profile shown in Subfigure 2.7F. Note that currently available dual-band homonuclear mixing pulses all have equal bandwidths. However, independent control over the two bandwidths, to allow a precise fit to the correct parts of the spectrum, is facilitated by the repeated rotating frames design method.

Figure 5.3 shows the transfer efficiency for this pulse. There can be no mixing to the non-spin-locked frequencies, so only the mixing with the wide band (Subfigure 5.3A) and

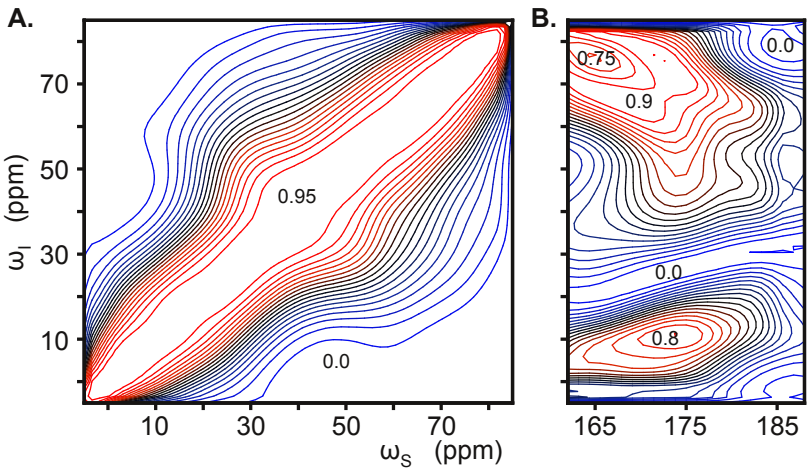

Figure 5.3: Transfer efficiency for the dual-band aliphatic-carbonyl pulse with asymmetric bandwidths. **A.** High transfer efficiency is achieved within the aliphatic region. **B.** Good transfer occurs between the carbon alpha range (45–65 ppm) and the carbonyl range (170–180 ppm). For both subplots, the coupling strength is $J = 35$ Hz. The mixing time is $t_{\text{mix}} = (2J)^{-1}$ (within-band mixing) and $t_{\text{mix}} = J^{-1}$ (between-band mixing). The pulse parameters are given in Table 2.4, and the spin locking profile is given in Subfigure 2.7F.

between the two bands (Subfigure 5.3B) are shown. The couplings within the wide aliphatic region are strongly maintained. The bandwidth along the main diagonal is around 85 ppm. The couplings are maintained over a reasonably wide region off the main diagonal too. The coupling between the two bands (Subfigure 5.3B) has a null at around 20–30 ppm. This will not ruin the performance, since the couplings in protein samples occur between the carbon alpha range (45–65 ppm) and the carbonyl range (170–180 ppm).

The dual-band pulse with asymmetric bands has not yet been demonstrated experimentally.

5.1.2 Tri-band mixing

During the last two decades, several dual-band mixing pulses have been designed for liquid state and solid state NMR, especially for homonuclear cross-polarization experiments on the carbon channel (Grzesiek and Bax 1995; Carlomagno et al. 1996; Zuiderweg et al. 1996;

	$k=0$	1	2	3	4	5
$u_{\rm k}/v_5$	2.1444	2.0478	0.9444	-1.1785	0.6824	$v_5 = 0.1750$
$f_{\rm k}$	-	11.1985	5.5993	2.7996	1.3998	0.6999
$Tf_{\rm k}$	-	16	8	4	2	1

Table 5.2: The amplitudes u_k and frequencies f_k in kHz for the tri-band mixing pulse. The pulse time is T =1.429 ms and the power is 6 kHz. The frequencies, amplitudes, and pulse time parameterize the pulse by (2.4). The carrier frequency must be set 118 ppm for placement of the bands over the appropriate parts of the carbon spectrum.

Demers et al. 2010; Zhang et al. 2012). However, the carbon spectrum of protein samples most naturally divides into *three* bands. The aliphatic carbons occupy the spectral region 0–80 ppm, the aromatics typically fall within the range 110–140 ppm, and the carbonyl resonances are at 170–180 ppm. Tri-band pulses suitable for correlating spins within and between these three separated spectral regions have not yet been developed. However, in Section 2.4 it was demonstrated that using the repeated rotating frame method, multi-band spin-locking pulses can be produced in a straightforward manner. The procedure is to begin with a broadband pulse, designed by applying the coupled recursions (2.10) and (2.11), and then reduce one or more of the the amplitudes $\{u_{\rm k}\}$ to produce multiple spin-locking bands with the appropriate spacing of active bands and gaps.

In this subsection, a pulse designed by this method is used for TOCSY mixing amongst spins sampled from three spin-lock bands. The pulse was designed with five rotating frames. The amplitude u_2 was reduced to 56% of its value, which induces a five-band structure: the two outermost bands are very narrow, while the three innermost bands are wide and relatively closely spaced. With a careful choice of overall RF power level and carrier frequency, the three central bands can be aligned with the aliphatic, aromatic, and carbonyl regions, as required.

At this stage, the mixing performance was observed using simulations of coupled two-

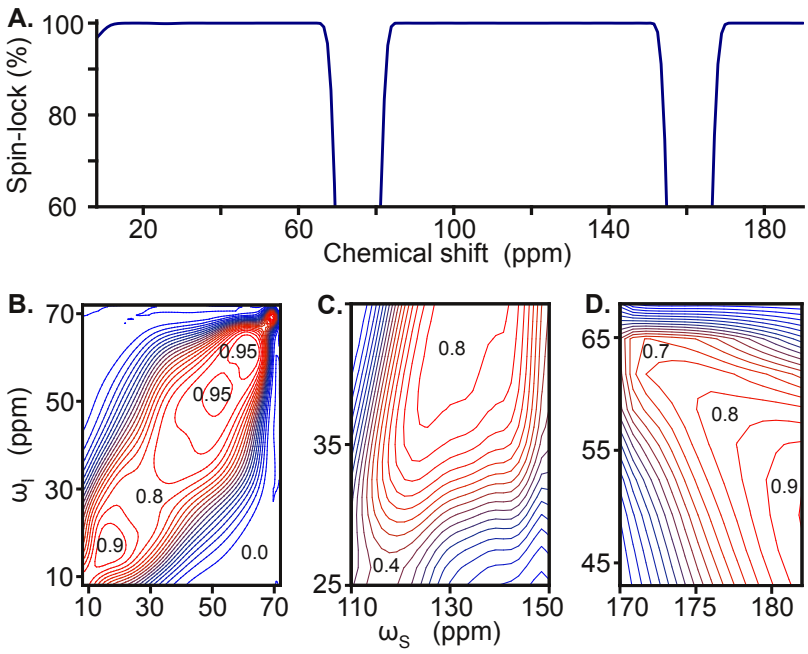

Figure 5.4: Simulations of spin-locking and transfer efficiency for the tri-band TOCSY pulse. The pulse parameteres are listed in Table 5.2. The root-mean-square RF amplitude is 6 kHz. The carrier frequency is 118 ppm. **A.** Spin-locking about the y-axis for time $4T$, where T =1.429 ms is the period of the pulse. Clearly, the spins are kept in-phase in three separate, closely spaced parts of the spectrum. **B.** Transfer efficiency within the aliphatic band. The coupling is J =35 Hz and the mixing time is $t_{\text{mix}} = (2J)^{-1}$. **C.** Transfer efficiency between the carbon beta and carbon gamma regions. J =40 Hz and the mixing time is $t_{\text{mix}} = 2J^{-1}$, i.e. four times longer than for spin pairs that maintain their full intrinsic coupling. **D.** Transfer efficiency between the carbon alpha and carbonyl regions. J =55 Hz and the mixing time is $t_{\text{mix}} = 2J^{-1}$.

spin systems with varying chemical shift offset frequencies. Further minor adjustments were made to the pulse amplitudes in an ad hoc fashion. The idea was to attempt to produce improved transfer efficiency by varying some of the pulse amplitudes and observing the effect on the transfer efficiency plots. The amplitudes u_0 was reduced by 7% and the amplitude u_0 was reduced by 1%. These changes slightly moved the high-efficiency parts of the mixing performance to achieve a better match with with the alpha-carbonyl couplings. Furthermore, the sign of u_3 was reversed, which increased the efficiency of transfers between carbon beta and the aromatic region.

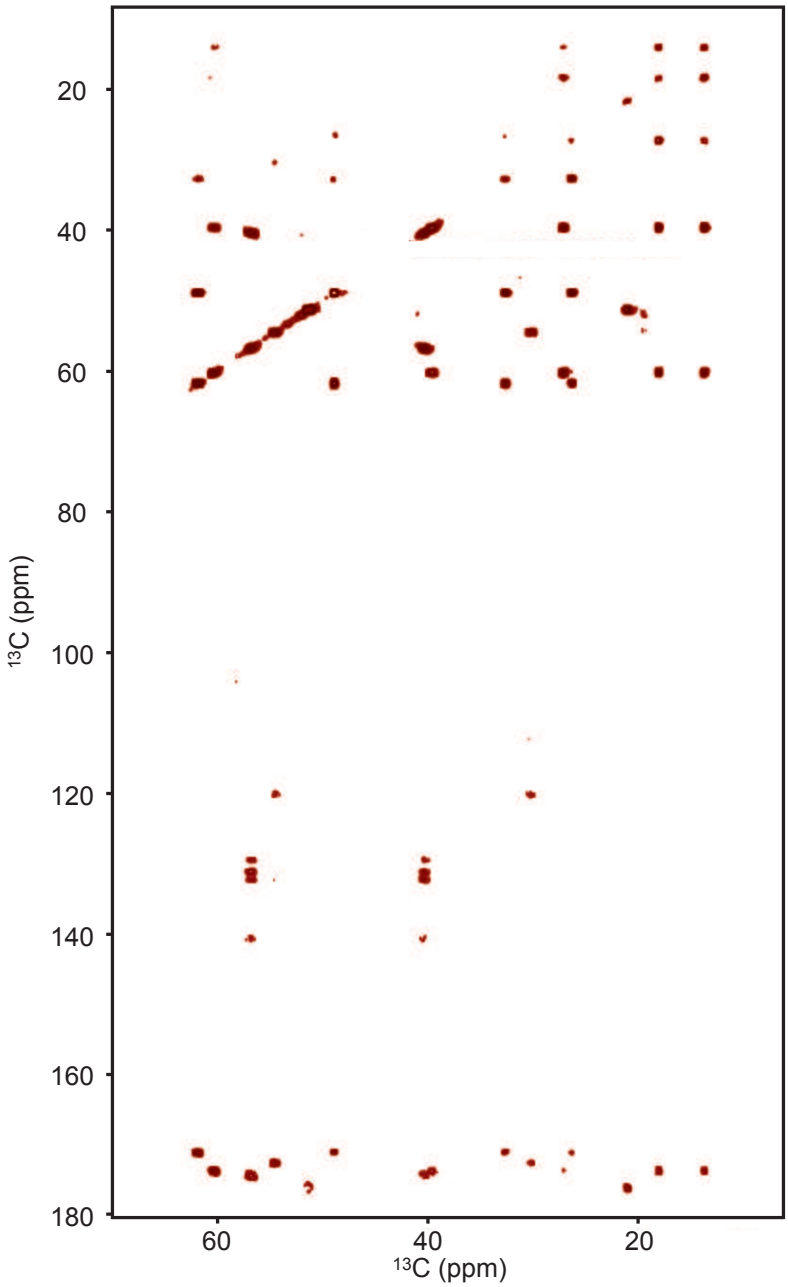

Figure 5.5: The tri-band mixing pulse is applied to the pentapeptide sample. This pulse has three active mixing bands, placed over the aliphatic, aromatic, and carbonyl regions. The root-mean-square RF amplitude is 6 kHz, and the mixing time is 77.15 ms. Cross peaks are observed between all three bands; however, some aromatic cross peaks are missing and the upper left part of the spectrum is of poor quality.

The simulated mixing performance between the spectral regions of interest, as well as the tri-band spin-locking profile, are depicted in Figure 5.4. These simulations are of the final pulse, i.e. they include the ad hoc adjustments described above. Subfigure 5.4A shows the magnetization that returns to the y-axis after time $4T$ (four repetitions of the pulse). Clearly, the three bands of interest are spin-locked, and there are narrow gaps between the bands. These gaps occur in unpopulated spectral areas. Subfigure 5.4B shows mixing amongst the aliphatic carbons. The mixing is sufficiently broad to correlate spins over the entire aliphatic bandwidth. The coupling was set to $J = 35$ Hz, and the mixing time was $t_{\text{mix}} = (2J)^{-1}$.

Subfigures 5.4C and 5.4D show the mixing between carbon beta and the aromatics, and carbon alpha and carbonyl, respectively. For between-band mixing with more than two bands, the coupling tensor has been reduced by successive applications of (4.1). Therefore, a longer mixing time than usual is required to allow magnetization to move along the weakened couplings. These plots have mixing time $t_{\text{mix}} = 2J^{-1}$, with characteristic couplings of 40 Hz (beta-aromatic) and 55 Hz (alpha-carbonyl), respectively. Clearly, sufficient coupling strength is maintained by the pulse for the three kinds of transfers tested in Subfigures 5.4B–D, which are the couplings typically present in protein samples.

The pulse parameters are given in Table 5.2. These values include the ad hoc adjustments made to the pulse amplitudes, described above. The root-mean-square RF amplitude of the pulse is 6 kHz—sufficiently low to run the pulse safely for reasonable mixing times. By contrast, around three times as much RF power is required to cover the carbon spectrum with a single broadband pulse (Kovacs and Gossert 2014).

An experimental test of the tri-band pulse was carried out on the pentapeptide sample, and the spectrum is presented in Figure 5.5. The mixing time was 77.15 ms. Aliphatic-aromatic cross peaks have been produced for both histidine and phenylalanine. However, more cross peaks were expected in the case of histidine: an aromatic at 120 ppm has clearly been correlated with the histidine alpha and beta nuclei, but similar correlations are not

observed for the other histidine aromatics. Cross peaks between the aliphatic and carbonyl regions are well resolved. The top left corner of the aliphatic regions appears to have low-intensity and missing peaks. The reason for this imperfection is unclear. These shortcomings notwithstanding, tri-band mixing has been demonstrated using a multi-frame mixing pulse. However, further improvements to the pulse are required if this technique is to be of practical benefit in protein NMR.

5.2 Narrowband mixing

Typically, TOCSY pulses are designed to function over a range of chemical shift frequencies that is as broad as possible (Glaser and Quant 1996). This is so that many bonds between neighboring nuclei can be observed. However, there are applications in protein NMR in which it is desirable to mix magnetization amongst spins in a particular narrow spectral range, and exclude any resonances that are outside of this range.

For example, the recently-developed CACA-TOCSY experiment requires that magnetization be moved across weak J-couplings that exist between the carbon alphas of neighboring amino acids, without magnetization moving to the strongly-coupled carbon betas (Takeuchi et al. 2010). The required selectively can be achieved chemically, by creation of a sample in which the alphas are carbon-13, while the other aliphatic carbons are carbon-12, which is spin-0 and therefore not NMR-active. This is called *alternate labeling*.

However, selection of the alpha carbons can also be realized using specially designed narrowband mixing pulses, i.e. pulses that are selective for a narrow range of chemical shift frequencies. Carbon alphas reliably resonate in a specific spectral region, from about 45 ppm to 65 ppm. The other aliphatics have resonance frequencies that are, with a few exceptions, outside of this region (Ulrich et al. 2008). If the mixing pulse has sufficiently sharp cutoffs at the edges of its bandwidth, then it can be used to mix magnetization between carbon

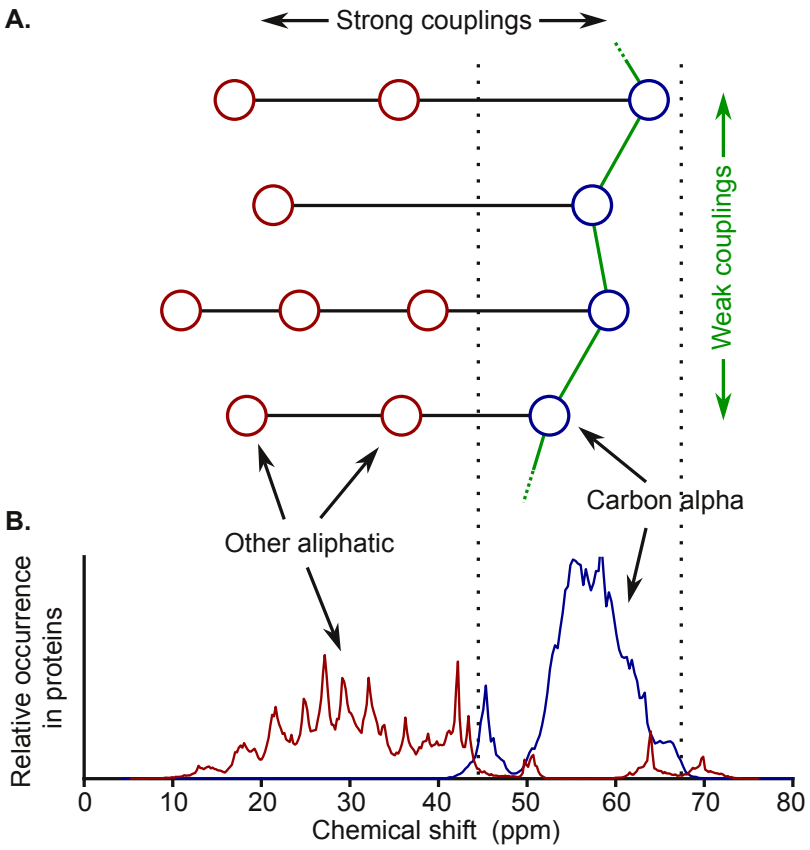

Figure 5.6: CACA-TOCSY by chemical shift selectivity. **A.** The spin system is a chain of carbon alphas, which are linked by weak inter-residue couplings ($\sim$ 2 Hz). Each carbon alpha is strongly coupled to the other aliphatic nuclei in the same residue. The intra-residue couplings are $\sim$ 35 Hz. Crucially, in the presence of strong couplings, the weaker couplings do not transfer magnetization efficiently, and inter-residue cross peaks are typically not observed in broadband TOCSY experiments. **B.** Around 560k protein chemical shift values from the Biological Magnetic Resonance Data Bank (Ulrich et al. 2008) were sorted into two categories: carbon alphas and other aliphatic carbons. The normalized histograms of these two sets are plotted here. The alpha chemical shifts occur mostly in the region 45–65 ppm. while the other spins mostly resonate outside of this region. The raises the possibility of performing CACA-TOCSY using a narrowband mixing pulse.

alphas, without any signal being transfered to the other aliphatics. Thus, the CACA-TOCSY experiment can also be used in the case of uniformly carbon-13 labeled samples, provided that narrowband mixing can be implemented. This approach has two obvious advantages: firstly, it does not require that an alternately labeled sample be synthesized. Secondly, the carbon betas can be included in, or excluded from, the TOCSY transfer at various times

during the same experiment. This can be used to generate novel spectra, and is discussed in detail in Subsection 5.3.1.

Figure 5.6 illustrates why CACA-TOCSY could be implemented using a selective narrowband mixing pulse. Subfigure 5.6A is a schematic of the coupling topology for the aliphatic region of the carbon spectrum in a protein sample, showing weak couplings between the carbon alphas of neighboring residues, as well as several strongly coupled spins within each residue. Subfigure 5.6B shows the distribution of resonance frequencies for carbon alpha nuclei versus the other aliphatic carbons, taken from the Biological Magnetic Resonance Data Bank (Ulrich et al. 2008). Clearly, there is a narrow band of frequencies which contains carbon alphas almost exclusively. Mixing that is selective for this region will allow magnetization to move along the weak inter-residue couplings, rather than along the strong intra-residue couplings.

The design of narrowband mixing pulses is straightforward using the repeated rotating frame methodology. Recall that in Subsection 4.4.1, the basic method was adapted in order to maximize the *active bandwidth*: the range of frequencies over which at least half of the intrinsic coupling was maintained by the pulse. The result, depicted in Subfigure 4.10A in Chapter 4, was a pulse that maintained a reasonably strong coupling over a certain bandwidth, but did not expend any of its RF power allowance needlessly spin-locking resonances outside of this bandwidth. Simulation revealed a strikingly sharp cutoff outside of the active bandwidth. In other words, the mixing efficiency of this pulse is highly selective for a specific spectral range. This was achieved simply by adjusting the value of α in (2.6), so that the frequencies in each new frame were no longer chosen to be in the middle of the bandwidth.

Comparison of Subfigures 4.10A and 4.10B (the latter is the active bandwidth and mixing efficiency profile of FLOPSY-16) shows that the mixing profile of the selective pulse has a different shape from the mixing profile of a broadband TOCSY sequence. Although the active bandwidths (the shaded regions in the plots) could be made equal by increasing the

	$k=0$	1	2	3
u_k/v_3	1.7942	0.4889	0.2605	$v_3 = 0.0658$
f_k	-	1.8421	0.5263	0.2632
Tf_k	-	7	2	1
α_k	-	0.87	0.6	0.55

Table 5.3: The amplitudes u_k and frequencies f_k in kHz for the narrowband (selective) mixing pulse. The pulse time is T =3.8 ms and the power is 2 kHz. The resonance frequency parameters α_k are also given. These are relevant to the design process, as explained in the text, but only the frequencies, amplitudes, and pulse time are needed to parameterize the pulse using (2.4).

RF power level of FLOPSY, the narrowband pulse would reliably *decouple* spins outside of the chosen bandwidth, whereas the broadband pulse would transfer a significant proportion of its polarization to spins that are not in the active bandwidth.

5.2.1 Narrowband pulse for CACA-TOCSY

Motivated by the high degree of selectivity observed in Subfigure 4.10A in Chapter 4, and by the spectral separation of carbon alphas from other nuclei in protein chemical shift statistics, the problem of carbon alpha TOCSY in uniformly carbon-13 labeled samples is addressed in this subsection.

In order to demonstrate CACA-TOCSY with uniformly labeled samples, a narrowband pulse was designed to maintain efficient mixing over a 20 ppm bandwidth, and, crucially, to inhibit mixing if either one of the spins is outside of this region. In practice, no selective pulse can be perfectly sharp; there is always a small transition region between the mixing band and the stop-band[1]. The pulse given in Table 5.3 has a mixing band that is approximately 20 ppm wide, and a transition region of approximately 1.5 ppm, as indicated in Subfigure 5.7A. The transition is far narrower than for broadband sequences, and sufficient to isolate

[1]This echoes the situation in selective excitation and inversion pulse design—an important topic in, for example, MRI (Bernstein et al. 2004) and NMR quantum computing (Jones 2011)—where the desired sharp excitation profile is only approximately realized.

the carbon alpha resonance in most amino acids.

The narrowband pulse is simulated extensively in Figure 5.7. The simulation in Subfigure 5.7A considers a spin at 55 ppm—the center of the carbon alpha range—that is weakly coupled to another carbon alpha. The transfer is plotted as a function of the chemical shift frequency of the second spin. The coupling strength is $J_{\mathrm{IS}} = 2.06$ Hz, so that 64 repetitions of the pulse is exactly the optimal mixing time $t_{\mathrm{mix}} = (2J_{\mathrm{IS}})^{-1}$, which is around 243 ms. Clearly, transfer is achieved over a specific bandwidth, but no mixing takes place to spins outside of the design bandwidth. 10 repetitions of the FLOPSY-16 sequence with $J_{\mathrm{IS}} = 2.12$ and $t_{\mathrm{mix}} = (2J_{\mathrm{IS}})^{-1}$ are also depicted for comparison. Subfigures 5.7B and 5.7C show the same simulation, but with the transfer beginning with a spin at 47 ppm or 63 ppm, respectively. Not only is the mixing profile more precisely fitted to the carbon alpha region than what is possible using FLOPSY-16, but the transfer efficiency is also higher across the carbon alpha region. In particular, transfer between spins from opposite ends of the carbon alpha bandwidth is considerably stronger under the selective pulse, as can be seen in Subfigures 5.7B and 5.7C. Clearly, even when the magnetization originates on a spin which is near the edge of the bandwidth, it is transfered with high efficiency right across the mixing bandwidth. In these plots, relaxation and RF inhomogeneity are ignored.

Subfigure 5.7D shows the transfer efficiency plot for the narrowband pulse. The coupling magnitude is $J_{\mathrm{IS}} = 2.06$ Hz and the mixing time is $t_{\mathrm{mix}} = (2J_{\mathrm{IS}})^{-1} = 64T$. Relaxation and RF inhomogeneity are ignored. The transfer is greater than 95% over a broad spectral width, and then rapidly drops to less than 5%. This confirms that the pulse can be used to precisely select a narrow mixing bandwidth.

Subfigure 5.7E is a simulation of CACA-TOCSY with a uniformly carbon-13 labeled four-spin-1/2 system. The spin system comprises two residues, each of which contains a strongly coupled alpha and beta carbon. The intra-residue couplings are 35 Hz. The two carbon

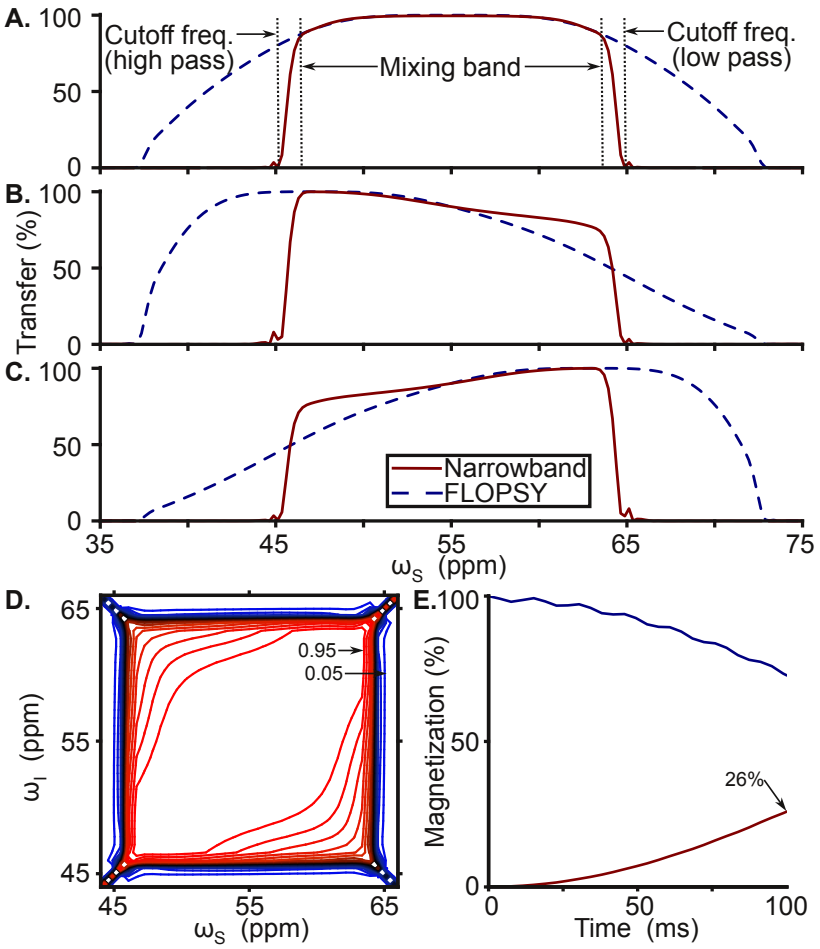

Figure 5.7: A narrowband (selective) TOCSY pulse. **A.** Simulation of transfer of magnetization from $\omega_{\mathrm{I}} = 55$ ppm, as a function of ω_{S}. The profile for FLOPSY-16 (dashed line) at the same power level is also shown. The narrowband pulse has efficient transfer over a certain bandwidth, but excludes resonances outside of this bandwidth. The transition from mixing band to decoupled band is 1.5 ppm wide. The coupling is $J_{\mathrm{IS}} = 2.06$ Hz (narrowband) and $J_{\mathrm{IS}} = 2.12$ Hz (FLOPSY). The mixing time is $t_{\mathrm{mix}} = (2J_{\mathrm{IS}})^{-1}$: 64 repetitions of the narrowband pulse and 10 repetitions of FLOPSY-16. Relaxation and RF inhomogeneity are ignored. **B., C.** The origin spin resonants ± 1 kHz from the carrier frequency, i.e. $\omega_{\mathrm{I}} = 47$ ppm (B) and $\omega_{\mathrm{I}} = 63$ ppm (C). **D.** The transfer efficiency plot for the narrowband pulse. The coupling is $J_{\mathrm{IS}} = 2.06$ Hz and the mixing time is $t_{\mathrm{mix}} = (2J_{\mathrm{IS}})^{-1}$. Relaxation and RF inhomogeneity are ignored. Contour lines are at $0.95, 0.9, \ldots 0.05$. **E.** Simulation of CACA-TOCSY. $J = 2$ Hz and $t_{\mathrm{mix}} = 100$ ms. The carbon alphas are at 50 ppm (origin spin) and 60 ppm (destination spin). Each carbon alpha is strongly ($J = 35$ Hz) coupled to a local carbon beta at 35 ppm, so that there are four spins altogether. Relaxation is ignored. RF inhomogeneity is averaged over 20 values uniformly distributed between 0.9 and 1.1. The transfer is 26%. There is no transfer to either carbon beta.

alphas are also weakly coupled to each other: this *inter*-residue coupling is only 2 Hz. Both carbon betas have a chemical shift of 35 ppm. The carbon alphas have chemical shifts of 50 ppm and 60 ppm, respectively. The initial state is $\rho(0) = I_{\mathrm{y}}^{\alpha_1}$. That is, y-phase magnetization is present on one of the carbon alphas at the beginning of the simulation. The mixing pulse runs for 100 ms, and no signal is transfered to either carbon beta. However, up to 26% of the in-phase magnetization migrates across the weak coupling to the second alpha carbon. This simulation includes RF inhomogeneity that is uniformly distributed between ±10% of the nominal power level.

This pulse has not been tested individually in an experiment. Nonetheless, it has been demonstrated to function correctly in an experimental situation: it is a crucial part of a more intricate experiment described and tested below in Subsection 5.3.1. This novel experiment would not be possible without a highly selective narrowband TOCSY pulse.

5.3 Temporally orchestrated mixing

Under a ideal broadband TOCSY mixing pulse, the chemical shift offsets are effectively removed, while the J-couplings allow magnetization to move throughout the spin network. For a given TOCSY pulse and spin topology, there are a set of effective (average) J-coupling constants that characterize the rates of transfer of magnetization.

Suppose, however, that the pulse *switches* between different effective J-couplings during the mixing time. For example, one coupling evolves for a certain duration, and then it is completely switched off (decoupled) while a different coupling is resolved. Alternatively, the magnitude of certain couplings could be reduced, rather than completely removed, during certain times within the overall mixing duration. This temporal control over the strength of J-couplings can be achieved by dynamically switching between different mixing pulses during the TOCSY period.

In this section, it is demonstrated that time-varying effective J-couplings can lead to enhanced transfer efficiency between certain sets of resonances. Three examples that are highly relevant to protein spectroscopy are used to explore this idea. Firstly, broadband and narrowband mixing are combined in order to correlate aliphatic carbons with the carbon alphas of adjacent residues. In contrast to CACA-TOCSY, inter-residue cross peaks involving spins *other than* carbon alpha can be observed using this technique. Secondly, a temporally orchestrated scheme for correlating alpha and beta carbons with aromatic nuclei in phenylalanine is developed, using a combination of two different dual-band pulses. Finally, time-varying effective couplings are suggested as a way of maximizing transfer between methyl group carbons and their local carbon alphas. This particular transfer is vital to the assignment of large proteins (Otten et al. 2010; Venditti et al. 2011).

5.3.1 Correlation of sidechain carbons via caca couplings

In Subsection 5.2.1 a narrowband selective pulse was presented. The narrowband pulse is capable of mixing magnetization amongst carbon alphas while the strong J-couplings to other aliphatic spins are effectively decoupled. This is achieved via a sharply selective mixing pulse, tailored to the carbon alpha region of the spectrum. In this subsection, the narrowband pulse is incorporated into a longer sequence in the following way: a broadband pulse is applied, followed immediately by a narrowband pulse. The broadband pulse correlates side chain carbons with their respective carbon alphas; the narrowband pulse resolves weak inter-residue couplings between neighboring alpha carbons.

Figure 5.8 presents some simulations that show why temporal control of the effective J-couplings is needed. The simulation data suggest that transfer of magnetization from a carbon beta to the carbon alpha of the neighboring residue cannot be efficient under any TOCSY pulse in which the effective couplings are time-invariant. Subfigure 5.8A shows

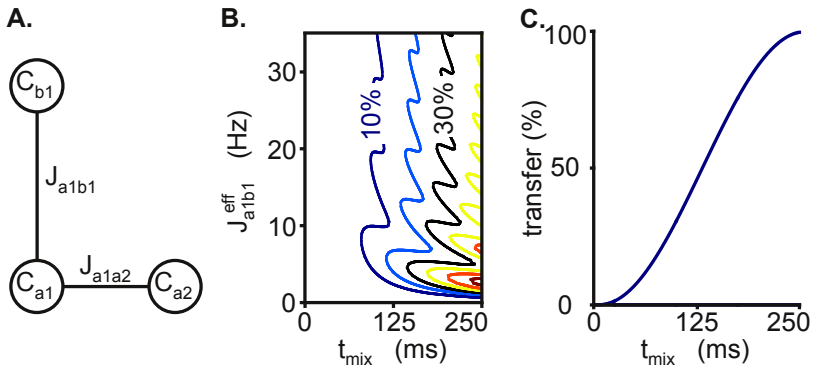

Figure 5.8: Temporally orchestrated mixing pulses can produce higher transfer efficiency than pulses with time-invariant effective J couplings. **A.** This simulation is of a residue with a strong intra-residue coupling (35 Hz) between the Ca1 and Cb1 carbons. Ca1 is weakly (J_{a1a2} = 2 Hz) coupled to Ca2 in a neighboring residue. The goal is to transfer in-phase magnetization from Cb1 to Ca2. For a given RF pulse, the couplings are replaced by *effective* couplings, so that J_{a1b1} can be lowered by choice of pulse. **B.** In-phase transfer from Cb1 to Ca2 as a function of mixing time and effective coupling, for time-invariant couplings. The maximum achievable transfer is 63% in 250 ms for J^{eff}_{a1b1} = 2.5 Hz. **C.** A simple temporal scheme produces higher transfer efficiency. The pulse maintains the full magnitude of both couplings for 14.3 ms, and afterwards effectively decouples Cb1. 99.6% of the Cb1 magnetization is transfered to Ca2. For smaller mixing times the temporal scheme's superior performance is even more pronounced. For example, at 125 ms the maximum transfer achievable with a time-invariant effective J is around 20%, where as close to 50% transfer is achieved with the simple temporal scheme.

a simple spin system with a strongly coupled CACB pair, and another (weakly coupled) CA. The polarization transfer of interest is from the CB, through its local CA, and on to the the second CA. Subfigure 5.8B is a plot of the transfer as a function of mixing time and the effective scaling of the strong coupling. Clearly, maximum efficiency is achieved when the strong coupling is *almost* eliminated, i.e. it is reduced by the pulse from 35 Hz to 2.5 Hz. The transfer is 63% in 250 ms. Of course, for realistic samples, it is unfeasible to simultaneously reduce all CACB couplings to 2.5 Hz, while fully maintaining the weak inter-residue couplings.

Subfigure 5.8C shows that a very simple scheme to produce time-varying effective J-couplings can do much better. Firstly, both couplings are fully maintained for time t =

$(2J_{\text{strong}})^{-1}$. This is easy to achieve using a broadband mixing pulse such as NF4 (described in Subsection 4.2.3) or FLOPSY-16. Secondly, the strong coupling is removed completely for the remainder of the mixing time. This can be realized using the narrowband CACA pulse derived in Subsection 5.2.1. The transfer from CB to the weakly coupled CA reaches a maximum of 99.6% in 250 ms. In practice, the mixing time in CACA-TOCSY is usually shorter than 250 ms (Takeuchi et al. 2010). After 125 ms of mixing, the best-case time-invariant scheme could achieve around 20% transfer, provided that it could be implemented with exactly the right scaling of the strong coupling. However, the simple temporally-orchestrated scheme produces close to 50% transfer in 125 ms. All of this suggests that the combination of two mixing pulses with different offset dependencies is highly suitable for generating these inter-residue cross peaks.

A schematic overview of the proposed procedure is given in Figure 5.9. The pulse sequence broadband at first, and then switches to narrowband. Subfigure 5.9A considers the effect on a component of signal which originates on a non-alpha sidechain carbon nucleus. During the broadband mixing pulse, this component of magnetization is shared with other spins in the same amino acid. In particular, some portion of the magnetization is transfered to the local carbon alpha. When the pulse is switched to narrowband, the coupled carbon alphas exchange magnetization. The combined effect of the two stages is that magnetization moves from the original sidechain carbon all the way to the carbon alphas of two adjacent residues. Subfigure 5.9B shows which features of the TOCSY spectrum are generated by each part of the pulse. The broadband pulse generates cross peaks that correlate the spins *within* each amino acid. The subsequent narrowband mixing pulse takes signal associated with carbon alphas and generates further cross peaks across weak bonds.

In contrast to the original CACA-TOCSY experiment (Takeuchi et al. 2010), this method works for uniformly labeled samples, and correlates the entire aliphatic region to neighbor-

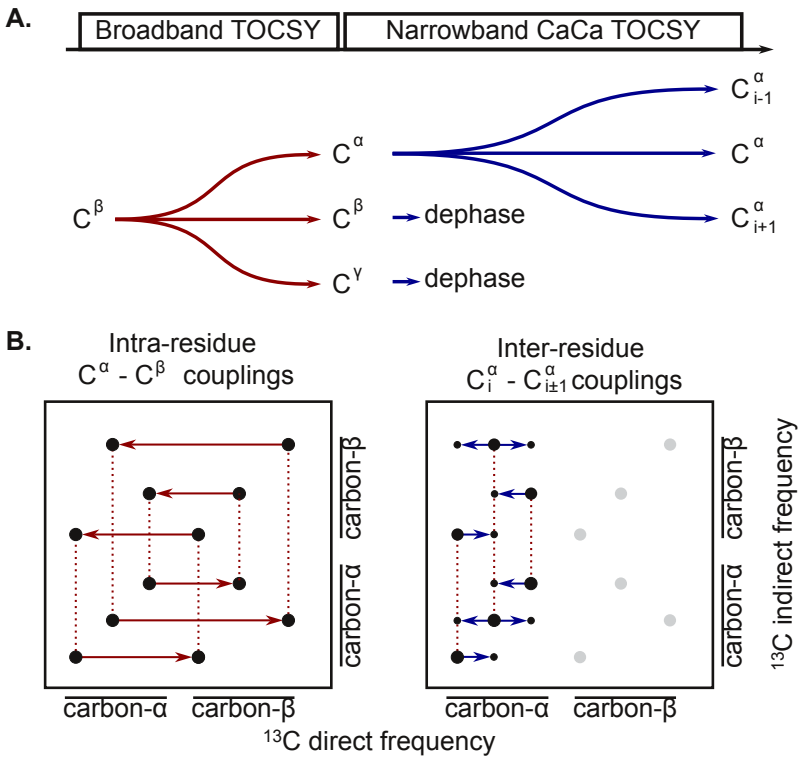

Figure 5.9: Broadband then narrowband pulse for sequential correlations. **A.** The TOCSY sequence comprises two distinct stages that resolve different couplings. For example, a component of the signal evolved at the carbon beta frequency during the indirect evolution time. The broadband TOCSY moves some of this magnetization on to the local carbon alpha, and the narrowband TOCSY moves the same component to another carbon alpha in a neighboring residue. After acquisition and Fourier transformation, there will be a cross peak with frequency co-ordinates (CB, $CA_{i\pm1}$). **B.** A schematic of the TOCSY spectra with and without the narrowband stage. The broadband TOCSY pulse generates intra-residues correlations, while inter-residue cross peaks are formed during the narrowband stage.

ing residues' alpha carbons. Inter-residue cross peaks are distributed over a large spectral width—the entire aliphatic bandwidth—rather than just the carbon alpha frequencies. In general there are several cross peaks between any adjacent residues. This helps alleviate ambiguity and overcrowding in CACA spectra. This correlation pattern cannot be observed using only broadband mixing, because the strong CACB couplings prevent efficient transfer across weak CACA couplings.

Figure 5.10 presents an experimental demonstration of the two-pulse scheme using a pen-

tapeptide sample. Subfigure 5.10A shows the spectrum after *only* a standard broadband mixing pulse (in this case, the pulse is the one given in Table 2.1. The mixing time was 29 ms, and the pulse power was 3.5 kHz). The five aligned columns of peaks correspond to the five residues in the sample. In this sample there are three residues that each have two aliphatic resonances, namely phenylalanine, histidine, and alanine. Without prior knowledge of the resonance frequencies of the relevant nuclei, there is insufficient connectivity information in 5.10A to establish beyond doubt which columns of peaks correspond to which amino acids. In practice, historical chemical shift data is available, which serves as a guide to which peaks arose from which kinds of amino acid. Of course, in larger samples, similar ambiguities arise from the presence of multiple versions of the same residue within the chemical structure, or from residues with very similar historical distributions of resonances.

Subfigure 5.10B shows a spectrum recorded with a two stage TOCSY. Firstly, NF4 was applied for 27.82 ms, at a power level of 4.5 kHz. This is immediately followed by the narrowband pulse for 91.20 ms, with a power level of 2 kHz. The carrier frequency was 55 ppm for both stages. The new peaks—the ones not present in Subfigure 5.10A—have been colored differently for visual clarity. The five columns of peaks, corresponding to the five residues in the sample, are still present. However, now there are several extra cross peaks in each column. The new peaks encode inter-residue correlations. For example, the proline (four-spin) and isoleucine (five-spin) system on the left of the spectrum are now correlated by seven new cross peaks. Possibly, there would be nine such cross peaks if it was not for the two residues having an overlapping frequency at 27 ppm. This provides a wealth of evidence that these two amino acids are adjacent in the chemical structure of the sample.

The isoleucine resonances at 13 ppm and 18 ppm have also been correlated with 57 ppm, by two new peaks at the top-center of Subfigure 5.10B. Moreover, the diagonal peak at 57 ppm is now correlated with the isoleucine column, by a new cross peak with coordinates (60

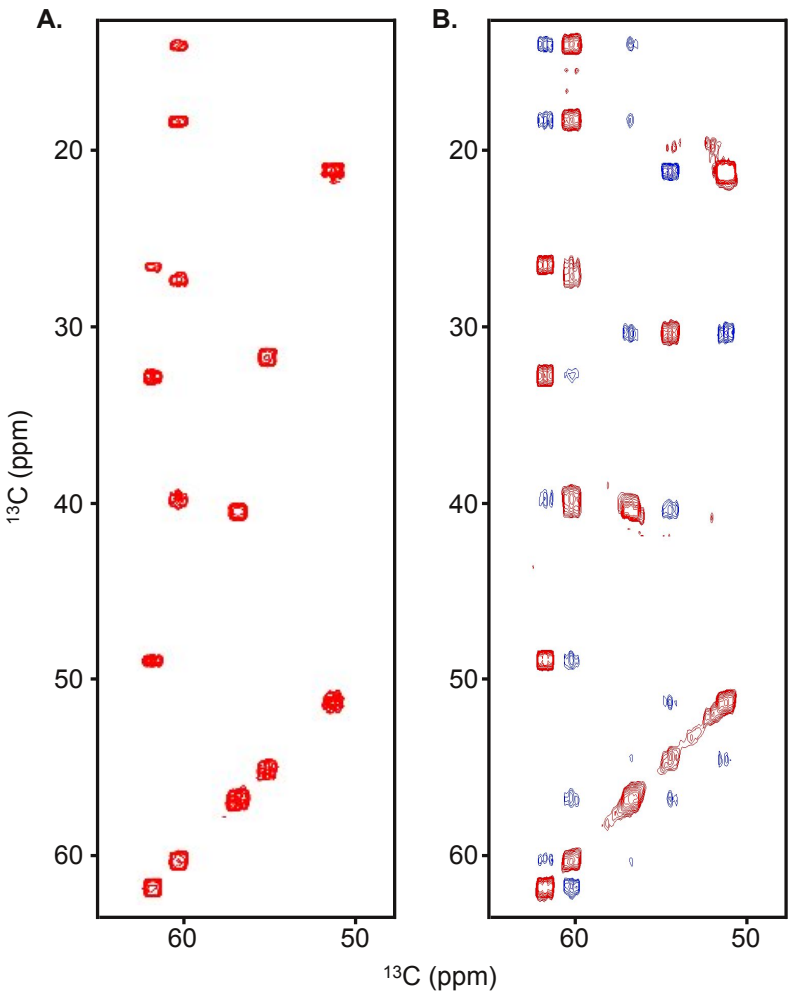

Figure 5.10: Broadband then narrowband pentapeptide spectrum. **A.** Broadband TOCSY of a PIFHA [U-13C,15N] labeled pentapeptide resolving 35 Hz intra-residue couplings. Each of the five columns corresponds to one amino acid in the sample. **B.** Two stage broad-then-narrow TOCSY further correlates each peak to the neighboring carbon alphas (all peaks are in phase; colors are a visual aid only). There are several new cross peals which indicate connectivities between adjacent residues.

ppm, 57 ppm). Altogether, this makes three separate pieces of evidence that isoleucine is adjacent with the two-spin system at 57 ppm. The amino acid sequence is Pro-Ile-Phe-His-Ala. Therefore, it can be concluded that the column of peaks at 57 ppm was generated by phenylalanine. Continuing in this way, it is straightforward to complete the assignment of the pentapeptide spectrum. There are several corroborating, inter-residue cross peaks for

each assigned residue.

For this simple sample, Figure 5.10 contains enough information to unambiguously assign the spectrum even with no prior knowledge of the likely chemical shift frequencies of particular nuclei. Interestingly, the assignment can be carried out even without prior knowledge of the number of aliphatic spins in each residue. This is because there is only one possible ordering of the five columns in Subfigure 5.10A that is consistent with the new cross peaks in Subfigure 5.10B. Inter-residue connectivity can be traced all the way from the proline to the alanine signals in several different ways. In other words, the information content of Figure 5.10 is highly redundant; if some of the inter-residue cross peaks were missing, the resonance assignment could still be completed.

The next step in this project is to apply the two-stage mixing sequence to protein samples, and to embed the it in higher-dimensional experiments (involving nitrogen and hydrogen nuclei) where it is potentially valuable for sequential resonance assignment.

5.3.2 Assignment of aromatic carbons

In this subsection, a temporally orchestrated sequence is developed for generating cross peaks between aliphatic and aromatic nuclei. The method uses two dual-band pulses with different band selectively.

Four of the common amino acids contain aromatic rings. These are phenylalanine, histidine, tryptophan, and tyrosine. Altogether, these have a relative abundance in proteins of 10.8% (Ulrich et al. 2008). That is, around 10.8% of the amino acids in protein samples will contain aromatic rings. The aromatic carbons resonate at around 110–140 ppm—relatively far from the aliphatic carbon resonances at 5–75 ppm.

There exists a significant difficulty in assigning aromatic resonances. The efficiency of magnetization transfer from aliphatic spins to aromatic spins is low. This is due to a combination of two effects: strong couplings amongst spins within the aromatic region (55–60

Hz), and large chemical shift differences across aliphatic-aromatic bonds. In particular, the chemical shift differences amongst either the aromatics or the aliphatics are much smaller than the chemical shift difference between these two groups, which serves to further suppress the transfer. This means that the aliphatic and aromatic carbons will tend to behave like two independent subsystems; sharing of magnetization across the single aliphatic-aromatic bond occurs very slowly. This is true even in the presence of extremely high-powered isotropic mixing pulses (Kovacs and Gossert 2014). Therefore, broadband mixing pulses that cover both the aliphatic and aromatic regions of the spectrum are of limited value for mixing between these two regions.

However, it is possible to increase transfer efficiency across the relatively weak aliphatic-aromatic coupling by effectively *decoupling* the other, stronger, bonds. This is similar to how the weak inter-residue couplings between neighboring carbon-alphas were isolated in Subsection 5.3.1. Consider the historical distribution of carbon chemical shifts in phenylalanine, depicted in Figure 5.11B. The nodes of this diagram are two standard deviations wide. These statistics are taken from protein NMR resonance assignments that have been submitted to the Biological Magnetic Resonance Data Bank (Ulrich et al. 2008). Clearly, the carbon gamma is shifted down-field from the other aromatic carbons. At the same time, the carbon beta is well-separated from the carbon alpha. This raises the following possibility: a dual-band pulse that selectively spin-locks the beta and gamma carbons, but which is narrow enough to *exclude* the other carbons, could isolate the 40 Hz J_{CbCg} coupling. This coupling could then evolve without the confounding effects of the strong (55–60 Hz) intra-aromatic and 35 Hz J_{CaCb} couplings.

Using a simple dual-band mixing pulse (see Subsection 2.4.1) with low RF power, two suitably placed spin-locking bands can be produced. As explained in Section 5.1, the effective coupling is reduced by half under the dual-band scheme, i.e. it is reduced to 20 Hz. However,

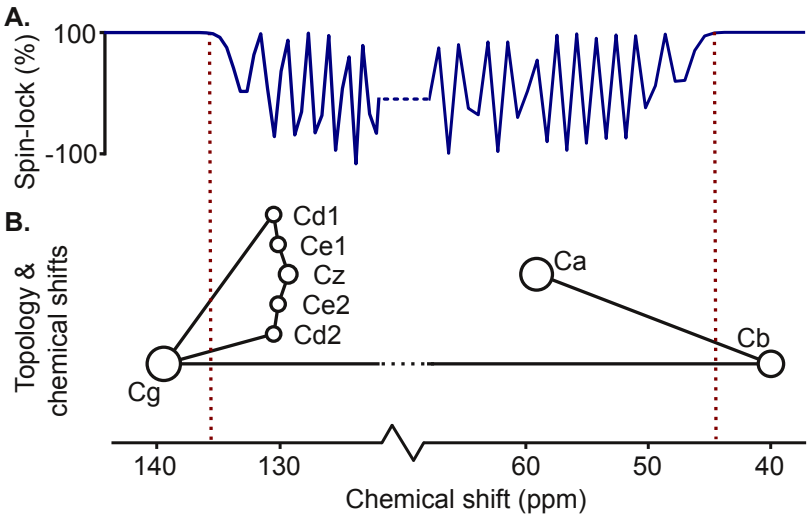

Figure 5.11: A selective spin-locking pulse designed to resolve the beta-gamma coupling in phenylalanine. **A.** A dual band spin-locking pulse is simulated. The bands cover only the beta and gamma carbons, while excluding the other spins in the network. The effective coupling is halved to $J_{\mathrm{CbCg}}/2 \approx 20$ Hz. The other carbons are effectively decoupled. The pulse parameters are given in Table 5.4, part two. **B.** A schematic of the topology and distribution of chemical shifts for phenylalanine. Each node is two standard deviations wide; vertices represent chemical bonds. The carbon-alpha and most of the aromatics reliably fall outside the spin-locked frequency bands. Statistical data and chemical structures are from the Biological Magnetic Resonance Data Bank (Ulrich et al. 2008).

due to the selective spin-locking, the other couplings are mostly or wholly removed. The pulse parameters are given in Table 5.4. Under this pulse, magnetization can be exchanged relatively quickly across the J_{CbCg} coupling. The spin-locking profile of the pulse is given in Figure 5.11A, which also shows how selection of the two spins of interest is achieved.

This experiment can be extended using a simple temporal scheme, so that not only CbCg cross peaks are resolved, but also cross peaks between other aliphatic and aromatic carbons. A *second* dual-band pulse was designed, which *includes* all phenylalanine aliphatic and aromatic resonances. That is, one band covers Ca and Cb; the other band covers all carbon resonances from the aromatic ring. With a short mixing time (e.g. around 10 ms) this pulse mixes some of the magnetization originating on Ca to Cb, as well as some of the Cd, Ce, and Cz magnetization to Cg. This is followed immediately by the highly selective pulse depicted

	$k=0$	1	2	3
Part 1 (two broad bands)				
u_k/v_3	0	2.7266	1.4921	$v_3 = 0.3764$
f_k	-	6.0222	3.0111	1.5056
Tf_k	-	4	2	1
Part 2 (two bands tailored to CbCg coupling)				
u_k/v_3	0	1.0927	0.5980	$v_3 = 0.1508$
f_k	-	6.6367	1.2067	0.0.6033
Tf_k	-	11	2	1

Table 5.4: The amplitudes u_k and frequencies f_k in kHz for the two pulses used to resolve the aliphatic-aromatic cross peaks in phenylalanine. Part one has bands that cover the whole aromatic and aliphatic regions. The pulse time is T =0.664 ms, and the root-mean-square RF amplitude is 5 kHz. Part two isolates the CbC coupling. The pulse time is T =1.657 ms, and the root-mean-square RF amplitude is 2 kHz. For both stages, the carrier frequency should be set at 90 ppm for band placement.

in Figure 5.11A, which exchanges Cb and Cg components.

The combined effect of the two pulses is as follows: A component of magnetization which originated on Ca is mixed to Cb during the first part of the pulse, and on to Cg during the second part of the pulse. This produces a (Ca, Cg) cross peak in the TOCSY spectrum. At the same time, a component of magnetization that originated on Cb *remained* on Cb during part one (assuming the duration of part one was not too long), and then moved on to Cg. The TOCSY spectrum will, therefore, include a (Cb, Cg) cross peak. Similarly, magnetization that began on any of Cd, Ce, or Cz mixed partly on to Cg during part one, and then on to Cb during part two. This means that the TOCSY spectrum will include a range of cross peaks that are at aromatic frequencies in the indirect dimension, and on the Cb in the direct dimension.

An experimental verification of this two-stage pulse is given in Figure 5.12. The first pulse was applied for 10.61 ms; the second pulse was applied for 26.52 ms. The total mixing duration is shorter than the time usually needed to move even a small amount of magnetization between the aliphatic and aromatic nuclei (Kovacs and Gossert 2014). However, under the

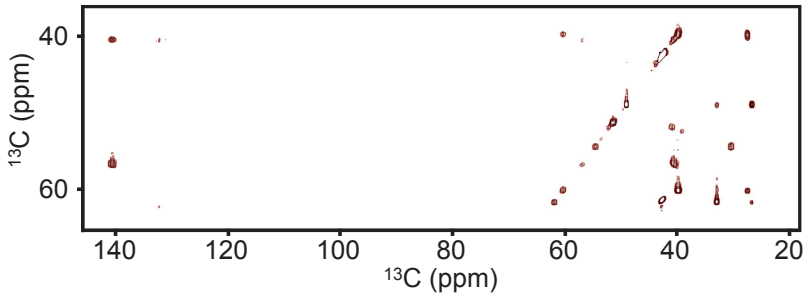

Figure 5.12: A temporal scheme comprising two dual-band pulses is applied to a pentapeptide sample containing phenylalanine. Cross peaks from the carbon alpha and beta to the carbon gamma are strongly resolved at 140 ppm. During the first part of the pulse, the alpha and beta nuclei exchanged approximately half their magnetization, so that signal components that originated on each of these spins was present on the carbon beta. The second part of the pulse exchanged beta and gamma magnetization, generating the two cross peaks on the left on the spectrum. The mixing times were 10.61 ms (Part 1) and 26.52 ms (Part 2).

temporal scheme, these mixing times are chosen to produce approximately complete transfer.

This method has been explored in detail for the case of phenylalanine, but could easily be adapted for other amino acids containing aromatic resonances. The carbon gamma of tryptophan resonates at 111 ppm, which is about 15 ppm away from the resonance frequencies of the coupled aromatics delta-1 and delta-2. Therefore, a suitable dual-band pulse could isolate the J_{CbCg} coupling, and embedding this in a two-stage temporal scheme could provide further connectives. Similarly, the histidine gamma chemical shift is separated from the other aromatic nuclei, so the same strategy is applicable.

Unfortunately, the same is not true of tyrosine; its carbon gamma chemical shift is too close to the shifts of the other aromatic residues for the J_{CbCg} coupling to be reliably isolated by dual-band selectivity. Moreover, it is not clear how the aliphatic-aromatic correlations could be generated for several different residues in the same experiment, meaning that a separate spectrum would be required each of phenylalanine, histidine, and tyrosine. Despite these shortcomings, the technique may be applicable for e.g. resolving a specific ambiguity

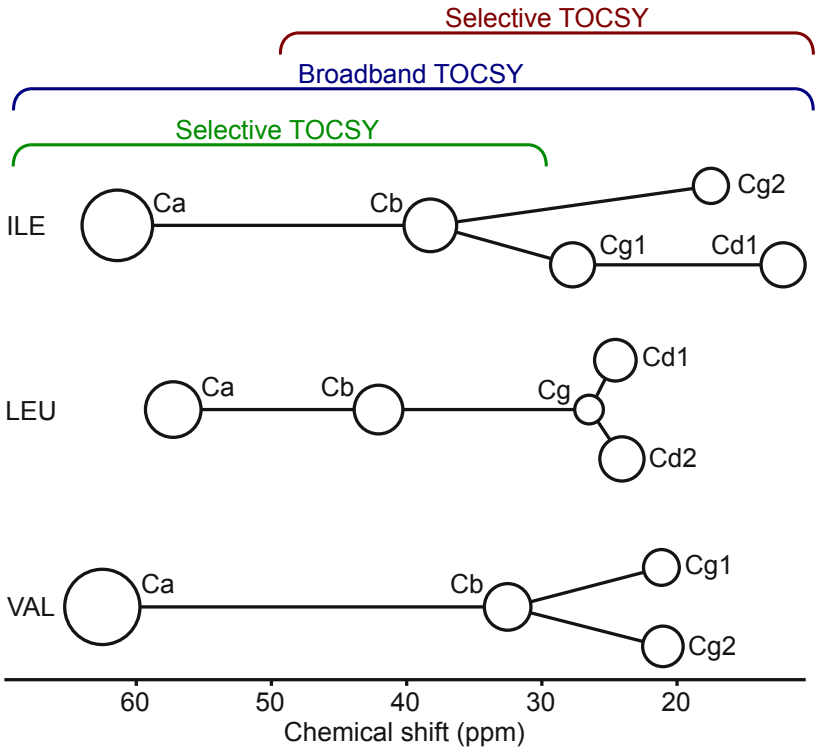

Figure 5.13: Couplings and chemical shifts for ILV systems. Each node is 2 standard deviations wide. Vertices represent chemical bonds, assumed to correspond a J-coupling of 35 Hz. Statistical data and chemical structures are from the Biological Magnetic Resonance Data Bank (Ulrich et al. 2008). It is clear that a narrowband selective TOCSY pulse can easily exclude all the carbon alphas, so long as the coupling is maintained below about 45 ppm but eliminated above about 55 ppm. It may also be possible to mix *just* the alpha and beta carbons, though some residual effective coupling to the gamma carbons of isoleucine and leucine might be encountered. Including a standard broadband pulse, there is a set of three mixing pulses which can be used at different times during the mixing sequence.

in a protein assignment.

5.3.3 Methyl assignment

In this subsection, the importance of the specific transfer from methyl to alpha carbons is briefly explained, and a simple example of a temporal scheme to increase the transfer efficiency is suggested.

Larger proteins tumble more slowly in liquid than smaller proteins, leading to more rapid

loss of signal through relaxation. Therefore, NMR spectroscopy of large proteins is more challenging than for small proteins. However, methyl (i.e. CH_3) groups relax much more slowly than other parts of the sample; the rapid motion of the three attached protons forms a subsystem with slower relaxation than the protein at large. Methyl groups occur in several amino acids, notably isoleucine, leucine, valine (ILV), and alanine. Spatially dependent cross relaxation rates between methyls can be particularly useful for studies of large proteins (Tugarinov et al. 2005). This means that the utility of NMR spectroscopy can be extended through strategies that focus on the resonances associated with methyl groups.

However, before the measured cross relaxation rates can be used for structure determination, the relevant resonance frequencies must be assigned to the correct nuclei. Assignment experiments depend on the ability to create methyl-alpha cross peaks using TOCSY transfer. The historical distributions of resonance frequencies for ILV carbon nuclei are shown in Figure 5.13. Clearly, the resonance frequencies are sufficiently separated that the narrowband pulse described in Section 5.2 could effectively decouple some of the spins, while allowing other spins to exchange magnetization.

Transfer efficiency is dependent the spin system's coupling topology. Selective isotope labeling schemes can alter the topology and yield higher cross peak intensity under standard TOCSY pulses, such as FLOPSY-16 with high RF power. The best available labeling scheme *linearizes* the spin coupling topology for each residue that contains a methyl group, i.e. it replaces a branched topology with one in which the spins are arranged in a linear chain. Intuitively, this allows magnetization to flow from the methyl, through a number of intermediate carbon-13 nuclei, towards the alpha, without being diverted along pathways that do not lead to the alpha carbon. This is called stereo-specific labeling. In particular, the gamma-2 in isoleucine, one of the deltas in leucine, and one of the gammas in valine are (un)labeled with carbon-12, and therefore NMR-inactive. With this scheme, isoleucine and leucine have the same topology, four spins in a linear chain, while valine has three spins in

a linear chain.

Subfigure 5.14A shows the efficiency of transfer from the methyl carbon to alpha carbon as a function of mixing time. The pulse is assumed to be a broadband mixing pulse run at high RF power, so that all couplings are fully maintained at their intrinsic magnitude of 35 Hz. After 19–24 ms, a reasonable portion of magnetization has moved to the carbon alpha. One immediate problem is that maximum transfer efficiency occus at *different* mixing times for different residues. This means that cross peak intensity cannot simultaneously be maximized for all relevant transfers.

Subfigure 5.14B considers a mixing protocol that switches between three available mixing pulses. The first is selective for the spins with chemical shift frequencies less that approximately 50 ppm. This effectively decouples the carbon alphas, and can be realized in practice using the narrowband mixing pulse developed in Section 5.2. The second pulse is broadband, and maintains all couplings at their intrinsic magnitude of 35 Hz. The third pulse is selective for the carbon alphas and betas. The placement of the pulse bandwidths is depicted in Figure 5.13. The first selective mixing pulse runs for 12.5 ms, then the broadband mixing pulse runs for 5.5 ms. The second selective mixing pulse runs for the remaining 8.5 ms. The two switching times were found by exhaustive numerical search of the two-parameter space. The resultant transfer function has two highly favorable features: the transfer efficiency is higher, and the maxima for all ILV systems occurs at the same time, $t_{\text{mix}} = 26.5$ ms.

The carbon beta in valine resonates at a frequency which is quite close to the gamma-1 in isoleucine. Therefore, there is a question as to whether the gamma-1 of isoleucine will be *completely* decoupled during the third pulse. Similarly, it is possible that alpha-beta coupling of valine might not be fully maintained. These problems arise if any resonance is in the transition region of the selective mixing pulse (see Subfigure 5.7A). Subfigure 5.14C shows the effect of not fully removing gamma-1 during the third part of the pulse. A small

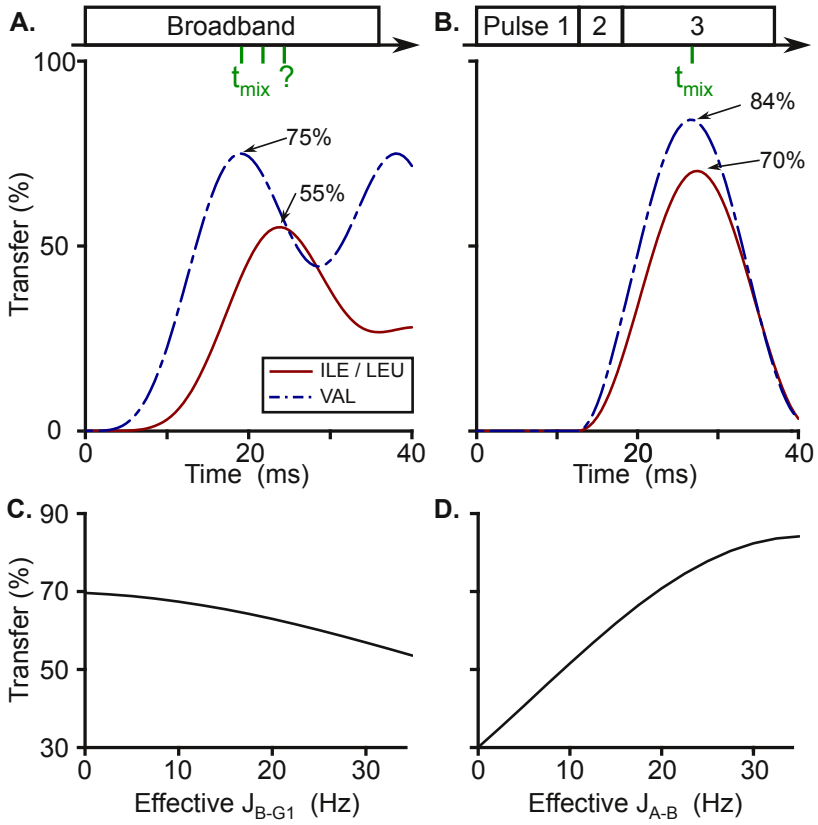

Figure 5.14: Stereo-specifically labeled ILV magnetization transfer under two mixing protocols. **A.** Broadband isotropic mixing is applied; all effective couplings are 35 Hz for the entire mixing time. The initial state has magnetization on the methyl carbon nucleus in each system, and the proportion of this magnetization that has been transfered to the carbon alpha is plotted. The isoleucine and leucine transfer is maximized at $t_{\mathrm{mix}} = 24$ ms, while the valine maximum is at $t_{\mathrm{mix}} = 19$ ms. **B.** Three mixing pulses are applied in sequence. The first selectively excludes the alpha region, the second is broadband, and the third is selective for the alpha and beta regions. The maximum transfers are all at 26.5 ms, and are higher than under the broadband pulse. **C.** The effect of a small residual effective coupling between beta and gamma-1 isoleucine carbons (incomplete selectivity) during the third pulse. As long as the gamma-1 is mostly excluded, the transfer measured at 26.5 ms is near 70%. **D.** The effect of weakened alpha-beta coupling in valine during the third pulse. Ideally, the narrowband pulse will maintain $J_{\mathrm{AB}}^{\mathrm{eff}} = 35$ Hz, but slightly lower effective values still yield high efficiency.

residual coupling will still give higher transfer efficiency than simple broadband mixing. Subfigure 5.14D shows that the effective alpha-beta coupling in valine must be quite strong (25–35 Hz) to achieve high transfer efficiency from the methyl to the alpha nuclei.

These simulations suggest that methyl-to-alpha transfer in stereo-specifically labeled ILV systems could be more efficient with time-varying effective J-couplings than with a single TOCSY pulse. The suggested scheme depends crucially on the selective mixing pulse derived using the multi-frame method.

There are two particularly relevant remaining questions: Firstly, whether even higher transfer efficiency could be achieved with a different time-varying set of mixing pulses. Secondly, whether the increased transfer efficiency in a time-varying protocol, as compared with simple broadband mixing, can be realized and demonstrated in experiments on proteins.

5.4 Summary

This chapter explored the design and usefulness of TOCSY mixing pulses that, instead of being broadband, produce mixing across separated bands or within a narrow region. A high degree of control over the chemical shift dependence of the mixing efficiency was achieved. This led to the idea of using several different mixing pulses in sequence, so that the effective magnitude of the J-couplings could be varied in time. Time-varying effective J-couplings produce higher transfer efficiency for certain sets of cross peaks than can be achieved with time-invariant effective J-couplings.

Dual-band mixing pulses have previously been developed for a range of applications in liquid state and solid state NMR. Several improvements have been demonstrated in this chapter. Constraints on the spacing of the spin-lock bands (to avoid distorting effects in one spectral band arising from the spin-locking of the other band), can be largely avoided using repeated rotating frame pulses. For example, the pulse simulated in Figure 5.4 has

bands that are very wide relative to the gaps between bands. Tri-band-selective mixing tailored to the three main parts of the carbon spectrum, and dual-band mixing with unequal bandwidths, were also demonstrated.

Narrowband mixing was achieved with a simple modification to the design algorithm. The sharp selectivity of the narrowband pulse can be used to isolate the carbon alpha region of the spectrum, while decoupling the other aliphatic nuclei.

Finally, the utility of time-varying effective J-couplings, bought about by switching between different pulses during the mixing period, was explored. In particular, mixing protocols were designed for three tasks relevant to protein NMR: mixing across weak couplings between carbon alphas in neighboring residues, assigning aromatic resonances, and transferring magnetization between methyl and alpha carbons in ILV systems. In all three cases, dynamically switching between different mixing pulses improves upon what is possible using a single pulse for the whole mixing time. The protocols that were developed all depend on mixing pulses that have highly specific offset dependency, which were easily and quickly created using the method of repeated rotating frames.

6

Conclusion

The multi-frame method for pulse design provides an analytical solution to the problem of large bandwidths in correlation NMR, relying on familiar kinds of Hamiltonian transforms (tilted axes, rotating frames, and rotating wave approximations), and does not require numerical searches/optimizations. Equation (2.2) allows chemical shift bandwidths to be precisely manipulated in a variety of ways, which have been explored in this document. With some care, a pulse can be engineered so that the pairwise couplings between spins dominate the effective Hamiltonian—a highly desirable situation in homonuclear mixing experiments. These mixing pulses have been successfully applied in carbon TOCSY experiments over large

bandwidths and at low RF power levels.

One pulse in particular, NF4, has favorable properties for broadband TOCSY. Its bandwidth, relaxation, and robustness to RF inhomogeneity have been studied in detail. NF4 out-performs the widely-used FLOPSY-16 sequence in both simulations and experiments, and therefore should find use in protein NMR experiments.

Precise control over the chemical shift band structure has facilitated the resolution of new, and highly informative, patterns of correlation. Temporally orchestrated pulses were shown to be capable of generating novel patterns of correlation among resonances. In particular, switching on or off strong couplings can allow weaker couplings to evolve during parts of the mixing period. This is made possible by new pulses with specific selectivity properties, designed by repeated rotating frames. For example, the highly selective narrowband pulse, or the dual-band pulse that targets the CbCg coupling in phenylalanine.

The mixing of side-chain carbons to the nearest neighbor amino acid is potentially a useful assignment technique, especially for small samples. This pattern can only be efficiently generated under a two-stage approach (broadband then narrowband TOCSY). The narrowband mixing pulse designed with multi-rotating frames has much sharper cutoffs than alternatives, ensuring that the desired transfer of signal can be precisely orchestrated. The pulse that isolates the CbCg coupling in phenylalanine can be embedded in a longer TOCSY pulse which targets other couplings at other times. This allows for rapid transfer of magnetization between the aromatic and aliphatic carbon nuclei. Under broadband mixing approaches, this transfer is severely hindered by the presence of other, stronger couplings. The repeated rotating frame method allows for simple and accurate control of the cutoffs and placement of dual bands, which allowed the strong intra-aromatic and intra-aliphatic bonds to be selectively decoupled.

There are several remaining topics worth exploring in the future. New refocusing and excitation pulses are needed for applications at high Zeeman field, since the standard rect-

angular pulses introduce intolerably large phase errors. Low power multi-band pulses are a possible solution, especially for the carbon channel. The same is true for fluorine NMR: even at relatively low Zeeman fields, the bandwidth of fluorine resonances is many times larger than the maximum allowable RF power. Spin-locking pulses which are tailored to a few specific frequency bands could be used for excitation, decoupling, and mixing of fluorine nuclear spins. These could be rapidly designed to suit particular samples, using the multi-frame method. Temporally orchestrated pulses have the potential to lead to novel protein assignment strategies, but this needs to be demonstrated experimentally for large protein samples.

The method of repeated rotating frames offers analytical control over the offset dependence of NMR pulses, and particularly mixing pulses. This thesis has demonstrated the usefulness of this method for a range of existing and emerging applications in protein NMR. This work has also contributed a set of specific pulse sequences, notably NF4, which can be easily included in standard experiments.

A

The dynamics of nuclear spin

In this appendix, the dynamical equations relevant to spin-1/2 NMR are reviewed. This material is standard in NMR textbooks (Levitt 2008; Cavanagh et al. 2007) and also in introductory quantum mechanics texts (Griffiths 2005; Merzbacher 1998).

The review starts with the density matrix formulation for isolated (non-interacting) spins, before describing coupled spin systems, measurement, and the calculation of effective Hamiltonians when the frame of reference is changed.

A.1 An isolated spin-1/2

The state of an isolated nuclear spin-1/2 is described using a basis of Pauli spin operators,

$$I_{\mathrm{x}} = \frac{\hbar}{2}\begin{bmatrix} 0 & 1 \\ 1 & 0 \end{bmatrix}, \quad I_{\mathrm{y}} = \frac{\hbar}{2}\begin{bmatrix} 0 & -i \\ i & 0 \end{bmatrix}, \quad I_{\mathrm{z}} = \frac{\hbar}{2}\begin{bmatrix} 1 & 0 \\ 0 & -1 \end{bmatrix}$$

obeying the commutation relation $[I_{\mathrm{x}},\ I_{\mathrm{y}}] = i\hbar I_{\mathrm{z}}$ and cyclic permutations. A state $\rho(t) = M_{\mathrm{x}}(t)I_{\mathrm{x}} + M_{\mathrm{y}}(t)I_{\mathrm{y}} + M_{\mathrm{z}}(t)I_{\mathrm{z}}$ can be thought of as a classical unit vector $\vec{M}(t)$ evolving on the Bloch sphere. The Hamiltonian is also expressed in this basis, and can be thought of as cataloging the total energy associated with each allowable state. Since the Hamiltonian encodes the potential energy of each state, it determines the evolution of the system. Both the density matrix and Hamiltonian are, in general, time-varying. According to quantum mechanics the evolution of the density matrix is given by the von Neumann equation (which is equivalent to the Schrödinger equation)

$$i\hbar\frac{d}{dt}\rho(t) = [H(t),\ \rho(t)]$$

where $H(t)$ is measured in energy units. It is convenient to absorb $\hbar$ into the Hamiltonian so that it is expressed in frequency units. Then the dynamics is

$$\frac{d}{dt}\rho(t) = -i[H(t),\ \rho(t)] \tag{A.1}$$

This can be integrated from initial time $t = 0$ to final time $t = T$ to form a unitary transition matrix $V(T)$,

$$\rho(T) = V^{\dagger}(T)\rho(0)V(T), \text{ where}$$
$$\frac{d}{dt}V(t) = -iH(t)V(t), \text{ and } V(0) = I$$

Since $V(T)$ does not depend on the density matrix it can be calculated directly from the Hamiltonian and applied to any initial state. The unitary transition matrix corresponds to a (non-unique) *effective* or *average* time-invariant Hamiltonian

$$V(T) = \exp(-iH^{\text{eff}}T)$$

Observe from this that when the Hamiltonian is time-invariant ($H = H^{\text{eff}}$) the unitary solution to the von Neumann equation $V(T)$ is given in closed form by a matrix exponential.

A.2 Multiple interacting spins-1/2

In the case of multiple interacting spins, we must expand the operator basis using the tensor structure of quantum mechanics. The state space for a single spin contains four elements (the three Pauli operators and the identity, where the latter does not affect the dynamics), while the state space for two interacting spins contains 16 operators. The operators corresponding to magnetization of one of the spins are given by a tensor product with the identity, for example

$$I_{1y} = I_{\text{y}} \otimes I_{2\times 2}, \quad \text{and}$$
$$I_{2y} = I_{2\times 2} \otimes I_{\text{y}}$$

where $I_{2\times 2}$ is the identity matrix of dimension 2. When the meaning is clear from the context, it is common to use the alternative notation I_{y} for I_{1y} and S_{y} for I_{2y}. Then the sixteen basis elements for the two-spin system are given by the following 4-by-4 matrices

$$I_{\mathrm{x}},\ I_{\mathrm{y}},\ I_{\mathrm{z}},\ S_{\mathrm{x}},\ S_{\mathrm{y}},\ S_{\mathrm{z}},\ 2I_{\mathrm{x}}S_{\mathrm{x}},\ 2I_{\mathrm{x}}S_{\mathrm{y}},\ 2I_{\mathrm{x}}S_{\mathrm{z}},\ 2I_{\mathrm{y}}S_{\mathrm{x}},$$
$$2I_{\mathrm{y}}S_{\mathrm{y}},\ 2I_{\mathrm{y}}S_{\mathrm{z}},\ 2I_{\mathrm{z}}S_{\mathrm{x}},\ 2I_{\mathrm{z}}S_{\mathrm{y}},\ 2I_{\mathrm{z}}S_{\mathrm{z}},\ \text{and}\ I_{4\times 4}$$

The first six of these are called *single quantum operators*.

In the case of many interacting spins, the Pauli matrices for each individual spin are bought into the correct state space via tensor products with many copies of the identity,

$$I_{\mathrm{kx}} = I_{2\times 2}\otimes I_{2\times 2}\cdots\otimes I_{2\times 2}\otimes \underbrace{I_{\mathrm{x}}}_{\text{position k}} \otimes I_{2\times 2}\cdots\otimes \underbrace{I_{2\times 2}}_{\text{position n}}$$

The state space also contains all possible products of the individual spin operators, including double-quantum and triple-quantum operators, and so on. The dimensionality of the state space grows exponentially with the number of interacting spins. In particular, the number of basis operators for an n spin system is 4^n, while the square matrices involved have dimension 2^n. The dynamical equation (A.1) is the same, regardless of the number of spins being modeled.

A.3 Measurement

In quantum mechanics, the instantaneous expectation value of a Hermitian operator A is given by $\langle A\rangle(t) = \mathrm{trace}(A(t)\rho(t))$. The measured signal in NMR is proportional to the expectation of single quantum operators in the transverse plane for all nuclear spins $\{I_{\mathrm{kx}},\ I_{\mathrm{ky}}\}$ during the acquisition of the oscillatory free induction decay signal. The properties of the free induction decay and many associated signal processing issues are described at length

elsewhere, for example in the book *NMR Data Processing* (Hoch and Stern 1996). For the purposes of this thesis it is sufficient to say that the amplitude of the signal of interest is proportional to trace$(A\rho(T))$, where T is the end of the applied pulse, and A is some linear combination of single quantum operators specific to the application.

A.4 Change of reference frame

Suppose we define a change of variables (such as a frame transformation) to the density matrix, described by a unitary operator $U(t)$,

$$\rho'(t) = U(t)\rho(t)U^\dagger(t)$$

Then the dynamics of $\rho'(t)$ is given by the von Neumann equation with an effective Hamiltonian (Cavanagh et al. 2007)

$$H'(t) = U(t)H(t)U^\dagger(t) - iU(t)\frac{d}{dt}U^\dagger(t) \tag{A.2}$$

This equation is used in throughout this thesis to engineer a desired effective Hamiltonian using a combination of pulses and simple frame transformations. In the case where $U(t)$ is a (possibly time-varying) rotation about a fixed axis, (A.2) can be simplified. For example, let

$$H(t) = a(t)I_\mathrm{x} + b(t)I_\mathrm{y} + c(t)I_\mathrm{z}$$
$$U(t) = \exp(if(t)I_\mathrm{z})$$

Then

$$\begin{aligned} H'(t) =& a(t)\left(\cos(f(t))I_{\mathrm{x}} - \sin(f(t))I_{\mathrm{y}}\right) + b(t)\left(\cos(f(t))I_{\mathrm{y}} + \sin(f(t))I_{\mathrm{x}}\right) \\ &+ \left(c(t) - \frac{d}{dt}f(t)\right) I_{\mathrm{z}} \end{aligned}$$

Similar expressions for rotations about the x or y axes can be found by cyclically permuting the Pauli operators in this expression.

References

Anderson, W. A., Freeman, R., Jul. 1962. Influence of a Second Radiofrequency Field on High-Resolution Nuclear Magnetic Resonance Spectra. Journal of Chemical Physics 37, 85–103.

Bai, N., Ramachandran, R., 1993. Numerical design of broadband homonuclear isotropic-mixing sequences. Journal of Magnetic Resonance, Series A 105 (3), 298–303.

Bax, A., 1988. Homonuclear Magnetization Transfer Experiments Using Isotropic and Non-isotropic Mixing Schemes. Israel Journal of Chemistry 28 (4), 309–317.

Bax, A., Davis, D. G., 1985. MLEV-17-based two-dimensional homonuclear magnetization transfer spectroscopy. Journal of Magnetic Resonance 65 (2), 355–360.

Bennett, A. E., Gross, J. D., Wagner, G., 2003. Broadband ^{13}C–^{13}C adiabatic mixing in solution optimized for high fields. Journal of Magnetic Resonance 165 (1), 59–79.

Bernstein, M. A., King, K. F., Zhou, X. J., 2004. Handbook of MRI pulse sequences. North-Holland, Amsterdam.

Bloch, F., Siegert, A., 1940. Magnetic resonance for nonrotating fields. Physical Review 57, 522–527.

Bohlen, J.-M., Rey, M., Bodenhausen, G., 1989. Refocusing with chirped pulses for broadband excitation without phase dispersion. Journal of Magnetic Resonance 84 (1), 191–197.

Braunschweiler, L., Ernst, R., 1983. Coherence transfer by isotropic mixing: Application to proton correlation spectroscopy. Journal of Magnetic Resonance 53, 521–528.

Carlomagno, T., Luy, B., Glaser, S. J., 1997. "Kin" HEHAHA Sequences, Heteronuclear Hartmann-Hahn Transfer with Different Bandwidths for Spins I and S. Journal of Magnetic Resonance 126 (1), 110–119.

Carlomagno, T., Maurer, M., Sattler, M., Schwendinger, M. G., Glaser, S. J., Griesinger, C., 1996. PLUSH TACSY: Homonuclear planar TACSY with two-band selective shaped pulses applied to C^{α},C' transfer and C^{β},$C^{aromatic}$ correlations. Journal of Biomolecular NMR 8, 161–170.

Cavanagh, J., Fairbrother, W. J., Palmer, A. G., Skelton, N. J., Rance, M., 2007. Protein NMR Spectroscopy: Principles and Practice, 2nd Edition. Academic Press, San Diego.

Conolly, S., Nishimura, D., Macovski, A., June 1986. Optimal control solutions to the magnetic resonance selective excitation problem. IEEE Transactions on Medical Imaging 5 (2), 106–115.

Coote, P., Arthanari, H., Yu, T.-Y., Natarajan, A., Wagner, G., Khaneja, N., 2013. Pulse design for broadband correlation NMR spectroscopy by multi-rotating frames. Journal of Biomolecular NMR 55 (3), 291–302.

Coote, P., Leigh, K., Yu, T.-Y., Khaneja, N., Wagner, G., Arthanari, H., 2014. A new broadband homonuclear mixing pulse for NMR with low applied power. Under review.

Daems, D., Ruschhaupt, A., Sugny, D., Guérin, S., Jul 2013. Robust quantum control by a single-shot shaped pulse. Phys. Rev. Lett. 111, 050404.

Delaglio, F., Grzesiek, S., Vuister, G., Zhu, G., Pfeifer, J., Bax, A., 1995. NMRPipe: A multidimensional spectral processing system based on UNIX pipes. Journal of Biomolecular NMR 6 (3), 277–293.

Demers, J.-P., Vijayan, V., Becker, S., Lange, A., 2010. Tailored low-power cross-polarization under fast magic-angle spinning. Journal of Magnetic Resonance 205 (2), 216–223.

Emsley, L., Bodenhausen, G., 1990. Phase shifts induced by transient bloch-siegert effects in {NMR}. Chemical Physics Letters 168 (3–4), 297–303.

Ermakov, V. L., Bodenhausen, G., 1993. Broadband excitation in magnetic resonance by self-refocusing doubly frequency-modulated pulses. Chemical Physics Letters 204 (3–4), 375–380.

Ernst, R. R., Bodenhausen, G., Wokaun, A., 1987. Principles of Nuclear Magnetic Resonance in one and two dimensions. Clerendon Press, Oxford.

Felli, I. C., Pierattelli, R., Glaser, S. J., Luy, B., 2009. Relaxation-optimised Hartmann–Hahn transfer using a specifically tailored MOCCA-XY16 mixing sequence for carbonyl–carbonyl correlation spectroscopy in 13C direct detection NMR experiments. Journal of Biomolecular NMR 43 (3), 187–196.

Floquet, G., 1883. Sur les equations differentielles lineaires a coefficients periodiques. Annales de l'Ecole Normale Superieure 12, 47–88.

Freeman, R., Kempsell, S. P., Levitt, M. H., 1980. Radio-frequency pulse sequences which compensate their own imperfections. Journal of Magnetic Resonance 38 (453).

Furrer, J., Kramer, F., Marino, J. P., Glaser, S. J., Luy, B., 2004. Homonuclear Hartmann–Hahn transfer with reduced relaxation losses by use of the MOCCA-XY16 multiple pulse sequence . Journal of Magnetic Resonance 166 (1), 39–46.

Glaser, S., 1993. Coupling Topology Dependence of Polarization-Transfer Efficiency in TOCSY and TACSY Experiments. Journal of Magnetic Resonance, Series A 104 (3), 283–301.

Glaser, S. J., Drobny, G. P., 1990. Assessment and optimization of pulse sequences for homonuclear isotropic mixing. In: Warren, W. S. (Ed.), Advances in Magnetic Resonance. Vol. 14 of Advances in Magnetic and Optical Resonance. Academic Press, pp. 35–58.

Glaser, S. J., Quant, J. J., 1996. Homonuclear and heteronuclear Hartmann-Hahn transfer in isotropic liquids. Advances in Magnetic and Optical Resonance 19, 59–252.

Griesinger, C., Ernst, R., 1988. Cross relaxation in time-dependent nuclear spin systems: Invariant trajectory approach. Chemical Physics Letters 152 (2–3), 239–247.

Griffiths, D., 2005. Introduction to Quantum Mechanics, 2nd Edition. Prentice Hall.

Grzesiek, S., Bax, A., 1995. Audio-Frequency NMR in a Nutating Frame. Application to the Assignment of Phenylalanine Residues in Isotopically Enriched Proteins. Journal of the American Chemical Society 117 (24), 6527–6531.

Haeberlen, U., 1976. High resolution NMR in solids: selective averaging. Academic Press, New York.

Haeberlen, U., Waugh, J. S., 1968. Coherent averaging effects in magnetic resonance. Physical Review 175, 453–467.

Hartmann, S. R., Hahn, E. L., 1962. Nuclear double resonance in the rotating frame. Physical Review 128, 2042–2053.

Hedges, L., Hoult, D., 1988. The techniques of rotating frame selective excitation and some experimental results. Journal of Magnetic Resonance 79 (3), 391–403.

Hiller, S., Arthanari, H., Wagner, G., 2009. The t-lock: automated compensation of radio-frequency induced sample heating. Journal of Biomolecular NMR 44 (2), 69–76.

Hoch, J. C., Stern, A. S., 1996. NMR Data Processing. Wiley-Liss.

Hoult, D., 1980. NMR imaging. rotating frame selective pulses. Journal of Magnetic Resonance 38 (2), 369–374.

Hyberts, S. G., Arthanari, H., Wagner, G., 2012. Applications of non-uniform sampling and processing. In: Billeter, M., Orekhov, V. (Eds.), Novel Sampling Approaches in Higher Dimensional NMR. Vol. 316 of Topics in Current Chemistry. Springer Berlin Heidelberg, pp. 125–148.

Hyberts, S. G., Robson, S. A., Wagner, G., 2013. Exploring signal-to-noise ratio and sensitivity in non-uniformly sampled multi-dimensional NMR spectra. Journal of Biomolecular NMR 55 (2), 167–178.

Isham, C. J., 1995. Lectures on Quantum Theory: Mathematical and Structural Foundations. Imperial College Press, London.

Jones, J. A., 2011. Quantum computing with {NMR}. Progress in Nuclear Magnetic Resonance Spectroscopy 59 (2), 91–120.

Kadkhodaie, M., Rivas, O., Tan, M., Mohebbi, A., Shaka, A., 1991. Broadband homonuclear cross polarization using flip-flop spectroscopy. Journal of Magnetic Resonance 91 (2), 437–443.

Khaneja, N., 2009. On some model problems in quantum control. Communications in Information & Systems 9 (1), 1–40.

Klarsfeld, S., Oteo, J. A., 1989. Recursive generation of higher-order terms in the magnus expansion. Physical Review A 39, 3270–3273.

Kovacs, H., Gossert, A., 2014. Improved NMR experiments with 13C-isotropic mixing for assignment of aromatic and aliphatic side chains in labeled proteins. Journal of Biomolecular NMR 58 (2), 101–112.

Kupce, E., Freeman, R., 1994. Wideband excitation with polychromatic pulses. Journal of Magnetic Resonance, Series A 108 (2), 268–273.

Leskes, M., Madhu, P. K., Vega, S., 2010. Floquet theory in solid-state nuclear magnetic resonance. Progress in Nuclear Magnetic Resonance Spectroscopy 57 (4), 345–380.

Levitt, M. H., 1986. Composite pulses. Progress in Nuclear Magnetic Resonance Spectroscopy 18 (2), 61–122.

Levitt, M. H., 1997. The Signs of Frequencies and Phases in NMR. Journal of Magnetic Resonance 126 (2), 164–182.

Levitt, M. H., 2008. Spin Dynamics: Basics of Nuclear Magnetic Resonance, 2nd Edition. Wiley.

Levitt, M. H., Johannessen, O. G., 2000. Signs of Frequencies and Phases in NMR: The Role of Radiofrequency Mixing. Journal of Magnetic Resonance 142 (1), 190–194.

Li, J.-S., Khaneja, N., 2006. Control of inhomogeneous quantum ensembles. Physical Review A 73, 030302.

Li, J.-S., Khaneja, N., March 2009. Ensemble Control of Bloch Equations. IEEE Transactions on Automatic Control 54 (3), 528–536.

Llor, A., 1992. Equivalence between dynamical averaging methods of the Schrödinger equation: average Hamiltonian, secular averaging, and Van Vleck transformation. Chemical Physics Letters 199 (3–4), 383–390.

Magnus, W., 1954. On the exponential solution of differential equations for a linear operator. Communications on Pure and Applied Mathematics 7 (4), 649–673.

Mao, J., Mareci, T., Scott, K., Andrew, E., 1986. Selective inversion radiofrequency pulses by optimal control. Journal of Magnetic Resonance 70 (2), 310–318.

MATLAB, 2011. Version 7.13.0.564, Release 2011b. The MathWorks, Inc., Natick, Massachusetts, United States.

McCoy, M., Mueller, L., 1992. Nonresonant effects of frequency-selective pulses. Journal of Magnetic Resonance 99 (1), 18–36.

Merzbacher, E., 1998. Quantum Mechanics, 3rd Edition. John Wiley and Sons, Inc., New York, NY.

Morris, G. A., Freeman, R., 1979. Enhancement of nuclear magnetic resonance signals by polarization transfer. Journal of the American Chemical Society 101 (3), 760–762.

Müller, L., Ernst, R., 1979. Coherence transfer in the rotating frame. Molecular Physics 38 (3), 963–992.

Otten, R., Chu, B., Krewulak, K. D., Vogel, H. J., Mulder, F. A. A., 2010. Comprehensive and Cost-Effective NMR Spectroscopy of Methyl Groups in Large Proteins. Journal of the American Chemical Society 132 (9), 2952–2960.

Owrutsky, P., Khaneja, N., Aug 2012. Control of inhomogeneous ensembles on the Bloch sphere. Physical Review A 86, 022315.

Pontryagin, L. S., 1959. Optimal control processes. Uspekhi Matematicheskikh Nauk 14, 3–20.

Pryor, B., Khaneja, N., 2006. Fourier decompositions and pulse sequence design algorithms for nuclear magnetic resonance in inhomogeneous fields. The Journal of Chemical Physics 125 (19).

Ramsey, N. F., 1955. Resonance transitions induced by perturbations at two or more different frequencies. Physical Review 100, 1191–1194.

Roehrl, M. H., Heffron, G. J., Wagner, G., 2005. Correspondence between spin-dynamic phases and pulse program phases of NMR spectrometers. Journal of Magnetic Resonance 174 (2), 325–330.

Rosenfeld, D., Zur, Y., 1996. Design of adiabatic selective pulses using optimal control theory. Magnetic Resonance in Medicine 36 (3), 401–409.

Rucker, S., Shaka, A., 1989. Broadband homonuclear cross polarization in 2D N.M.R. using DIPSI-2. Molecular Physics 68 (2), 509–517.

Runge, V. M., Wood, M. L., Kaufman, D. M., Silver, M. S., 1988. MR imaging section profile optimization: improved contrast and detection of lesions. Radiology 167 (3), 831–834.

Sacolick, L. I., Wiesinger, F., Hancu, I., Vogel, M. W., 2010. B1 mapping by Bloch-Siegert shift. Magnetic Resonance in Medicine 63 (5), 1315–1322.

Shaka, A., Keeler, J., Freeman, R., 1983. Evaluation of a new broadband decoupling sequence: WALTZ-16. Journal of Magnetic Resonance 53 (2), 313–340.

Shaka, A., Lee, C., Pines, A., 1988. Iterative schemes for bilinear operators; application to spin decoupling. Journal of Magnetic Resonance 77 (2), 274–293.

Shaka, A., Pines, A., 1987. Symmetric phase-alternating composite pulses. Journal of Magnetic Resonance 71 (3), 495–503.

Silver, M. S., Joseph, R. I., Chen, C.-N., Sank, V. J., Hoult, D. I., 1984. Selective population inversion in NMR. Nature 310, 681–683.

Skinner, T. E., Kobzar, K., Luy, B., Bendall, M. R., Bermel, W., Khaneja, N., Glaser, S. J., 2006. Optimal control design of constant amplitude phase-modulated pulses: Application to calibration-free broadband excitation. Journal of Magnetic Resonance 179 (2), 241–249.

Skinner, T. E., Reiss, T. O., Luy, B., Khaneja, N., Glaser, S. J., 2003. Application of optimal control theory to the design of broadband excitation pulses for high-resolution NMR. Journal of Magnetic Resonance 163 (1), 8–15.

Skinner, T. E., Reiss, T. O., Luy, B., Khaneja, N., Glaser, S. J., 2004. Reducing the duration of broadband excitation pulses using optimal control with limited RF amplitude. Journal of Magnetic Resonance 167 (1), 68–74.

Takeuchi, K., Frueh, D. P., Sun, Z.-Y. J., Hiller, S., Wagner, G., 2010. CACA-TOCSY with alternate 13C-12C labeling: a 13Cα direct detection experiment for mainchain resonance assignment, dihedral angle information, and amino acid type identification. Journal of Biomolecular NMR 47 (1), 55–63.

Tugarinov, V., Choy, W.-Y., Orekhov, V. Y., Kay, L. E., 2005. Solution NMR-derived global fold of a monomeric 82-kDa enzyme. Proceedings of the National Academy of Sciences 102 (3), 622–627.

Turk, E. A., Ider, Y. Z., Ergun, A. S., Atalar, E., 2014. Approximate Fourier domain expression for Bloch–Siegert shift. Magnetic Resonance in Medicine.

Ulrich, E. L., Akutsu, H., Doreleijers, J. F., Harano, Y., Ioannidis, Y. E., Lin, J., Livny, M., Mading, S., Maziuk, D., Miller, Z., Nakatani, E., Schulte, C. F., Tolmie, D. E., Kent Wenger, R., Yao, H., Markley, J. L., 2008. BioMagResBank. Nucleic Acids Research 36 (Suppl. 1), D402–D408.

Venditti, V., Fawzi, N., Clore, G., 2011. Automated sequence- and stereo-specific assignment of methyl-labeled proteins by paramagnetic relaxation and methyl–methyl nuclear Overhauser enhancement spectroscopy. Journal of Biomolecular NMR 51 (3), 319–328.

Zhang, Z., Miao, Y., Liu, X., Yang, J., Li, C., Deng, F., Fu, R., 2012. Dual-band selective double cross polarization for heteronuclear polarization transfer between dilute spins in solid-state MAS NMR. Journal of Magnetic Resonance 217 (0), 92–99.

Zuiderweg, E. R., Zeng, L., Brutscher, B., Morshauser, R. C., 1996. Band-selective hetero- and homonuclear cross-polarization using trains of shaped pulses. Journal of Biomolecular NMR 8, 147–160.